Structural and Functional Determinants of Cardiac Impulse Propagation and Arrhythmias

by

Luqia Hou

**A dissertation submitted in partial fulfillment
of the requirements for the degree of
Doctor of Philosophy
(Molecular and Integrative Physiology)
in the University of Michigan
2013**

Doctoral Committee

       **Professor José Jalife, Chair
Associate Professor Omer Berenfeld
Assistant Professor Justus Mukolu Anumonwo
Associate Professor Anatoli N. Lopatin
Associate Professor Daniel Eugene Michele**

ACKNOWLEDGEMENTS

TABLE OF CONTENTS

LIST OF FIGURES

LIST OF TABLES

LIST OF ABBREVIATIONS

AF: atrial fibrillation

AP: action potential

APD: action potential duration

CCD: charge-coupled device

CV: conduction velocity

Cx: connexin

DAD: delayed after-depolarization

DF: dominant frequency

EAD: early after-depolarization

ECG: electrocardiogram

ECM: extracellular matrix

FRAP: fluorescence recovery after photobleaching

GFP: green fluorescent protein

hERG: human ether-a-go-go-related potassium channel

iPSC: induced pluripotent stem cell

I_K: delayed rectifier potassium current

I_{Kr}: cardiac rapid delayed rectifier potassium current

I_{Ks}: cardiac slow delayed rectifier potassium current

I_{K1}: cardiac inward rectifier potassium current

I_{KACh}: cardiac ACh activated potassium current

I_{to}: cardiac transient outward potassium current

I_{Na}: cardiac sodium current

I_{CaL}: L-type cardiac calcium current

LQTS: long QT syndrome

MDP: maximum diastolic potential

MF: myofibroblasts

MI: myocardial infarction

MOI: multiplicity of infection

NRVF: neonatal rat ventricular fibroblasts

NRVM: neonatal rat ventricular myocytes

NS: non-significant

PS: phase singularities

PVC: premature ventricular complex

RMP: resting membrane potential

SCD: sudden cardiac death

SQTS: short QT syndrome

TdP: *torsades de pointes*

TEA: tetraethylammonium

VF: ventricular fibrillation

VT: ventricular tachycardia

WL: wavelength

4-AP: 4-Aminopyridine

ABSTRACT

Sudden cardiac death (SCD) attributed to ventricular fibrillation (VF) kills approximately 200,000 people each year in the United States alone. Yet, the mechanisms responsible for VF, and therefore VF-related SCD, are incompletely understood. However, what is known is that during VF, spiral waves are generated by electrical rotors at an exceedingly high frequency, and these waves then propagate through the ventricles and generate turbulent activation. Repolarizing potassium currents, including the inward rectifier potassium current (I_{K1}) and the slow component of the delayed rectifier (I_{Ks}), have been shown to contribute to the control of the rotor's spinning frequency as well as to the complexity of turbulent propagation. However, the role of the fast component of delayed rectifier (I_{Kr}) in the initiation and maintainence of VF has not previously been investigated; as a result, this ionic current served as a major area of interest during my graduate studies (see below). Another area that is gaining attention (both at a global research level and in my own work) is the potential use of cellular and gene therapy in clinical treatments. The advent of gene therapy has offered new hope and several tantalizing possibilities of new treatments for a variety of pathological conditions. With respect to cardiac physiology and arrhythmogenesis, our laboratory's goal is to use this technology to help repair

and/or restore function in the myocardium, which is inherently considered not to be a regenerative tissue/organ. Over the past years, I worked with normally non-excitable cells (cardiac fibroblasts), genetically engineered them so that they could become excitable, and determined whether they could then generate and propagate action potentials within the myocardium. In so doing, the long-term goal is to integrate these genetically modified excitable fibroblasts into injured myocardium, with the hope that they might serve as a novel means to prevent arrhythmias in ischemic heart disease and/or restore impaired cardiac function in diseased tissue.

During my PhD studies in the laboratory of Dr. José Jalife at the University of Michigan, I focused on two major questions related to cardiac electrophysiology and the mechanisms of cardiac arrhythmias. First, I examined the ionic mechanisms of reentry. Specifically, I studied how I_{Kr} influences rotor behavior. The second area of my research examined whether a combination of cellular and gene therapy, which was aimed at reducing heterogeneous propagation and cardiac turbulence, could be a novel approach to treat VF. As discussed briefly above, this project created and used genetically modified, excitable cardiac fibroblasts in order to rescue normal impulse propagation and reduce the risk of arrhythmia initiation and maintenance.

1. A major role for hERG in determining the frequency of reentry in neonatal rat ventricular myocyte monolayers: The rapid delayed rectifier potassium current, I_{Kr}, which flows through the human ether-a-go-go-related

(hERG) channel, is a major determinant of the shape and duration of the human cardiac action potential (AP). However, it is unknown whether the time dependency of I_{Kr} enables it to control the action potential duration (APD), conduction velocity (CV) and wavelength (WL) at the exceedingly high activation frequencies that are relevant to cardiac reentry and fibrillation. It was my hypothesis that upregulation of hERG would increase functional reentry frequency and contribute to its stability. Using optical mapping, I investigated the effects of I_{Kr} upregulation on reentry frequency, APD, CV and WL in neonatal rat ventricular myocyte (NRVM) monolayers overexpressing GFP (control), hERG (I_{Kr}), or a dominant negative mutant form of hERG, G628S. Reentry frequency was significantly higher in I_{Kr}-infected monolayers, and slightly reduced in G628S-infected monolayers. APD_{80} in I_{Kr}-infected monolayers was shorter (>50%) than in control monolayers during pacing at 1-5 Hz. The CV was similar in both groups at low frequency pacing. In contrast, during high frequency reentry, the CV measured at varying distances from the center of rotation was significantly faster in I_{Kr}-infected monolayers than in control. Computer simulations using a modified NRVM model predicted that rotor acceleration was due in part to a transient hyperpolarization immediately following the AP. The transient hyperpolarization was confirmed experimentally. These results show that hERG overexpression accelerates reentry frequency more than two fold in NRVM monolayers. Both APD and WL shortening, together with transient hyperpolarization, underlie the increased rotor frequency and stability. Therefore, while it has been traditionally thought that I_{Kr} reduction is pro-arrhythmic, our

results suggest that, given the right circumstances, increase in I_{Kr} could be a factor in maintaining VF.

2. Genetically engineered excitable cardiac fibroblasts coupled to cardiomyocytes rescue normal propagation and prevent arrhythmias in heterocellular monolayers: The use of genetic engineering of unexcitable cells to enable expression of gap junctions and inward rectifier potassium channels has suggested that cell therapies aimed at establishing electrical coupling of unexcitable donor cells to host cardiomyocytes may be arrhythmogenic. Whether similar considerations apply when the donor cells are electrically excitable has not been investigated. Here I tested the hypothesis that adenoviral transfer of genes coding Kir2.1 (I_{K1}), Na$_V$1.5 (I_{Na}) and connexin-43 (Cx43) proteins into neonatal rat ventricular myofibroblasts (NRVF) will convert them into fully excitable cells, rescue rapid conduction velocity (CV) and reduce the incidence of complex reentry arrhythmias in an in vitro model. At varying multiplicity of infection (MOI) ratios of 10/10, 5/10 and 5/20, NRVF co-infected with Ad-Kir2.1 + Na$_V$1.5 were hyperpolarized and generated action potentials (APs) with upstroke velocities >100V/s. However, when forming monolayers only the addition of Ad-Cx43 made the excitable NRVF capable of conducting electrical impulses (CV=20.71±0.79cm/s). When genetically engineered excitable NRVF overexpressing Kir2.1, Na$_V$1.5 and Cx43 were used to replace normal NRVF in heterocellular monolayers that included neonatal rat ventricular myocytes (NRVM), CV was significantly increased (27.59±0.76 vs. 21.18±0.65 cm/s,

p<0.05), reaching values similar to those of pure myocyte monolayers (27.27±0.72 cm/s, NS). Moreover, during reentry, propagation was faster and more organized, with a significantly lower number of wavebreaks in heterocellular monolayers formed by excitable compared to unexcitable NRVF. It suggested that viral transfer of genes coding Kir2.1, $Na_V1.5$ and Cx43 to cardiac fibroblasts endows them with the ability to generate and propagate APs. These results supported the idea that cellular therapies with excitable donor cells increase safety and reduce arrhythmogenic potential. While still preliminary, these results provide a proof-of-concept evidence that may eventually result in new therapy to treat myocardial infarction, which is associated with massive death of myocytes and replacement by fibrosis tissue.

Therefore, it is my sincere hope that the work accomplished as part of this dissertation will lead to an overall better understanding of the molecular determinants of VF, and that it will serve as a basis for the development of cell-based therapeutic approaches aimed at preventing VF and SCD.

CHAPTER 1

INTRODUCTION

1.1 Normal and Abnormal Impulse Propagation in Heart

The human heart beats approximately 36 million times every year [1]. Its function is to pump blood, and thereby provide oxygen and nutrients that are essential for the viability of cells throughout the body. For the heart to function efficiently, it is critical that atria and ventricles contract regularly and synchronously. Blood is pumped from atria to ventricles, and then to the rest of the body. During this process, arterial circulation delivers blood to vital organs, including the brain, kidneys, liver and skeletal muscles. Venous circulation returns deoxygenated blood first to the right atrium and then to the right ventricle, where it is pumped into the lungs for exchange of gases (i.e. blood becomes enriched with oxygen and loses carbon dioxide). Thereafter, the oxygenated blood returns to the left atrium via the pulmonary veins. The blood is then pumped into the left ventricle, and through the aorta to the rest of the body. This cycle continues thousands of times every day [2].

The cardiac cycle is important because the brain is highly sensitive to changes in blood pressure and blood flow. For example, interruption of the ventricular contraction for even a few seconds can lead to a drop in blood pressure. Consequently, blood supply to the brain would be reduced and a loss of consciousness would be highly probable for the individual. Taken together, decreased blood pressure and blood flow to the brain could lead to brain damage, and even death, if normal circulation is not resumed within minutes [3].

Electrical impulses are the drivers for the mechanically coordinated contractions in both atria and ventricles. The initiator of these electrical impulses is the sinoatrial node. This specialized conglomerate of intrinsically automatic cells in sinoatrial node serves as the primary pacemaker that maintains the normal rhythm responsible for each contraction of the heart. The activity of these synchronously beating pacemaker cells can be modulated by the autonomic nervous system in human, which may increase or decrease heart rate and also modulate contractions. The human heart rate is ~ 70 beats per minute at rest, but it can increase to more than 200 beats per minute during excise [4]. At the command of sinoatrial pacemaker impulses, all atrial myocytes will be the first to depolarize and contract in a coordinated way. On surface eletrocardiogram (ECG), which is recorded using electrodes that are attached to the skin and connected to a recording device, this depolarization of the atria corresponds to the P wave (Figure 1.1A). After the impulse travels rapidly through both atria to initiate their contraction, it will be delayed briefly upon reaching the atrioventricular (AV) node, which contains specialized, slowly conducting cells

that bridge the atria and ventricles. This delay, represented on ECG as the PR interval, is critical because it enables atiral contraction to complete prior to initiation of ventricular contraction which ends up closing the AV valve. Thereafter, the electrical impulse propagates through the His bundle and along the left and right bundle branches, leading to the depolarization of ventricular myocytes and their subsequent synchronized contraction. On ECG this process corresponds to the QRS complex, which is followed by the ST interval and the T wave, each corresponding to a consecutive phase during the slow repolarization of the ventricles. The cardiac cycle then repeats, with rhythmic electrical impulses generated repetitively by the sinoatrial pacemaker.

Alteration in any step of the cardiac electrical impulse (as described above) may lead to arrhythmias. Importantly, not all cardiac arrhythmias are lethal, and the symptoms may be variable under different pathological conditions as well as in different individuals [5, 6]. While most patients are not even aware of an occasional irregularity of their heartbeat, others may have very severe symptoms. This can be illustrated with the case of premature ventricular complexes (PVCs). On ECG, PVCs are characterized by wide and bizarre-looking QRS complexes that are not associated with P waves. In many patients, PVCs are asymptomatic [7]. However, for the majority of patients with symptomatic PVCs, these premature beats do not necessarily lead to a more severe arrhythmia, such as ventricular tachycardia (VT) or ventricular fibrillation (VF).

Premature beats can occur in the atria as well. Atrial premature beats originate at regions other than the sinoatrial node. On ECG they are identified by premature or deformed P waves [8]. If a premature atrial beat reaches the AV node during its refractory period, it will be unable to reach the ventricles, and as a result, there will be no QRS complex associated with it. Atrial premature beats may be harmless in healthy patients; and, like PVCs, they can be the result of normal biological variability. However, when patients have structural heart disease, atrial premature beats can trigger severe arrhythmias like atrial flutter or atrial fibrillation.

Arrhythmias can be categorized into two major types: bradyarrhythmias (heart rate less than 60 beats per minute) and tachyarrhythmias (heart rate greater than 100 beats per minute at rest) [9]. Both types of arrhythmia may occur in sinoatrial nodal disease (also known as sick sinus syndrome), which usually affects the specialized conduction system. Bradyarrhythmias may occur as a result of impairment of impulse generation or conduction. Heart block, also known as AV block, is the most common cause of bradyarrhythmia [10]. AV block occurs when there is an impairment of normal conduction between the atria and ventricles, either at the level of the AV node itself or at the level of the His-Purkinje system. There are three degrees of AV block. First degree AV block is diagnosed by a prolongation of the PR interval. Characterized by a PR interval greater than 200 ms, first degree AV block can be the non-pathological result of enhanced vagal tone, which is often a consequence of intense physical training. On the other hand, it could also result from an acute myocardial infarction or from

pharmacological agents [11]. However, unlike the other two types of AV blocks, while the PR interval is prolonged, its duration at rest is relatively constant, and for each P wave, there is a subsequent QRS complex.

Second degree AV block is defined as one or more atrial impulses that fail to propagate to the ventricles [12]. On ECG this can be visualized as a P wave that is not followed by a QRS complex. Second degree AV block can be further classified as type 1 and type 2. Type 1, also known as Wenkebach periodicity, can be a benign response to an increase in the normal atrial frequency that manifests itself as increasing delays between the P wave and the QRS complex before the omission of one QRS complex [13]. In typical Wenckebach periodicity, the prolongation of the PR interval occurs with decreasing increments; whereas atypical Wenkebach periodicity is associated with progressive PR prolongation with increasing increments. Type 2 second degree AV block has no such pattern. Instead, AV block occurs suddenly without prior changes in the PR interval. Like first degree AV block, second degree AV block may result from pharmacological agents or diseases. However, in this case the alteration is usually due to abnormal conduction at the level of the His-Purkinje system [14].

Third degree AV block is also called complete heart block, which means that none of the atrial impulses conduct to the ventricles [15]. On ECG, two independent rhythms may be detected in association with third degree AV block. One rhythm is the result of atrial depolarization under the command of the SA node. As a result, patients with third degree AV block have regular PP intervals.

The other rhythm is the excitation of the ventricles initiated by the AV node. This generates QRS waves with variable PR intervals. Unlike the other two types of AV block, third degree AV block is always the result of an underlying pathology, with the most common cause being myocardial infarction [16].

Tachyarrhythmias may originate in the atria or the ventricles. During atrial flutter, a patient's atrial contraction rate can increase up to 240 - 433 beats per minute [17, 18]. On ECG atrial flutter manifests as flutter waves, which can vary in both the beat-to-beat amplitude and duration. As with monomorphic or polymorphic VT, atrial flutter can lead to atrial fibrillation.

Atrial fibrillation (AF) is a severe type of atrial arrhythmia [19, 20]. Like atrial flutter, AF excites the atria at high rates: 240-360 beats per minute. On ECG, AF is typically characterized by the absence of P waves, which are replaced by disorganized electrical activity with irregular RR intervals [21].

VT and VF are the most severe forms of ventricular arrhythmias. Monomorphic VT may result from ventricular ectopic discharges or from reentry in the ventricles. It is characterized by an excessively rapid heart rate in the absence of P waves. Further, the interbeat intervals are periodic and the QRS complexes are identical to each other in any given ECG lead [22].

On the other hand, polymorphic VT is distinguished by beat to beat variations in the amplitude and/or morphology of the QRS complex [23]. *Torsades de pointes* (TdP), which literally means twisting of the points, is the most well-known example of polymorphic VF. It is characterized by a waxing and

6

waning of the QRS amplitude, and it may terminate spontaneously or degenerate into VF [24].

Similar to AF, both monomorphic and polymorphic VT could be the emsemble outcomes of underlying genetic factors, nutritional deficiencies, pharmacology, and/or gross structural changes to the heart anatomy that are most commonly brought on by myocardial infarction [20, 25, 26]. VT is life-threatening, mostly because it has the potential to degenerate into VF, which is defined as turbulent cardiac electrical activity that precludes adequate pumping of blood. On ECG, VF is characterized by an excessively rapid (>500 QRS complexes/min) and irregular heart rhythm that results in uncoordinated contraction [27]. VF rapidly results in loss of consciousness because of cessation of blood circulation, and it may lead to an irreversible tissue/organ damage unless terminated within 10 minutes by electric shock treatment [28].

While there are numerous types of arrhythmias, some being asymptomatic and others being highly symptomatic, a better understanding of the causes, treatments, and prevention for each can be best achieved through knowledge of the molecular and biophysical bases of ion channel function, which underlie the characteristics of the cardiac action potential.

1.1.1 Action Potential and Ion Channels

To understand cardiac impulse propagation and the mechanisms of arrhythmias, one must first examine the excitability of a single cell. Excitability is a key property that underlies the ability of the electrical impulse to propagate from cell to cell throughout the heart [29, 30]. Similar to neurons and skeletal

muscle cells, cardiac myocytes are excitable cells. Unlike other cell types,

excitable cells have a well-polarized resting membrane potential (RMP). The

RMP is the result of electrochemical gradients, and it is established by the

diffusion of multiple ions (e.g., Na^+, K^+, Cl^-) across specialized membrane protein

channels that are embedded in the cell membrane. At rest, the membrane

potential of non-pacemaker cells remains stable at -70 to -90 mV. However, the

ionic fluxes of sodium, calcium and potassium ions across the membrane enable

excitable cells to generate action potentials (APs). These ionic fluxes directly

results in a stereotypic change in the electrical potential across the cell

membrane, which is associated with the passage of an impulse. Importantly, the

duration of the cardiac AP is much longer (~ 200 ms) than the AP characteristic

of neurons and skeletal muscle cells (~1 and 10 ms, respectively) [31]. The

temporal course of the cardiac AP is divided into five distinct phases numbered

0-4 (Figure 1.1B). Phase 0 is initiated by depolarization to a threshold potential (~

-60 mV) for activation of the fast sodium inward current (I_{Na}) through voltage-

gated, cardiac-type sodium channels. Typically, the influx of positively charged

sodium ions depolarizes the atrial or ventricular myocyte at a very high speed to

an overshoot of the membrane potential to +30 mV. Phase 1 represents the

quick partial repolarization that occurs immediately after peak depolarization.

Phase 1 often appears as a notch, and this is due to the fast inactivation

(closure) of sodium channels and the activation (opening) of the transient

outward potassium channels (I_{to}). Phase 2 is called the plateau phase of the

cardiac AP. At this phase, the membrane potential lingers transiently near 0 mV

and contributes to the long APD. The plateau represents the balance between inward currents, through L-type calcium channels (I_{CaL}), and outward currents, mainly through I_{Kr} and I_{Ks} which are the rapid and slow components, respectively, of the delayed rectifier current [32]. With time, the slow decrease in I_{Ca} together with an increase in outward potassium currents tilts the balance towards further repolarization. During phase 3, a large outward current (I_{K1}), provided by strong inward rectifier potassium channels (Kir2.x), brings the membrane potential back to its resting level. Phase 4 is the RMP. During this phase, the dynamic balance between the inward and outward movement of potassium ions through inward rectifier potassium channel keeps the RMP at a very negative level. Thus, I_{K1} is critical to cellular excitability: by maintaining RMP at -70 to -90 mV during rest, and by ensuring the availability of sodium channels for the initiation of the next AP [33]. In addition, a number of other ion channels also contribute to RMP in cardiac cells, such as sodium/potassium pump, sodium/calcium exchanger, and chloride channels.

1.1.2 Ventricular Fibrillation and Sudden Cardiac Death

Ventricular fibrillation (VF) is the leading cause of sudden cardiac death (SCD), which accounts for about 200,000 fatalities annually in the United States alone [34]. Despite decades of research, there is no cure for VF, and the best long-term treatment remains the implantation of an Implantable Cardiac Defibrillator (ICD). Most likely, this is due to an incomplete understanding of the molecular mechanisms responsible for VF [34-36]. On ECG, VF is diagnosed by the presence of an aperiodic and irregular rhythm, which suggests that cardiac

9

activation of the ventricles is exceptionally complex and disorganized during the VF period (Figure 1.1C) [36]. However, modern technologies that enable high spatial and temporal resolution imaging as well as the complex mathematical modeling (computer simulations) have provided evidences to support the idea that VF is, in fact, deterministic, quantifiable, and mechanistically understandable [35, 37]. Reentry is one type of abnormal impulse propagations observed during fibrillation. It occurs when an electrical impulse travels in continuous loop, rather than propagating linearly throughout the heart. A number of experimental and computer simulation studies have suggested that reentry is one of the most important mechanisms underlying VF and SCD [38-40].

1.1.3 Reentry and Arrhythmias

The first descriptions of reentry activity during VF were provided by MacWilliam in 1887 [41]. Three important features of "arrhythmic fibrillar contraction" were observed in that principal study: complexity, persistence, and rapidity. However, the first mechanistic insight into how VF can occur came twenty years later when Mayer et al. observed and described reentry activity in jellyfish tissues [42]. The important observation from this study was that unidirectional block was a prerequisite for reentry activity to occur. In 1914, Mines et al. further improved our understanding of arrhythmias by providing evidence that reentry around an obstacle was responsible for arrhythmias in dog cardiac tissue [43]. Subsequent works focused on what we now call "anatomical" reentry, which relies on a fixed barrier around which the electrical wave can travel [44-46]. However, as improvements in technology allowed for more precise

measurements of impulse propagation, it was discovered that the presence of an anatomical obstacle was not always a prerequisite for fibrillation. In the 1970s, Allessie et al were the first group to demonstrate functional reentry in rabbit atrial muscle [47]. In their study, Allessie et al. proposed the "leading-circle" concept, which was defined as a sustained wave of propagation at the "leading" tip of a circuit around a critical sized "circle" [47-49]. This concept was highly appreciated by both clinicians and experimental physiologists because it not only complemented our early understanding of fibrillation, but it also was a theory that allowed for verifiable antiarrhythmic interventions. However, subsequent technological breakthroughs would later allow for even more precise measurements and new insights. Advances in biophysics and computer modeling, for example, led to the concept of "rotors" as the drivers of "spiral wave" reentry [50].The introduction of this principle has significantly expanded and improved our understanding of functional reentry as a central mechanism of cardiac fibrillation.

The idea that rotors and spiral waves could exist in the heart initially came from studies in other excitable media, such as a chemical reaction called the Belousov–Zhabotinsky reaction [51]. It was found that if the conditions were just right, the solution (e.g. Ferroin solution) would change color in a spiral wave fashion [52]. Arthur T. Winfree was one of the first theoretical biologists to use mathematical modeling to demonstrate that rotors could theoretically exist in the heart [53]. Further, using 3-D computer models of the heart, it was shown that a rotor of electrical impulse is a "fingerprint" of a 3-D wave called a scroll wave [36,

54-56]. Experimental evidence for the existence of rotors and spiral waves of electrical impulse in many mammalian species (mouse, guinea pig, rabbit, pig, sheep and human) was obtained using high temporal/spatial optical imaging on the surface of isolated heart by Jalife's group and others [57-62]. Using voltage sensitive dyes (e.g. di-4-ANEPPS, di-8-ANEPPS) and charge-coupled device (CCD) cameras, optical mapping has been demonstrated to be a very powerful tool to visualize and study complex patterns of electrical wave propagation during cardiac arrhythmias [63].

One obstacle to current research on spiral waves and rotors is the limitation posed by technology. For example, investigators cannot image 3-D propagation of electrical wave in the ventricles with the high spatial/temporal resolution needed to visualize spiral waves; and, as a result, they are limited to 2-D analysis of the heart [64, 65]. This poses a significant problem that may affect the interpretation of the results: Depending on the orientation of the scroll wave and the placement of the imaging device, one may observe a spiral wave, or see other complex impulse propagation patterns [66]. An indirect, but nevertheless, useful tool called dominant frequency (DF) mapping was therefore developed to infer the location of a scroll wave [67]. Using Fast Fourier Transform analysis, DF mapping enables to take a fluorescent signal obtained during optical mapping and convert it from the time domain to the frequency domain. In the frequency domain, the frequency with the highest amplitude (power) is called the DF; which likely represents the rotation frequency of the scroll wave. Therefore, if spiral waves are the "fingerprints" of 3-D scroll waves that underlie fibrillations, then

understanding the dynamics of spiral waves should enable us to better understand both atrial and ventricular fibrillation.

1.1.4 Properties of Spiral Waves

Propagation of voltage waves through the myocardium is a complex non-linear phenomenon. Historically, our understanding of this process began with the application of the classical cable theory to cardiac electrophysiology [68, 69].

Voltage impulse propagation can be clearly illustrated with an example of a very simple model: a 1-D cable of myocytes where a stimulus is applied to one end of the cable. It is useful to think of a propagating wave in the cable as a propagating AP. Phase 1 can be considered to be the wave front and phase 3 can be considered to be the wave tail. If this AP were to propagate through the 1-D cable, a source cell (depolarized cell) would need to provide enough electrotonic current through gap junctions to its neighboring cell in order to bring that cell's membrane potential to the threshold for sodium channel activation. Once the neighboring cell generates an AP, it then becomes a source and the process continues as the wave propagates from cell to cell. The process of ion fluxes that occur below the membrane potential for sodium channel activation are called electrotonic interactions.

If the 1-D cable was replaced by a 2-D sheet, then the scenario would become much more complex. Consider the example of a planar wave propagating through a homogenous medium composed of thousands of electrically connected heart cells (Figure 1.2A). As the wave propagates, the conduction velocity (CV) can be calculated by measuring the activation time

between fixed points and then dividing it by the distance traveled between points. If, however, the wave is concave (negative curvature), then the cells at the wave front need to provide current to relatively fewer cells than would be required by a planar wave (Figure 1.2B). For a concave wave, more diffusive current is available to flow into the recipient cells as compared to the planar wave situation. As a result, the recipient cells (of a concave wave) are depolarized quicker, which thereby increases the CV. However, if we consider a convex wave (positive curvature), the situation is reversed (Figure 1.2C). Compared to the concave or the planar wave, the cells at the curved wave front must activate a relatively large number of cells ahead of them, and this results in a lower CV with respect to concave or planar waves. Importantly, if the convexity (positive curvature) of the wave front exceeds a critical value, then the cells at the wave front will not be able to provide enough depolarizing current to excite downstream cells, and conduction block occurs as a result. In the case of a spiral wave, the curvature of the wave front increases and the CV decreases toward the center of rotation. Near the very center (i.e., at the tip of the spiral), the curvature is critical and the velocity is zero, which forces the wavefront to pivot around an unexcited, but eminently excitable, core (Figure 1.2D). Thus, a spiral wave rotates around an area of unexcited cells that are available to be excited once they receive enough current to bring them above the threshold for sodium channel activation. As such, a spiral wave can either be stationary or rotate continuously around the core. It can also invade the core, or meander in complex geometrical patterns. Why this occurs is not entirely understood, but it is thought to be a consequence

of the flow of electrotonic currents between cells at the core and cells at or near the rotor tip. Rotor meandering or drift may also occur as a result of wave front-wave tail interactions (see below).

The wave front is always followed by its wave tail, and the spatial extension between them is known as the wavelength (WL). The wave front corresponds to the AP upstroke and the wave tail corresponds to repolarization; therefore, in a planar wave, the WL can be approximated as CV x APD. However, this formula usually does not apply to a spiral wave since both APD and WL change with distance from the core. At the core, cells function as current sinks, shortening APD of the cells in its immediate vicinity, which are acting as the current source. Therefore, the APD and WL are smaller closer to the core and larger when farther away from the core (Figure 1.2D).

It has been shown that the frequency at which a spiral wave can rotate around a given core, the size of the core, and the degree of meandering of the wave depend primarily, but not entirely, on two factors: excitability and APD. If the system is highly excitable, a spiral wave can have a higher critical curvature. This is because of more depolarizing current in any given source cell available to excite downstream cells. The opposite is true for reduced excitability. In such situation, the curvacure of a spiral wave is lower and the propagation of wave front also becomes slower.

If the WL is large near the core, then there is a high probability that the wave front will collide with its tail. These wave front-wave tail interactions can lead to meandering of the wave, and they may eventually terminate in fibrillation

or lead to local wavebreaks. A shorter APD, on the other hand, will result in a smaller wavelength, which minimizes the chance of meandering or wavebreak to occur. Wavebreak happens when the wave front encounters refractory tissues, or when the wave front (i.e., the source) is too weak to depolarize downstream cells above threshold. The general consensus is that wavebreak is critical in rotor formation and the breakdown into turbulent activity, also termed "fibrillatory conduction".

1.1.5 Animal and Human Studies of Fibrillation

Based on computer simulations first using simplified excitation-diffusion models and later models that included specific ionic channel kinetics and millions of electrically coupled cells, investigators predicted that any shortening of the APD or increase in the excitability should stabilize spiral waves [70, 71]. Further, it was predicted that gradients in APD/excitability should provide a substrate for wavebreaks. Since wavebreaks serve as a "footprint" for the formation of scroll waves, it was thus postulated that should wavebreaks occur in the heart, fibrillation dynamics should consequently change, based on the above predictions.

In experiments with isolated Langendorff-perfused guinea pig hearts, Warren et al. visualized a long-lasting stable rotor in the LV as well as the breakup of 1:1 propagation in the right ventricle [72], which resulted in a left-to-right gradient in VF frequency. Combining this observation with subsequent advances in molecular biology, the molecular mechanisms responsible for fibrillation gained a solid foundation as it was beginning to be explored. It was

then soon discovered that a spatial gradient of I_{K1} density existed between the left and right ventricles in guinea pig heart presumably a result of the left ventricle having a higher expression level of Kir2.1, which is the primary protein component of I_{K1} in the ventricles [58]. Further, perfusion with $BaCl_2$ at low concentrations that preferentially block I_{K1}, slowed and then terminated VF in all cases studied. The finding that a gradient of the inward rectifier current is responsible for frequency gradients is not limited to just the ventricle, as similar results, and gradients, have been found in the atria as well [73]. For example, the left atrium has a higher density of I_{KACh} (an inward-rectifing potassium current activated by releasing of acetylcholine (ACh)), and it also has a higher dominant frequency than the right atrium during AF [74].

In 2004, Li et al. generated a transgenic mouse model in which Kir2.1 was overexpressed specifically in the heart [75]. This Kir2.1 overexpressing mouse had a slightly more negative resting membrane potential and a drastically shorter APD than the littermate wild type (WT) mice. In optical mapping experiments, Noujaim et al. demonstrated that VF in the Kir2.1 overexpressing mouse heart was much more stable and faster (~ 43.5 Hz; 5.8 minutes) than that observed with WT hearts (~26.3Hz; 3 seconds), as predicted by simulations [76]. Such data suggested a major role for I_{K1} in the control of the frequency and stability of rotor activity during VF in the mammalian heart.

In 2008, Muñoz et al. investigated the role of the slow component of delayed rectifier, I_{Ks}, in fibrillation dynamics [77]. Using a neonatal rat ventricular myocyte (NRVM) monolayer model, they demonstrated that, in contrast to I_{K1} up-

regulation, I_{Ks} overexpression resulted in post-repolarization refractoriness. As a result of the effective refractory period outlasting the APD, Muñoz et al found that there was an increase in the formation of wavebreaks and fibrillatory conduction without significant change in rotor frequency, likely due to I_{Ks}'s accumulation effect at high frequency.

Experiments using animals (sheep [78] and rabbit [79]) have demonstrated that sodium channel blockade reduces excitability, which therefore leads to slow propagation and reduces the stability and frequency of rotors. As a result, meandering, and ultimately, termination of VF occurs by collision of the rotor with a boundary. However, it is known that sodium channel blockade can be proarrhythmic, as demonstrated in the Cardiac Arrhythmia Suppression Trial (CAST) [80]. Further, one of the most common conditions that predispose an individual to VF is heart failure, which itself results in a prolongation of the APD [81]. Taking experimental and clinical data together, there seem to be some discrepancies between the theory of rotors and what actually happens in the human heart. Are such discrepancies the result of flaws in the theory or do they rather represent inherent limitations of our experimental approach to study VF in a mammalian system? In order to address these important questions, it is necessary to better understand the molecular mechanisms of reentry arrhythmias at the cellular as well as at the whole organ levels.

1.1.6 Monolayers as a Model to Study Spiral Waves

Cultured NRVM monolayers are electrically coupled and can contract synchronously. Recently, monolayers have been generated from human stem

cell derived myocytes in order to study human electrophysiology [82]. While artificial compared to the 3D heart, both human and neonatal rat cardiomyocyte monolayers provide an ideal model in which to study spiral wave dynamics under a variety of different conditions (e.g. overexpression/silencing of various proteins, heterocellular coupling of non-myocytes to cardiomyocytes). Either rat or human monolayer can be used as an ideal model for the study of spiral waves. They can be easily visualized, and the cells that constitute the monolayer are biological in origin. Further, they contain biological and electrophysiological parameters that cannot be taken into account with the current computer modeling due to the inherent limitations in processing power, etc. [83]. Despite being a reductionist technique, our laboratory has successfully used the NRVM, and now human iPS-derived cardiomyocyte monolayer model to study how different ion channels and, more importantly, how other cell types influence spiral wave activity.

One area in which our laboratory as well as other groups have used the monolayer system is to examine how different repolarizing potassium currents affect spiral wave biophysics. Specifically, we demonstrated that spiral wave stability and break up can be modulated by the amount of I_{Ks} [77]. Leslie Tung's laboratory has shown that heterogeneity of I_{K1} in NRVM can influence spiral wave dynamics as well [84]. However, the effects of another important repolarizing current, I_{Kr}, in controlling rotor dynamics remained unstudied until this dissertation (Chapter 2).

Recently, more complex monolayer models have been generated and characterized. Different cell types have been introduced into a given monolayer

of cardiomyocytes, including cardiac fibroblasts [85], genetically modified HEK cells [86], and human stem cells [87]. These new models have helped to further expand our understanding of how the interaction between cardiomyocytes and different cell types impacts electrical impulse propagation. For example, our lab has developed a heterocellular monolayer model composed of randomly distributed NRVM and neonatal rat ventricular fibroblasts (NRVF) in order to mimic the pathological situation of fibroblast infiltration [85]. The data obtained from studies using this model have provided solid evidences to support that strong correlations exist between the proportion of fibroblasts and CV, rotor frequency, and fibrillatory conduction. A higher ratio of fibroblasts to myocytes resulted in a biphasic change in CV, a reduction in rotor frequency and increase in fibrillatory conduction. Therefore, I took advantage of this heterocellular model, and investigated whether genetically modified cardiac fibroblasts could have the opposite effect when coupled with native cardiomyocytes (Chapter 3).

1.2 Functional Determinant of Rotor Dynamics

While rotors have been recognized as the main mechanism underlying VF for years, the ionic mechanisms responsible for their behavior are still incompletely understood. Previous studies suggested that the frequency and the stability of rotors are determined in great measure by the RMP and CV. These, in turn, are largely controlled by the dynamic interplay between the outward component of the inward rectifier potassium current (I_{K1}) and the rapid inward sodium current (I_{Na}). Milstein et al. demonstrated that there is a dynamic

reciprocity of Kir2.1 (I_{K1}) and Na_V1.5 (I_{Na}) channel expression that exits across

different species [88]. These results further suggested that the relationship

between I_{K1} and I_{Na} plays a central role in controlling membrane properties in the

heart.

Our laboratory has shown that upregulation of the slow delayed rectifier

potassium channels (I_{Ks}) does not affect reentry frequency, but does significantly

increase the incidence of fibrillatory conduction [77]. However, when I started my

doctoral work, it was not known how the rapid delayed rectifier current (I_{Kr})

influences spiral wave dynamics. In Chapter 2, I will present the

electrophysiological consequences of increasing I_{Kr} in rotor frequency and spiral

wave dynamics. While the effects of I_{Kr} on spiral waves were not known prior to

my doctoral studies, there was a large body of knowledge about the I_{Kr} current

itself as well as data to suggest an association between variations in the

biophysical properties of I_{Kr} and arrhythmias.

1.2.1 hERG and LQT/SQT

The human ether-a-go-go-related (hERG) gene (*KCNH2*), located on

chromosome 7q35-q36, encodes α subunits of the channels that responsible for

the rapid component of the delayed rectifier current I_K [89]. hERG was originally

cloned by Warmke and Ganetzky in 1994 from a human hippocampal cDNA

library [90]. While it is clearly found in neuronal tissues, the hERG protein is most

abundantly expressed in the heart [91].

The rapid component of the delayed rectifier current, I_{Kr}, is important in

determining the shape and duration of the human cardiac AP. Reduction of I_{Kr}

results in AP prolongation, cardiac arrhythmias, and sudden cardiac death [92]. In 1995, the Keating laboratory reported that mutations in *hERG* were associated with chromosome 7-linked inherited long QT syndrome (LQT2) [93].

LQTS is defined by a QT interval prolongation on the ECG (Figure 1.1A). This delay in ventricular repolarization greatly increases the patient's risk of developing TdP [94], which can further evolve into lethal VF. The most common causes of LQTS are mutations in one of three ion channel encoding genes, with the channel's respective current given in parentheses: *hERG* (I_{Kr}), *KCNQ1* (I_{Ks}) and *SCN5A* (I_{Na}) [89]. Drug-induced LQTS has also been observed in patients as a result of I_{Kr} blockade. For example, one side effect of the antiarrhythmic drug quinidine is TdP, which has been reported in ~2-9% of patients who take quinidine [95]. The arrhythmogenic potential of I_{Kr} blockade has resulted in numerous drugs being withdrawn from the market, including medications treating gastrointestinal disorders and allergies (e.g. cisapride and terfenadine) [96]. Moreover, it has also encouraged pharmaceutical companies to more carefully screen their compounds for potential hERG channel blockade during the preclinical safety assessment [97].

However, the arrhythmogenic potential associated with hERG/I_{Kr} is not limited only to a loss-of-function in I_{Kr}. A gain-of-function mutation of hERG, N588K, was identified in association with short QT syndrome (SQTS) [98]. This provided evidence that upregulation of I_{Kr} can also be arrhythmogenic. However, early studies observed an antiarrhythmic effect when hERG channels were expressed in adult rabbit ventricular myocytes maintained in primary culture [99].

In this study by Nuss et al., cultured myocytes normally exhibited prolonged the APD and they were predisposed to early afterdepolarizations (EAD). An increase in hERG expression enhanced AP repolarization and reduced the incidence of EAD [99]. Therefore, upregulation of I_{Kr} was shown to exert both pro-arrhythmogenic (SQTS) and anti-arrhythmogenic activities (*in vitro* rabbit myocyte culture). However, how alteration in I_{Kr} influences spiral wave dynamics was not clear from these studies.

1.2.2 hERG Structure and Kinetics

hERG encodes the α subunit of a classic voltage-gated potassium channel. The structure of the 1159 residue protein consists of six transmembrane domains (S1-S6), including a voltage sensor S4 and a potassium selective pore region between the S5 and S6 segments (Figure 1.3) [92]. A functional hERG channel is composed of four subunits (tetramer). Like other voltage-gated potassium channels, hERG channels differ from sodium and calcium channels in that their four homologous domains are not covalently linked, but are presumably assembled by non-covalent associations. In addition to the transmembrane domains, the hERG α subunit also contains two cytoplasmic domains: the amino N- and carboxyl C-terminal domains. The hERG N-terminus contains a PAS (Per-Arnt-Sim) domain, which is believed to play a role in the deactivation process of the channel [100]. The C-terminus contains a cyclic-nucleotide-binding domain (cNBD), which has been shown to affect channel trafficking and processing in the endoplasmic reticulum [101]. hERG α subunit

also interacts with KCNE2, accessory subunits which modulate the channel's biophysical properties [102].

In 1995, Sanguinetti et al. and Trudeau et al. reported the gating properties of hERG channels in *Xenopus* oocytes [93, 103]. hERG channels have three states: closed, open, and inactivated. The gating kinetics of hERG channels is very unusual. The channel exhibits rectification similar to that of the inward rectifier potassium channel. The mechanism of this inward rectification process was shown to be the result of a fast and voltage dependent inactivation that reduces whole cell channel conductance at positive voltages, by Smith et al. in 1996 [104].

Voltage-gated potassium channels have different mechanisms of inactivation [105]. The first one is N-type inactivation, which is commonly referred to as ball-and-chain inactivation since it is believed that amino acids swing into the pore in order to prevent ion fluxes. Another type is C-type inactivation, which is believed to involve changes in the 3D conformation of the channel as a means of preventing ion fluxes. Regardless of the mechanism of inactivation, the ion channel again becomes capable of allowing ion flow when the transmembrane voltage returns to more hyperpolarized potentials.

In 1996, three groups using different approaches independently ruled out the possibility of N-type inactivation with respect to hERG channels [104, 106, 107]. Each of them provided evidences that the inactivation is neither sensitive to internal TEA (tetraethylammonium) application nor to the deletion of the N-terminus. Thereafter, investigators recognized the inactivation of hERG channels

as being analogous to the "C-type" mechanism of inactivation [108, 109]. In accordance, and similar to that observed for *Shaker* (the first cloned potassium channel [110]), hERG inactivation is sensitive to the ion occupancy of a selectivity filter as well as to external TEA application [104, 106]. Moreover, when Ser631 is mutated in hERG, the inactivation process is compromised. Ser631 is functionally equivalent to Thr449 in *Shaker* in that each residue is critical to the C-type inactivation of its respective channel [111, 112]. However, inactivation of hERG channels is fast and voltage-dependent, while it is the opposite (slow and voltage insensitive) for *Shaker* channels [109]. Compared to the rapid inactivation of hERG, the activation process of hERG channels is unusually slow.

Wang et al. was the first to study the voltage dependence of hERG activation in detail [113]. They proposed a three closed state activation model with a voltage-insensitive intermediate closed state, which accurately reproduced the time and voltage dependence of the activation and deactivation of hERG. In addition, they pointed out that the activation process was insensitive to extracellular potassium, but inactivation was sensitive to changes in potassium concentration. When $[K]_o$ was changed from 2 to 98 mM, Wang et al. reported that hERG inactivation did indeed undergo a shift of ~30 mV towards depolarization.

Recent studies have discovered an alternatively processed hERG isoform, hERG1b, which has identical transmembrane and cytoplasmic domains as hERG1a but contains a truncated N-terminus [114, 115]. hERG1b is 340 amino acids shorter than hERG1a, and is able to form heterotetrameric channels with

hERG1a. Compared to hERG1a alone (homotetrameric channel), the heterotetrameric channel has a faster activation, deactivation, and recovery from inactivation [116]. This partially explains the differences in gating kinetics between native I_{Kr} in myocytes and the current through hERG channels composed of hERG1a alone in autologous cells [117, 118].

1.2.3 hERG Contribution to Repolarization

The contribution of I_{Kr} to repolarization has been recognized for decades. hERG channels are active during phases 2 and 3 of the cardiac action potential. The balance between hERG current and L-type calcium current contributes to the plateau phase of the action potential. The prolonged plateau phase ensures that adequate extracellular Ca^{2+} enters the cell to enable excitation-contraction coupling. It also allows the cardiac tissue a period to remain refractory, and hence, it serves to partially protect the heart from the propagation of premature beats/arrhythmia [92]. hERG channels start to open when the membrane potential is depolarized above -60 mV. While depolarization continues, hERG channels rapidly enter into an inactivation state, which reduces the membrane conductance and the outward current. It results in low hERG current flow during depolarization and the plateau phase. However, during repolarization, hERG channels recover from inactivation at a faster rate than deactivation, and this initiates phase 3 repolarization of the AP. This progressive increase in hERG current causes the repolarization of the cardiomyocyte to continue, and it eventually reaches the maximal current before the final rapid declining phase of AP.

1.3 Structural Determinants of Impulse Propagation

While ion channels are paramount to cardiac impulse propagation and myocytes contraction, the heart also contains numerous cell types and structures that are not actively involved in contraction. Nevertheless, they are crucial to normal heart physiology and as new evidence suggests, also to arrhythmias.

1.3.1 Fibrosis and Arrhythmia

Cardiac pathologies generally lead to structural remodeling and the development of fibrosis [119]. These processes are often accompanied by cardiomyocyte hypertrophy, fibroblast activation and proliferation, and an imbalanced extracellular matrix (ECM) deposit [120]. Once fibroblasts differentiate into myofibroblasts (MF), they are able to modify the electrophysiology of cardiomyocytes by heterocellular coupling via gap junctions [121]. On one hand, this action may rescue electrical impulse conduction between disconnected myocardium by acting as short-range conductors; on the other hand, the delayed conduction associated with unexcitable myofibroblasts may promote unidirectional conduction block and reentry arrhythmias.

Although cardiomyocytes occupy 70% of the volume of the working myocardium, cardiac fibroblasts are the most abundant cell type in the heart [122, 123]. These fibroblasts are important for maintaining myocardial structure by forming a three-dimensional extracellular network/matrix surrounding myocytes in healthy myocardium. The main components of the matrix are collagen and elastin [124]. Under physiological conditions, the production and

27

degradation of collagen is very tightly regulated [125]. However, when an injury such as myocardial infarction (MI) takes place in the heart, fibroblasts differentiate into their active form of MF. In this state, MF proliferate and increase the ECM deposit. They also promote myocardial remodeling and the formation of a scar [126]. During this remodeling, it is common for cardiomyocytes to undergo hypertrophy and experience cell death [127]. As a result, where there once was excitable tissue (composed of healthy cardiomyocytes) is now replaced with unexcitable tissue infiltrated by fibroblasts/MF (fibrosis).

Fibrosis leads to the accumulation of collagen, which may serve as an electrical insulating barrier for spiral wave anchoring and may thus act to stabilize arrhythmias [128, 129]. Also, a redistribution of connexins is often observed in infarcted tissue, and this could also favor the initiation and perpetuation of arrhythmias [129]. In addition, during reentrant arrhythmias, the rapidly succeeding electrical wave emanating through fibrotic myocardium generates fragmentation and wavelets that may lead to fibrillatory conduction. Together, these effects may further reduce the likelihood of arrhythmia termination.

However, it is important to note that the arrhythmogenic potential of fibrosis is multi-faceted. Its effects are not merely due to the loss of healthy myocardium nor only to changes in myocardial connectivity in response to increased accumulation of ECM components. The effects of fibrosis are often cumulative and include both the above factors, and are often further influenced by potential electrical coupling between unexcitable MF and surviving cardiomyocytes.

1.3.2 Myofibroblast and Impulse Propagation

MF are unexcitable cells with a more depolarized resting membrane potential (-15 to -40 mV) and a higher membrane resistance (4 GΩ) than cardiomyocytes [130-132]. Therefore, when MF electronically couple to myocytes, they can potentially serve both as current sinks for electrical charges as well as short and long range conductors [128, 133, 134]. MF have been shown to affect electrical impulse propagation by causing slow and "zigzag" conductions [135]. Further, by functional coupling with myocytes, MF can contribute to conduction block, which itself increases the probability of initiating reentry arrhythmias [135, 136].

An important feature of MF is the expression of connexins, which has been shown in a variety of tissues [137, 138]. Both homocellular gap junctional coupling with other MF and heterocellular gap junctional coupling with myocytes have been identified *in vitro*. In 1992, conductance of gap junctions in MF was measured and reported by Rook et al.: 21 pS between MF and 32 pS between MF and myocytes [130]. Using immunohistochemistry and Western blot analyses, subsequent studies have demonstrated expression of multiple connexin proteins (connexin43, connexin40 and connexin45) in MF across different species [133, 139, 140]. It has been suggested that these connexins are able to form heterologous gap junctions, which may provide an explanation for the unusual conductance reported earlier (Cx43: ~100 pS; Cx40: ~150 pS; Cx45: ~50 pS).

Because of the difficulty in studying MF in complex and variable remodeled myocardium *in vivo*, a number of *in-silico* and *in vitro* models have

29

been generated to assess the functional consequences of MF-myocyte interactions [85, 133, 141, 142]. Using a mathematical model, MacCannelll et al. showed that several changes occur in the properties of myocytes when they are coupled to MF, including APD shortening and reduction in AP plateau height [142]. However, RMP of coupled myocytes was unchanged. Miragoli et al. later provided experimental evidences showing that MF were able to depolarize myocytes in a co-culture with neonatal rat myocyte strands. In this unique co-culture model, strands of cardiomyocytes were coated with a layer of MF at different plating densities [133]. As the density of MF increased, the resting membrane potential of the myocyte strands gradually depolarized from about -80 mV to -55 mV. This resulted in biphasic changes in both conduction velocity and upstroke velocity of AP. The results from Miragoli et al. provided "proof of concept" evidence that MF can serve as a current sink when coupled to cardiomyocytes.

Gaudesius et al. identified a different role that MF may play in impulse propagation: short and long-range conductors [134]. In their *in vitro* model, MF at various lengths were inserted in the middle of two myocyte strands. Conduction delays were observed at shorter lengths before conduction block eventually occurred when MF inserts exceeded 300 µm. More recently, our laboratory further studied the effect of MF in initiating and maintaining reentrant arrhythmias [85]. To examine how MF influence spiral wave dynamics, we used a heterocellular model in which NRVM and MF were co-cultured at different ratios. Compared to control dishes (containing NRVM alone), more complex wave

propagation with a slower frequency was observed in dishes with high MF to NRVM cell ratios. Moreover, in both experiments and computer simulations, conduction velocity and heterocellular coupling displayed a biphasic relationship similar to that which has previously been shown by Miragoli et al. [133]. Specifically, there was an initial decrease that was followed by an increase in conduction velocity. This biphasic relationship can be explained by a switch in the role that MF plays in impulse propagation: from current sink to conductor. As coupling initially increases, the MF become a stronger current sink and act to slow impulse propagation. This occurs until MF reaches a threshold and they are then able to pass enough current to initiate an AP from downstream myocytes. Thereafter, further increase in coupling would make MF stronger conductors, and this would, as a result, increase conduction velocity.

MF can also influence the remodeling of cardiomyocytes through the release of multiple cytokines (e.g. TGF-β, IL-6, IL-10 and tumor necrosis factor-α), growth factors and chemokines. These molecules have been shown to affect various potassium and calcium ion channels [143, 144]. Recently, our laboratory has demonstrated that secreted and/or exogenous cytokines and growth factors have significant effects on the electrophysiology and AP profile of cultured cardiomyocytes. In these experiments, MF conditioned medium (containing all the cytokines, growth factors, etc. secreted by MF in culture) or TGF-β treatment increased peak sodium current (I_{Na}), prolonged the APD, and promoted EADs in adult rat ventricular myocytes. This further supports the pro-arrhythmic effect of

MF in fibrotic tissues and also sheds some mechanistic insight underlying MF-myocyte interactions.

Altogether, several studies have suggested that MF could become a target to treat post MI arrhythmia [145-147]. While most of the treatments studied so far focus on reducing the number of MF, I proposed an alternative approach in Chapter 3: that transient genetic modification and expression of specific ion channels will make MF excitable and able to generate an AP. Our working hypothesis is that these newly-excitable MF will restore fast myocardium conduction and reduce arrhythmias in a heterocellular *in vitro* model of cardiac impulse propagation.

1.4 Thesis Overview

Traditional pharmacological and device therapies designed to treat arrhythmias have indeed reduced the number of deaths from VF over the last decade; yet, the treatment options remain suboptimal since they introduce additional complications. Further, while they may initially improve the quality of life, they treat the symptoms rather than the causes. Arguably, the causes are varied, and this may complicate the search for the ideal treatment and/or prevention of VF. In general, the causes of cardiac arrhythmia can be divided into two categories: pathogenic changes in the electrophysiology of the heart (functional determinants) and changes in the gross anatomy of the heart (structural determinants). Therefore, the overall objectives of my thesis are: (1) to understand how changes in hERG (I_{Kr}) affect the rotor dynamics and properties

of VF; and (2) to determine whether genetical modification of cardiac MF will alter the arrhythmogenic potential and/or consequences of the remodeling associated with fibrosis.

In Chapter 2, the role of hERG channel expression in impulse propagation is systematically studied in a NRVM monolayer model. I tested the hypothesis that increasing the expression level of the hERG channels will change spiral wave dynamics by increasing both its frequency and stability. In Chapter 3, I will present data to demonstrate that cardiac MF infected with adenoviral constructs encoding three ion channels (Kir2.1, $Na_V1.5$, and Cx43) restore conduction velocity, and reduce arrhythmias in an *in vitro* heterocellular monolayer model.

Finally in Chapter 4, I will discuss how the data presented in Chapters 2 and 3 lead to an advanced understanding of the ionic mechanisms of fibrillation, and provide insights into the development of potential pharmacological or cell therapy treatments for VF in the future.
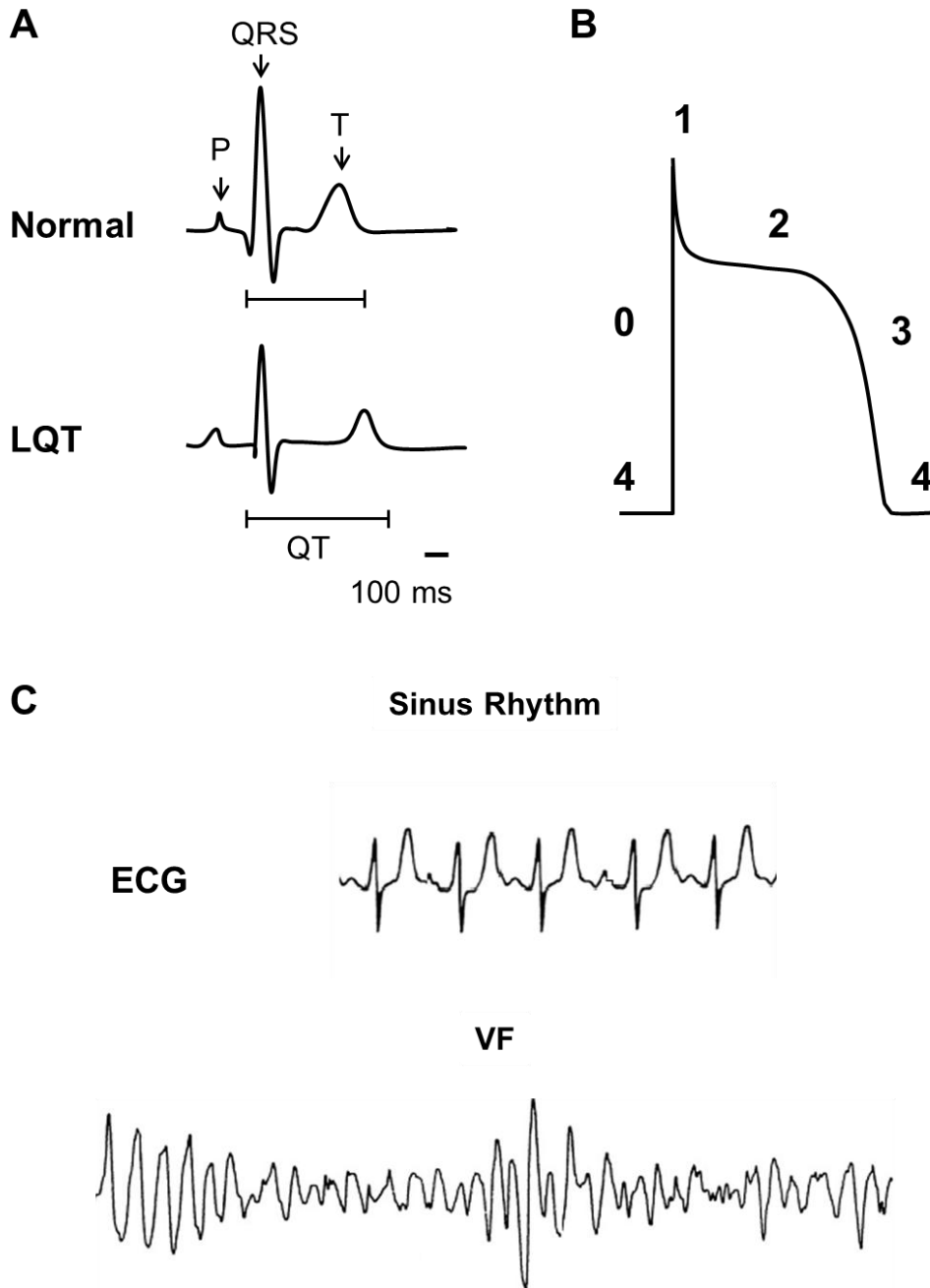
Figure 1.1. Electrocardiogram (ECG) and action potential. A. ECG traces represents a normal and Long QT (LQT) case. **B.** Action potential phase 0 to 4. **C.** ECG traces under sinus rhythm and ventricular fibrillation (VF).

A

Planar Wave

B

Concave Wave

C

Convex Wave

D
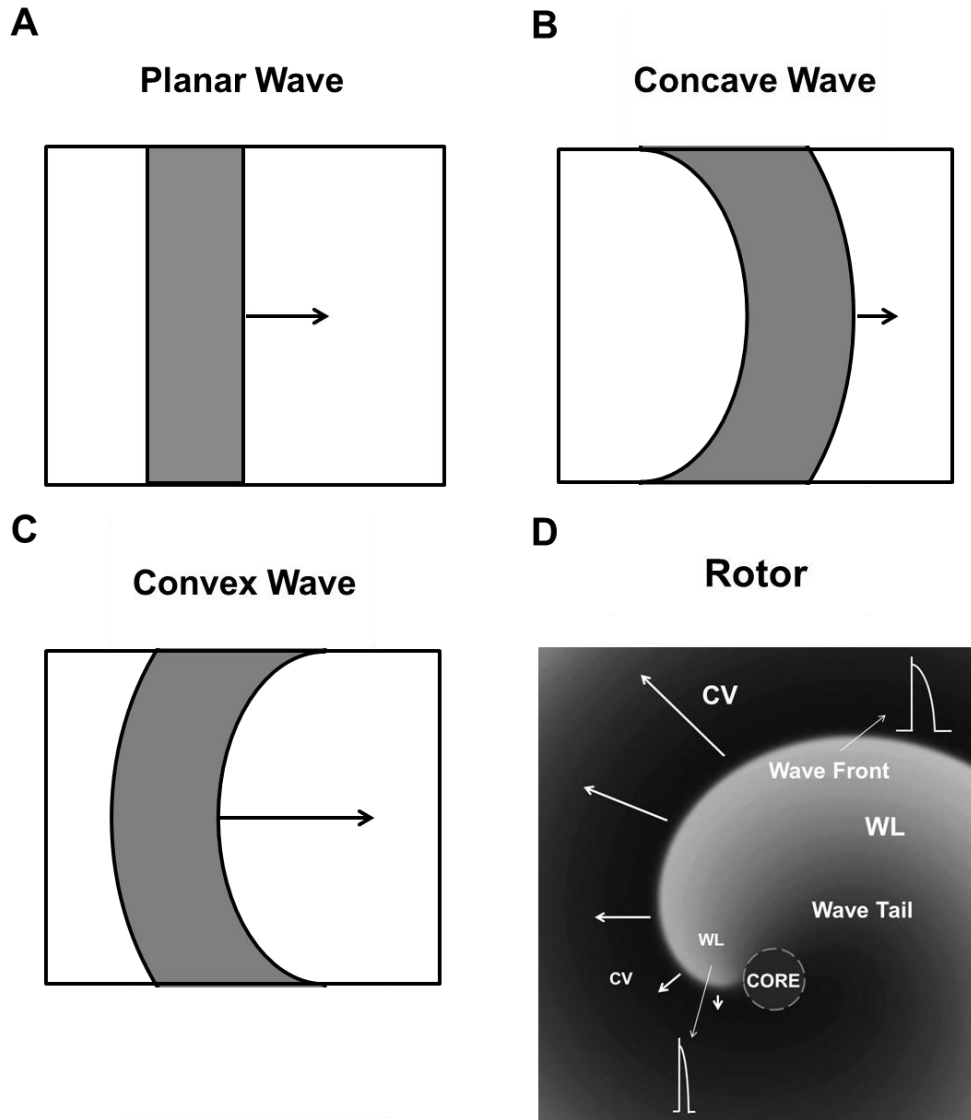
Rotor

Figure 1.2. Propagating wave in a 2D sheet. A. Planar wave. **B.** Concave wave. **C.** Convex wave. **D.** Rotor: electrotonic effect of the center of rotation (core) on conduction velocity (CV) action potential duration (APD) and wavelength (WL). Modified from [36, 148].
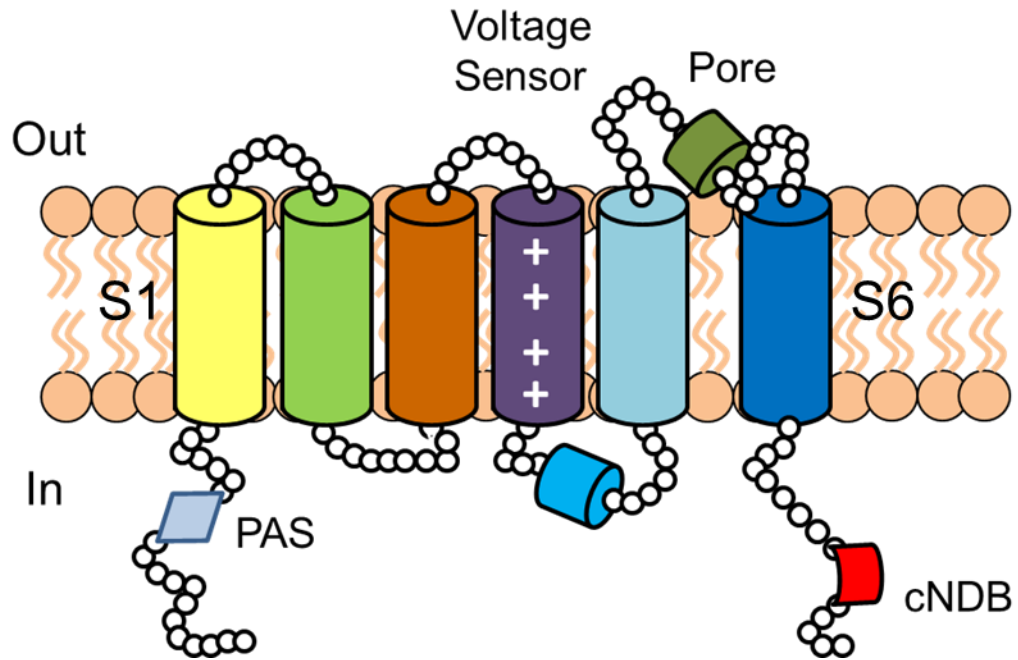
Figure 1.3. hERG structure. Schematic diagram of one subunit of hERG channel with six α-helical transmembrane domains, S1-S6, and cytoplasmic N-terminal and C-terminal domains. PAS: Per-Arnt-Sim; cNDB: cyclic-nucleotide-binding domain. Modified from [92].

CHAPTER 2

A MAJOR ROLE FOR HERG IN DETERMINING FREQUENCY OF REENTRY

IN NEONATAL RAT VENTRICULAR MYOCYTE MONOLAYERS

2.1 Abstract

The rapid delayed rectifier potassium current, I_{Kr}, which flows through the human ether-a-go-go-related (hERG) channel is a major determinant of the shape and duration of the human cardiac action potential (APD). However, it is unknown whether the time dependency of I_{Kr} enables it to control APD, conduction velocity (CV) and wavelength (WL) at the exceedingly high activation frequencies that are relevant to cardiac reentry and fibrillation. The objective is to test the hypothesis that upregulation of hERG increases functional reentry frequency and contributes to its stability. Using optical mapping, we investigated the effects of I_{Kr} upregulation on reentry frequency, APD, CV and WL in neonatal rat ventricular myocyte (NRVM) monolayers infected with GFP (control), hERG

(I_{Kr}), or dominant negative mutant hERG G628S. Reentry frequency was higher in the I_{Kr}-infected monolayers (21.12±0.8 Hz; n=43 vs 9.21±0.58 Hz, n=16; p<0.001), but slightly reduced in G628S-infected monolayers. APD_{80} in I_{Kr}-infected monolayers was shorter (>50%) than control during pacing at 1-5 Hz. CV was similar in both groups at low frequency pacing. In contrast, during high frequency reentry, the CV measured at varying distances from the center of rotation was significantly faster in I_{Kr}-infected monolayers than control. Simulations using a modified NRVM model predicted that rotor acceleration was due in part to a transient hyperpolarization immediately following the AP. The transient hyperpolarization was confirmed experimentally. Therefore, we conclude that hERG overexpression dramatically accelerates reentry frequency in NRVM monolayers. Both APD and WL shortening, together with transient hyperpolarization, underlies the increased rotor frequency and stability.

2.2 Introduction

Ventricular fibrillation is a major cause of sudden cardiac death. Evidence suggests that, in mammalian species ranging in size from the mouse to human, VF may be maintained by highly periodic reentrant waves called rotors [35, 37]. The spiral waves that emanate from high frequency rotors propagate through the ventricles, and undergo intermittent, spatially distributed wavebreaks resulting in complex patterns of conduction also known as fibrillatory conduction [30, 35]. While the existence of rotors has been known for years, the ionic mechanisms responsible for their behavior remain incompletely understood. Recently, it was

shown that the frequency and the stability of rotors are determined in great measure by the resting membrane potential (RMP) and the conduction velocity (CV), which are controlled by the dynamic interplay between the outward component of the inward rectifier potassium current (I_{K1}) and the rapid inward sodium current (I_{Na}) [76]. Other experiments have demonstrated that overexpression of the slow delayed rectifier current (I_{Ks}) does not affect reentry frequency, but significantly increases the incidence of fibrillatory conduction in cardiomyocyte monolayers [77]. However, the consequences of upregulation or gain of function in the rapid delayed rectifier current (I_{Kr}) on reentry frequency and dynamics have never been directly investigated either in the heart or any model system.

The human ether-a-go-go-related (hERG) potassium channel responsible for I_{Kr} is important in determining the shape and duration of the human cardiac action potential (AP) [92]. I_{Kr} suppression results in action potential duration (APD) prolongation, cardiac arrhythmias and sudden cardiac death [149]. hERG mutations are associated with chromosome 7-linked inherited long QT syndrome type 2 (LQTS2) [150]. In addition, drug induced LQTS is often the result of I_{Kr} blockade [149]. However, an arrhythmogenic phenotype is not limited to loss of function in I_{Kr}.

Recently, a gain-of-function mutation in hERG, N588K, was identified to be associated with short QT syndrome (SQTS) [98]. It provided evidence that upregulation of I_{Kr} could be arrhythmogenic. Thus, it seems reasonable to speculate that once a reentrant arrhythmia is initiated, I_{Kr} upregulation influences

its dynamics. However, while I_{Kr} contributes significantly to APD, and thus ventricular refractoriness and wavelength (WL ≈ APD x CV) at physiological heart rates, it is unknown whether its time dependency enables it to control the same parameters at the exceedingly high activation rates of cardiac reentry and fibrillation. Therefore the objective of this study was to systematically determine how expression levels of I_{Kr} affect the frequency, stability, and duration of rotors in 2-dimensional NRVM monolayers. We tested the hypothesis that through its direct effects of APD shortening, upregulation of hERG increases functional reentry frequency and contributes to its stability.

2.3 Materials and Methods

2.3.1 Isolation and Culture of NRVM Monolayers

The isolation and culture techniques are described elsewhere [77]. Briefly, hearts from 1 to 2 day old neonatal Sprague-Dawley rats (Charles River, Mass) were removed and collected in calcium and magnesium free Hanks' Balanced Salt Solution (HBSS). Then the ventricles were isolated, minced and enzymatically digested in a solution that contained 0.06% trypsin (Roche Applied Science) and 0.15% pancreatin (Sigma). After a two-hour preplating period, which helped avoid non-cardiomyocyte attachment, cells were cultured in M199 medium (Cambrex) with 10% fetal bovine serum (FBS) (Cellgro), 20 U/mL penicillin, 20 µg/mL streptomycin, and 100 µmol/L bromodeoxyuridine (Sigma). Finally, myocytes were plated in 35 mm tissue culture dishes at a density of 1×10^6 cells/dish for monolayers and at low density on 25 mm cover slips for

single cell patch-clamp experiments. To facilitate cardiomyocyte attachment, dishes were coated with human placental collagen type IV (Sigma). Cells were subsequently cultured at 37ºC, 5% CO_2.

2.3.2 Adenoviral Constructs

We generated adenoviral constructs containing WT or G628S cDNA sequence of hERG tagged with GFP, using the AdEasy vector system (Stratagene, La Jolla, CA). Viruses were purified using a kit (Virus Purification Kit, Clonetech) and the titer calculated (Rapid Titer Kit, Clontech) before multicellular preparations were infected with varying multiplicities of infection (MOI). MOIs of 200 and 30 were found to be optimal for uniform expression of WT and mutant hERG channels, respectively, based on the GFP level across the monolayer. An adenovirus carrying the sequence of GFP (Ad-GFP) at an MOI=10 served as control. All viral infections were performed after 48 hours in culture. After infection, the myocytes were cultured for an additional 48 hours to allow sufficient protein expression before mapping or patch-clamping.

2.3.3 Electrophysiology

In whole-cell patch-clamp experiments the bath solution was HBSS with Ca^{2+} and Mg^{2+} (Sigma); pH was adjusted to 7.4 with NaOH. Nifedipine (5 µM) and 4-AP (2 mM) were added to reduce extraneous ion currents. The pipette solution contained (in mM): 1 $MgCl_2$, 5 EGTA, 150 KCl, 5 HEPES, 5 Phosphocreatine, 4.5 K_2ATP, 2mM B-hydroxybutyric acid; pH was adjusted to 7.2 with KOH. Recordings were carried out at 37ºC using a MultiClamp 700B amplifier (Axon Instruments, Forest City, CA). After gigaseal formation and patch

break the tip potential was nulled and cell capacitive currents and series resistance were optimally (~80%) compensated. I_{Kr} currents were elicited with 0.5-second depolarizing steps applied in 10 mV increments from a holding potential of -60 mV to +50 mV. I_{Kr} was derived by subtracting currents recorded in the presence of E4031 (1 μM) from control currents.

APs were recorded from individual myocytes using the current-clamp mode of the MultiClamp 700B amplifier after gigaseal formation and patch break. Stimulus pulses (1-2 ms duration) were generated using a World Precision Instruments DS8000 stimulator. The bath solution was HBSS with Ca^{2+} and Mg^{2+} (Sigma). The pipette solution contained (in mM): 1 $MgCl_2$, 5 EGTA, 150 KCl, 5 HEPES, 5 Phosphocreatine, 4.5 K_2ATP, 2mM B-Hydroxybutyric acid. Recordings were carried out at 37 °C.

2.3.4 Optical mapping

High-resolution optical mapping was conducted using a CCD camera (80x80 pixels, SciMeasure) (Figure 2.1). Cultured dishes were placed on a heating chamber connected and maintained at 37°C. Monolayers were superfused with HBSS (in mM/L): 1.6 $CaCl_2$, 5.4 KCl, 0.8 $MgSO_4$, 0.4 KH_2PO_4, 4.2 $NaHCO_3$, 136.9 NaCl, 0.3 $NaHPO_4$, 5.5 D-Glucose, and 10 HEPES; pH 7.4. Electrical wave propagation was recorded by staining the cells with 40 μM/L di-8-ANEPPS (Molecular Probes) for 15 minutes. We obtained 5-seconds movies at 200 frames/s and 2-seconds movies at 500 frames/s.

2.3.5 Pacing Protocol

Monolayers were paced using 5-ms pulses at 2X threshold through a thin bipolar electrode. Incremental pacing started at 1 Hz, until loss of 1:1 capture or induction of sustained reentry. The I_{Kr} blocker, E4031 (1 µM) was superfused when indicated.

2.3.6 Data Analysis

Single Cell Electrophysiology: We used commercially available software (pCLAMP, version 10.2; Axon Instrument, Forster City,CA). I_{Kr} peak pulse currents were measured using the Clampfit subroutine of the pCLAMP software, normalized to cell capacitance, and plotted against voltage.

Optical Movies: The methods for the construction of phase maps, activation maps and time-space plots have been described in great detail previously [58, 76, 77, 85, 151]. Ensemble averaging at each pixel was performed over 5 or more propagating wavefronts synchronized with stimuli. Background fluorescence was subtracted from each frame, and spatial (3x3 pixels) and temporal (7 pixels) conical convolution filters were applied. Dominant frequency (DF) maps and phase maps were constructed in monolayers showing sustained reentry as described [152]. Optical APDs were measured at 80% repolarization. The local CV was measured as described.[59] Briefly, the distributions of activation times (50% of upstroke) for the spatial regions of 5x5 pixels were fitted with the plane, and gradients of activation times gx and gy were calculated for each plane along the *x* and *y* axes, respectively. The magnitude of the local CV was calculated for each pixel as $(g_x^2 + g_y^2)^{-1/2}$. Mean values and

standard deviations for CV and APD were calculated for the entire visible

surfaces and for sequential activations. During pacing, wavelength (WL) was

calculated as WL = APD x CV. However, it is well known that during functional

reentry both APD and CV vary greatly as a function of distance from the center of

rotation (core). Therefore, during sustained reentry, the WL was measured from

the phase maps as the expanse between the wavefront and the end of the

repolarization wavetail, at a fixed distance of 10 mm from the core (Figure 2.2).

Method of measuring the wavelength (WL): As shown in Figure 2.2, WL

during reentry was defined by the length of the black line drawn on the phase

map 10 mm from the center of rotation (white circle) and perpendicular to the

tangent at the wavefront (blue). In both experiments (panel A) and simulations

(panel B) I_{Kr} upregulation reduced WL significantly during sustained reentry.

2.3.7 Computer Simulations

The computer simulation was performed by Dr. Makarand Deo. We have

modified an existing mathematical model of the neonatal rat myocyte published

by Korhonen et al [153]. This model is unique in that the cytosolic Ca^{2+} is a

function of temporal as well as spatial coordinates. Due to the lack of t-tubules

[154], calcium ions entering into the cells via membrane channels must diffuse a

small distance through the cytosol before reaching the sarcoplasmic reticulum

and trigger the excitation-contraction coupling machinery. Some ionic current

components were modified to reproduce the AP morphology and the restitution

properties recorded from the experiments performed in our laboratory. Other

formulations in the Korhonen model remain unchanged [153].

44

2.3.8 Statistical Analysis

Data are expressed as mean±SEM. Patch-clamp data were analyzed by two-way ANOVA with Bonferroni post-tests. Analyses of reentry frequency were performed using one-way ANOVA with Tukey's multiple comparison test. A Student's *t test* with Welch-correction was used to analyze the average APD and CV, as well as the maximal diastolic potential (MDP) data. $p < 0.05$ was considered to be significant.

2.4 Results

2.4.1 hERG overexpression upregulates I_{Kr} in NRVM

At 200 or 30 MOI of adenoviral expression, we observed maximal GFP-tagged WT or G628S mutant hERG channel expression in NRVM monolayers. Spatially uniform protein expression was consistently confirmed by fluorescent microscopy as illustrated in Figure 2.3A.

Figure 2.3B illustrates on the top the voltage-clamp protocol (see Methods) used to determine the voltage dependence of I_{Kr} density. The same panel shows superimposed representative I_{Kr} traces recorded from single NRVM infected with Ad-GFP (middle) or Ad-hERG (bottom). I_{Kr} current was appreciably increased in the Ad-hERG infected myocytes when compared to control. As summarized in Figure 2.3C, Ad-hERG infected cells have a significantly steeper current density vs voltage (IV) relation than Ad-GFP control. At 0 mV, outward current was 14.7 ± 1.98 pA/pF in cells expressing hERG versus 2.8 ± 0.53 pA/pF in cells expressing GFP ($p < 0.001$). As shown in panel D, the peak tail current

also increased significantly in Ad-hERG myocytes. However, activation of the normalized tail current showed no difference between the two groups in terms of voltage dependence (Figure 2.3E).

2.4.2 I_{Kr} upregulation accelerates reentry frequency

Sustained functional reentry could be obtained from monolayers infected by Ad-GFP, Ad-hERG and Ad-G628S. Figure 2.4A shows phase maps of single rotors generating spiral waves in Ad-GFP control (left), I_{Kr}-overexpressing (middle), and G628S-overexpressing (right) monolayers. The corresponding color activation maps and time space plots demonstrating the stability and reproducibility of the respective reentry patterns are presented in Figures 2.5 and 2.6. Figure 2.5 presents color activation maps of sustained reentry corresponding to the phase maps shown in Figure 2.4. Neonatal rat ventricular monolayers were infected with Ad-GFP, Ad-hERG, or Ad-G628S. In Figure 2.6, we illustrate the original optical signals and corresponding time-space plots for the same experiments. Each time-space plot (bottom) was constructed along the horizontal white line drawn on the equivalent reentry snapshot (top). Please note that Ad-hERG significantly abbreviated the spatial extension of the excited state (white) and greatly accelerated reentry frequency, as reflected by the large increase in the number of rotations in the respective time-space plot. In contrast Ad-G628S appreciably increased the spatial extension of the excited state and reduced the number of rotations in the time-space plot.

The graph in Figure 2.4B compares the ranges of individual rotation frequencies of control monolayers with that of I_{Kr}-overexpressing and G628S-

overexpressing monolayers. The mean values are shown as horizontal bars for each experimental group. The average frequency is significantly higher in I_{Kr}-overexpressing monolayers than GFP controls (21.12 ± 0.81, n = 43; vs. 9.21 ± 0.58 Hz, n = 16; p<0.001); whereas the frequency in the G628S monolayers is slightly lower (6.14 ± 0.3 Hz, n=17; NS vs GFP).

To confirm the involvement of I_{Kr} overexpression on the acceleration of rotor frequency, E4031, a specific I_{Kr} blocker, was superfused at a concentration of 1μM in 23 monolayers infected with Ad-hERG. As shown in Figure 2.7, E4031 dramatically reduced the frequency of rotation (22.75 ± 1.24 vs. 9.82 ± 0.74 Hz, p<0.05). This effect was partially reversed after a 5min washout period (16.72 ± 1.03 Hz, p<0.05 vs. E4031).

2.4.3 Wavelength shortening underlies I_{Kr}-induced rotor acceleration

To elucidate the mechanism by which hERG accelerated reentry frequency, we first investigated the effect of I_{Kr} overexpression on APD and CV during pacing at varying cycle lengths. From high-resolution APD maps, APD_{80} was measured during 1:1 activation in 11 control and 8 I_{Kr} overexpressing monolayers. Figure 2.8 shows examples of single pixel recordings at pacing cycle lengths between 1000 and 200 ms. The data demonstrates the excellent signal-to-noise ratio, which allowed accurate APD measurements. As shown in Figure 2.9A, I_{Kr} expression reduced the APD_{80} by more than 50% when compared with control during pacing at cycle length between 200 and 1000ms (p<0.01). On the other hand, as shown in Figure 2.9B, the mean CV of Ad-hERG expressing monolayers was similar to Ad-GFP monolayers at all pacing cycle

lengths. Moreover, the wavelength (WL = APDxCV), was significantly shorter in the Ad-hERG monolayers than the control group at all pacing cycle length (Figure 2.9C).

We also plotted the rotation frequency in each monolayer as a function of the respective mean APD_{80} in both control and I_{Kr} overexpressing groups. As shown in Figure 2.10A, the relationship was very steep and highly significant for the Ad-hERG group. In some monolayers, hERG overexpression reduced APD_{80} to less than 30 ms, which enabled rotation frequencies of 25 Hz or higher. In contrast in the Ad-GFP group, although the slope of the relationship was significant, it was much less steep and the minimal APD_{80} was 60ms and the highest rotation frequency was 12.6 Hz.

As demonstrated previously [58, 76, 155], during functional reentry, the CV decreases as the curvature of the wavefront increases toward the center of rotation (core). We therefore measured the CV as a function of distance from the core to determine whether I_{Kr} affected that relationship in the same manner as I_{K1} overexpression does [76]. We determined the role of wavefront curvature in determining the changes of reentry frequency and dynamics secondary to hERG modification, as illustrated in panel A of Figure 2.11: 1) A snapshot of the phase movie showing a rotor with a singularity point (SP) at its pivoting tip was randomly selected for each of a total of n=9 monolayers in each group. 2) In each snapshot we determined by visual inspection the orientation of the wavefront tip in the immediate vicinity (i.e., within 3 pixels) of the SP. 3) We then drew a line in that orientation across the SP. 4) Subsequently, we drew a second line

48

perpendicular (90 degree angle) to the SP crossing line and extended it to approximate the first ½ winding of the wavefront; i.e., to the nearest transition between phases blue and purple in the phase map. 5) We measured the length of the second line. 6) We took that length being equivalent to the diameter of a hemi-circle approximately delineating the wavefront in its first ½ winding and therefore as being inversely proportional to its curvature at that location.

In Figure 2.10B we summarize data for 21 Ad-hERG monolayers and 12 Ad-GFP monolayers. As expected, CV increased gradually as a function of distance from the core in both groups. However, the Ad-hERG monolayers showed a lager CV at all distances from the core as compared with the Ad-GFP monolayers ($p<0.05$). Similarly, the curvature of the wavefront near its pivot point was determined and compared between groups (Figure 2.11). Curvature was larger in the Ad-hERG monolayers than Ad-GFP controls. Taken together, this analysis showed that during reentry, excitability and CV are higher in the Ad-hERG monolayers than in the Ad-GFP control.

Figure 2.10C shows a comparison of WL measured during reentry as the expanse between the wavefront and the end of the repolarization wavetail (see Figure 2.2 and Method). As expected, the WLs were significantly shorter in the Ad-hERG group. They ranged between 2.75 and 6.89 mm, whereas control WLs ranged between 7.88 and 22.22 mm ($p<0.05$). Altogether the data presented thus far suggested that APD and WL shortening, together with increased CV underlie rotor acceleration in I_{Kr}-upregulated monolayers.

2.4.4 Numerical Simulations

To gain further mechanistic insight into the effects of hERG overexpression on rotor frequency and stability, we conducted computer simulations at the single cell level, as well as in 2D using a modified model of the NRVM. Figure 2.12A shows APs elicited in the single cell model by pacing at 1 Hz in control, and hERG increase (I_{Kr} 5.21X). As expected, APD abbreviated upon I_{Kr} upregulation. Interestingly, in the I_{Kr} 5.21X model the AP was followed by a highly reproducible transient hyperpolarization (see also Figure 2.13A).

We investigated the consequences of I_{Kr} upregulation on rotor dynamics in a 2D monolayer model. As shown in Figure 2.12B, the reentry frequency was significantly increased from 12.8 Hz in control to 18.5 Hz in I_{Kr} 5.21X, which was consistent with the experimental result shown in Figure 2.4. Similar to experiments, overexpressing I_{Kr} (5.21X) in the simulations increased the CV during reentry at all distances from the core compared with the controls (Figure 2.12C).

To determine whether the changes seen in Figure 2.12A had any role in I_{Kr} overexpression-induced rotor acceleration, we subjected the single cell model to pacing at varying frequencies (from 1 to 20 Hz). We surmised that at the highest frequencies the ensuing APD shortening and transient hyperpolarization should increase I_{Na} availability and therefore excitability. To test that hypothesis, the fast inward sodium current (I_{Na}) was recorded in two sets of simulations (control, and I_{Kr} 5.21X, respectively), and peak I_{Na} was plotted against pacing frequency for each case. As a negative control, in yet another set of simulations

we scaled I_{Ks} (25X) while I_{Kr} was kept unchanged. Differences in cell excitability were investigated in both sets in terms of peak I_{Na} amplitude. As shown in Figure 2.13A, while I_{Kr} upregulation produced a concomitant transient hyperpolarization after the abbreviated action potential (left), I_{Ks} upregulation did not result in membrane hyperpolarization (top right). Therefore, as shown in Figure 2.14B, the effects of I_{Ks} upregulation on I_{Na} availability were substantially less at any given activation frequency, compared with the effects of I_{Kr} upregulation. The difference was most significant at the highest frequencies between 12 and 20 Hz. This could explain the effect of I_{Kr} upregulation on CV increase during high frequency reentry (Figure 2.10B) but not low frequency pacing (Figure 2.9B).

As discussed above in Figure 2.10A, the slope of the line defining the relationship between rotation frequency and APD was steeper in the case of hERG overexpression than in control. We surmised that such an increase in the sensitivity of rotation frequency to APD abbreviation was the result of the transient hyperpolarization. Therefore, we studied the effects of premature stimuli (S1-S2 protocol) in single cell, 1D cable and 2D monolayer models (Figure 2.14). In Panel C of Figure 2.13, a single I_{Kr} 5.21X cell was paced at 2 Hz (S1) for 10 seconds followed by a premature stimulus (S2) at varying intervals. It is clear from that graph that at the shorter S2 intervals, more I_{Na} was activated in I_{Kr} 5.21X model compared to control. This increase in peak I_{Na} disappeared when the transient membrane hyperpolarization was suppressed by clamping the maximal diastolic potential (MDP) to -70 mV. As illustrated in panel A of Figure 2.14, in the 1D cable of 10 mm in length, this increase in I_{Na} translated into

increased CV which again disappeared when the MDP was clamped to -70 mV. We further verified the role of the transient hyperpolarization during reentry in 2D monolayer models by clamping the MDP to various voltages. As expected, the frequency of reentry was progressively reduced with increasing the value of MDP (see panel B of Figure 2.14. The clamped voltages in these simulations covered the range of our experimentally observed MDPs and thus clearly underscored the role of the transient hyperpolarization in addition to the APD abbreviation in increasing the rotor frequency and CV during reentry in I_{Kr} upregulation.

2.4.5 I_{Kr}-Induced transient hyperpolarization in NRVM

To determine whether a transient hyperpolarization predicted by simulations occurred experimentally in the in NRVM, we obtained single cell action potential recordings using current clamp. In Figure 2.15A, we present 2 representative action potential recordings at a pacing cycle length of 2000 ms. Consistent with the simulation results, APD shortening and a transient hyperpolarization were demonstrated in the myocytes infected with Ad-hERG when compared to Ad-GFP. In Figure 2.15B, we quantified the MDP after each action potential in Ad-hERG (-67.6±0.98 mV; n= 8) and Ad-GFP cells (-63.9±1.11 mV; n=6; p=0.03). As shown in Figure 2.15C, APD was measured at three different levels (APD_{30}, APD_{50} and APD_{80}) and showed a significant reduction when hERG was overexpressed. Taken together, these results demonstrated that APD shortening and transient hyperpolarization are both important consequences of I_{Kr} overexpression.

2.5 Summary

We have investigated the consequences of I_{Kr} upregulation on electrical impulse propagation and reentry dynamics in 2-D biological and numerical models. The most important results in this chapter are as follows: 1. I_{Kr} overexpression significantly increased the frequency of reentry. 2. During pacing at 1-5Hz, I_{Kr} overexpression shortened APD and WL more than 50%, but did not affect the CV. 3. During sustained reentry, rotation frequency demonstrated a steep and highly significant dependence on I_{Kr} upregulation-induced shortening of APD. The CV was significantly larger in the hERG group vs. the control group at all distances from the core. In addition, the WL was significantly shorter in Ad-hERG monolayers than in control. 4. Computer simulations and single cell action potential recordings demonstrated that APD shortening and the transient hyperpolarization after each AP in hERG overexpressing NRVM increased the INa availability, which contribute to the increased rotor frequency.

2.6 Clinical Relevance

Advances in pharmacological treatment of VF require a detailed study of the molecular and ionic mechanisms underlying cardiac excitation and its frequency dependence. There is currently a debate on whether block of I_{Kr} is arrhythmogenic, or is only arrhythmogenic in a subset of patients with a genetic predisposition [156]. Further increases in I_{Kr} have shown to be associated with short QT syndrome (SQTS). Patients with this syndrome have been shown to have a high incidence of syncope, sudden cardiac death (SCD), and

supraventricular arrhythmias [157]. Our experiments show that increased hERG can lead to fast and stable reentry, which could be the mechanism underlying arrhythmias in SQTS patients. Therefore, specific hERG blocker might be beneficial to some patients with an upregulation in hERG or with SQTS.

2.7 Study Limitations

The effect of hERG was examined in the NRVM monolayer model, which allowed us to overexpress hERG channel and study its effect on reentry dynamics in a highly controlled environment. However, by overexpressing the hERG channel alone we have not considered the importance that the regulatory β-subunits have in reconstituting native I_{Kr}, or their role in controlling reentry frequency [158]. Further, the consequences of channel expression in neonatal rodent myocytes are likely to be different from those in human adult myocytes since the ionic profile is different. Also, the closeness of the RMP to the K^+ equilibrium potential in normally polarized adult cardiomyocytes would substantially diminish the contribution of the transient hyperpolarization to the overall effect observed in NRVM. However, reentry typically occurs in association with ischemia/reperfusion injury — a situation in which external K^+ is usually elevated — therefore, depolarization of the RMP may increase the relevance of the latter mechanism in the adult heart. Finally, the conclusions that have been drawn from this study are only conceptual and mechanistic in relation to the cardiac fibrillatory process. In no way do we attempt to relate them to the clinical

setting. Further studies in translational models would be necessary before any extrapolation to humans can be made.

2.8 Conclusion

This is the first study to systematically evaluate the role of I_{Kr} in the frequency and stability of reentry. We demonstrate that hERG overexpression dramatically accelerates reentry frequency in NRVM monolayers. APD shortening and transient hyperpolarization induced increase in excitability are the mechanisms underlying reentry acceleration.

2.9 Acknowledgements
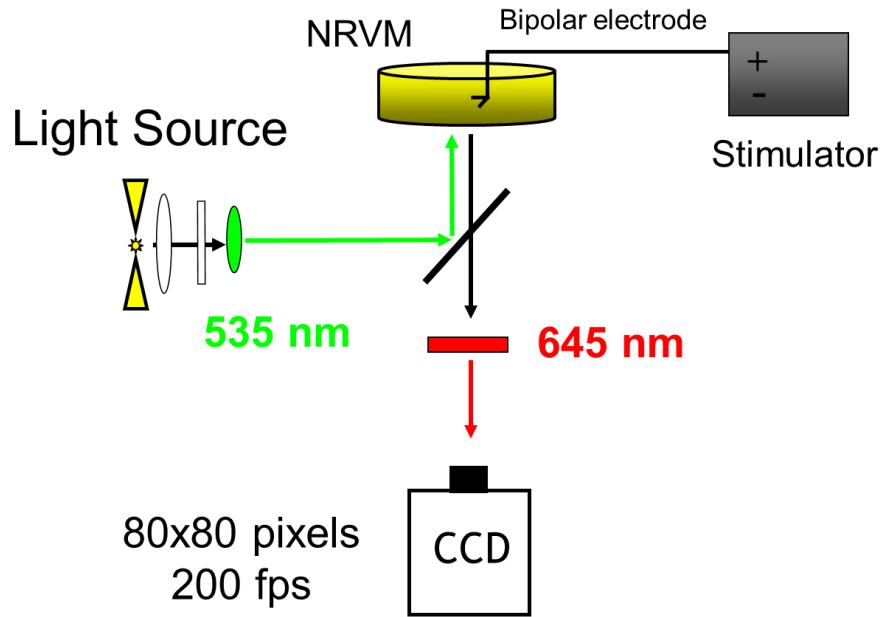
Figure 2.1 Schematic representation of the optical mapping setup. NRVM: neonatal rat ventricular myocytes; CCD: charge-coupled device.
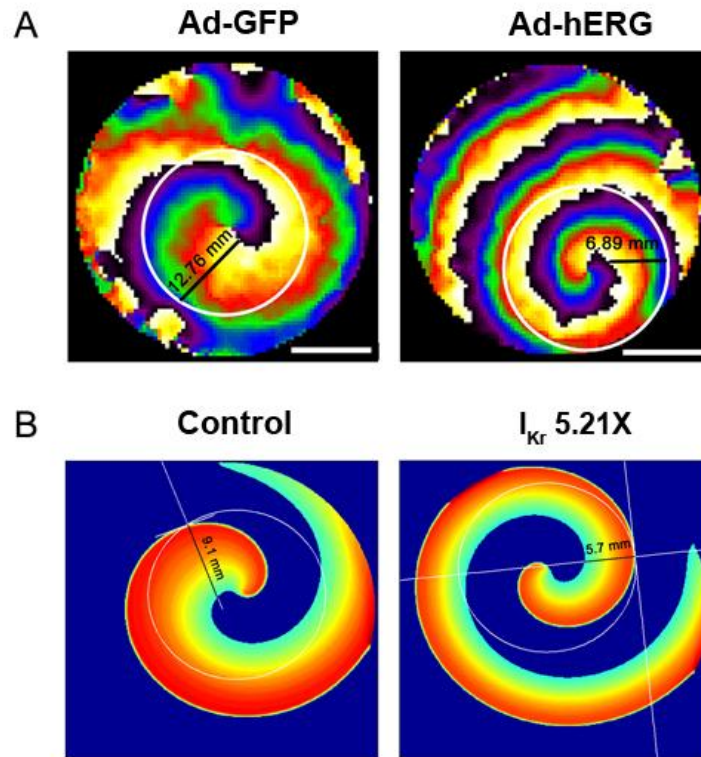
Figure 2.2. Wavelength measurement in experiments and simulations. A. Snapshots of the phase movies in Ad-GFP and Ad-hERG infected monolayers. White circles indicated the distance of 10 mm from the center of the reentry. In each panel, WL is given by the length of the black line extending between the wavefront (blue) and the end of repolarization wavetail (yellow). Scale bar: 10 mm; **B.** Snapshots of the voltage map in control and I_{Kr} 5.21X monolayers in simulation.
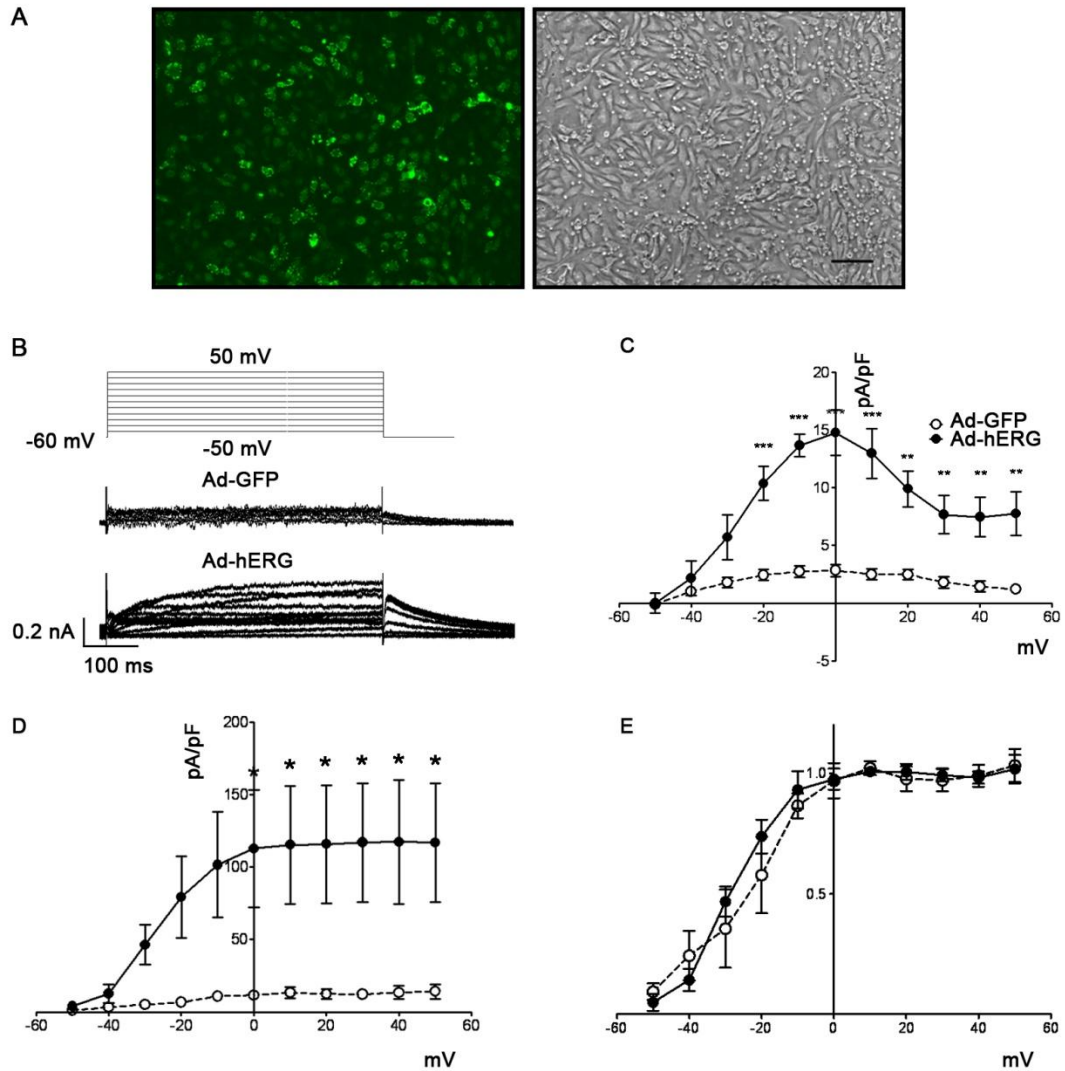
Figure 2.3. Adenoviral expression of hERG protein in neonatal rat ventricular cardiomyocytes after 48 hours of infection. A. GFP-tagged WT hERG channel expression. Left: fluorescent micrograph of a 4-day-old neonatal rat ventricular myocyte monolayer 48 h after viral infection. Right: corresponding phase contrast micrograph. Scale bar = 100 μm. **B**. Voltage clamp protocol (top) and representative examples of currents from Ad-GFP (middle) and Ad-hERG (bottom) infected myocytes. **C.** I-V relationship of the E4031-sensitive current normalized to cell capacitance in neonatal rat ventricular myocytes infected with Ad-GFP (open circles; n=5) and Ad-hERG (filled circles; n=5). ***p < 0.001, **p < 0.01, *p < 0.05; Ad-hERG vs. Ad-GFP, two-way ANOVA with Bonferroni post-tests. **D.** I-V relationship of the peak tail currents. **E.** Normalized peak tail currents from Ad-GFP and Ad-hERG myocytes. The two curves are not different statistically.
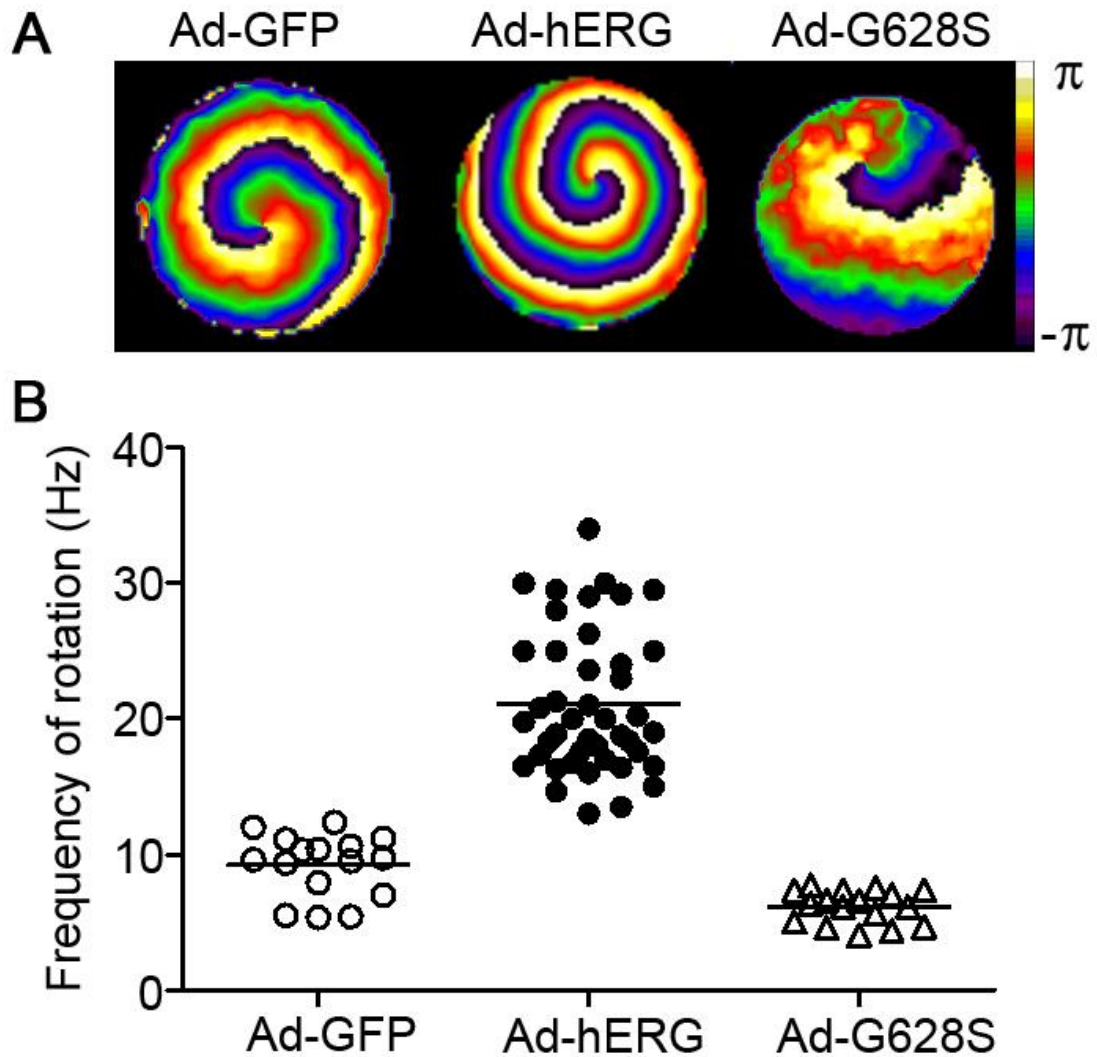
Figure 2.4. Effects of hERG infection on reentry frequency in NRVM monolayers. A. Snapshots from representative optical mapping movies in monolayers infected with Ad-GFP (left), Ad-hERG (middle), or Ad-G628S (right). **B.** Reentry frequencies in individual monolayers infected with Ad-GFP (open circles), Ad-hERG (closed circles; p<0.05 vs. GFP), or Ad-G628S (open triangles; NS vs. Ad-GFP; p<0.05 vs. Ad-hERG). Horizontal bars represent mean values. One-way ANOVA with Tukey's multiple comparison test.
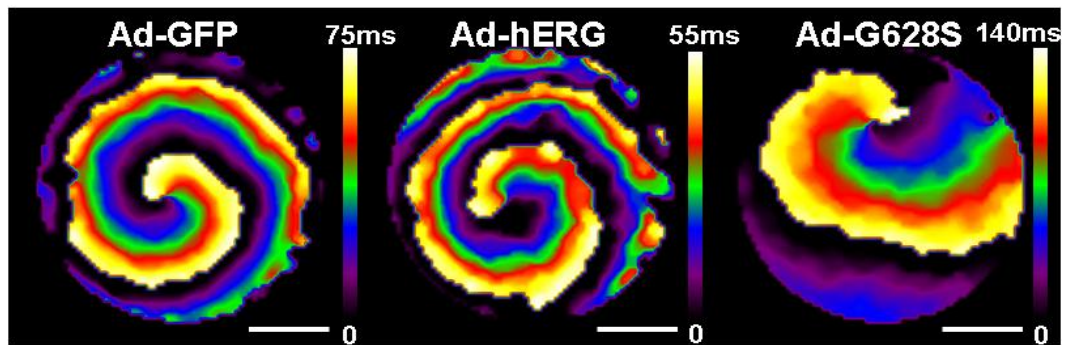
Figure 2.5. Activation maps of the NRVM monolayers infected with Ad-GFP, Ad-hERG, or Ad-G628S. Scale bar on the right of each map indicates different time point as shown in different color. Scale bars in white: 10mm.
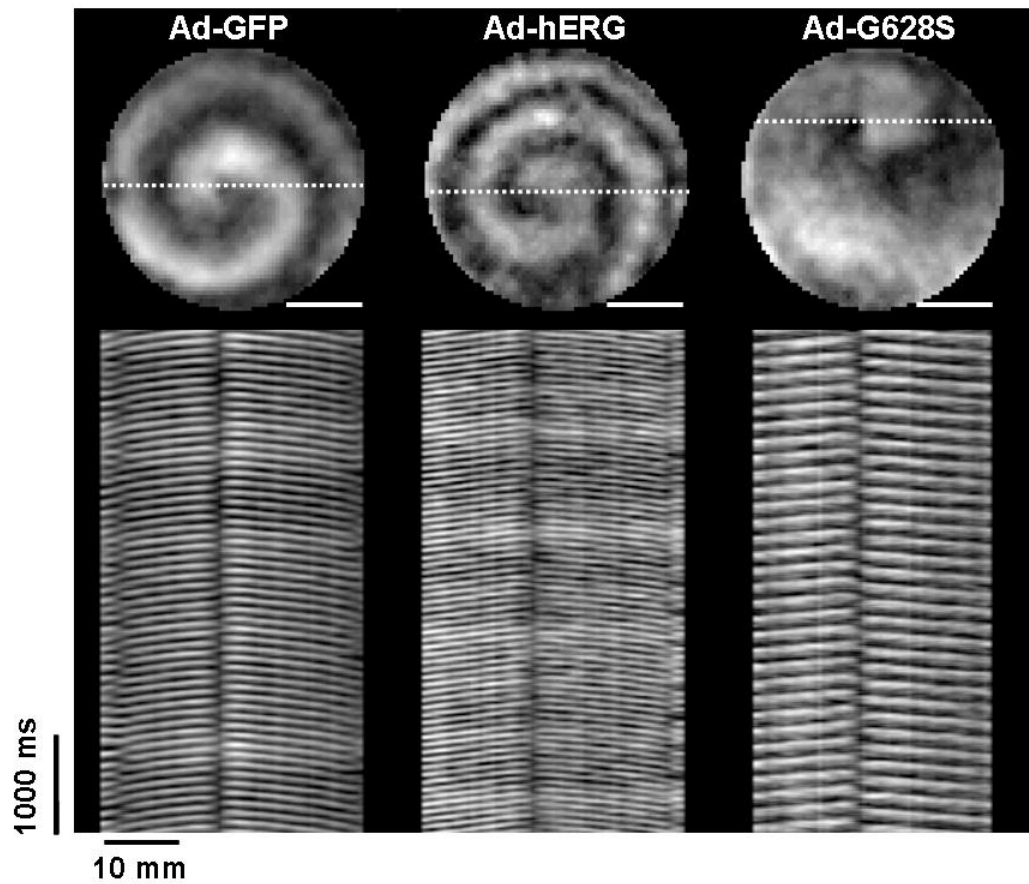
Figure 2.6. Optical signals and time-space plot (TSP) show the singularity points in monolayers infected with Ad-GFP, Ad-hERG, or Ad-G628S. TSPs were constructed for activity recorded along the horizontal white lines in the optical recordings. Scale bars in white: 10mm.
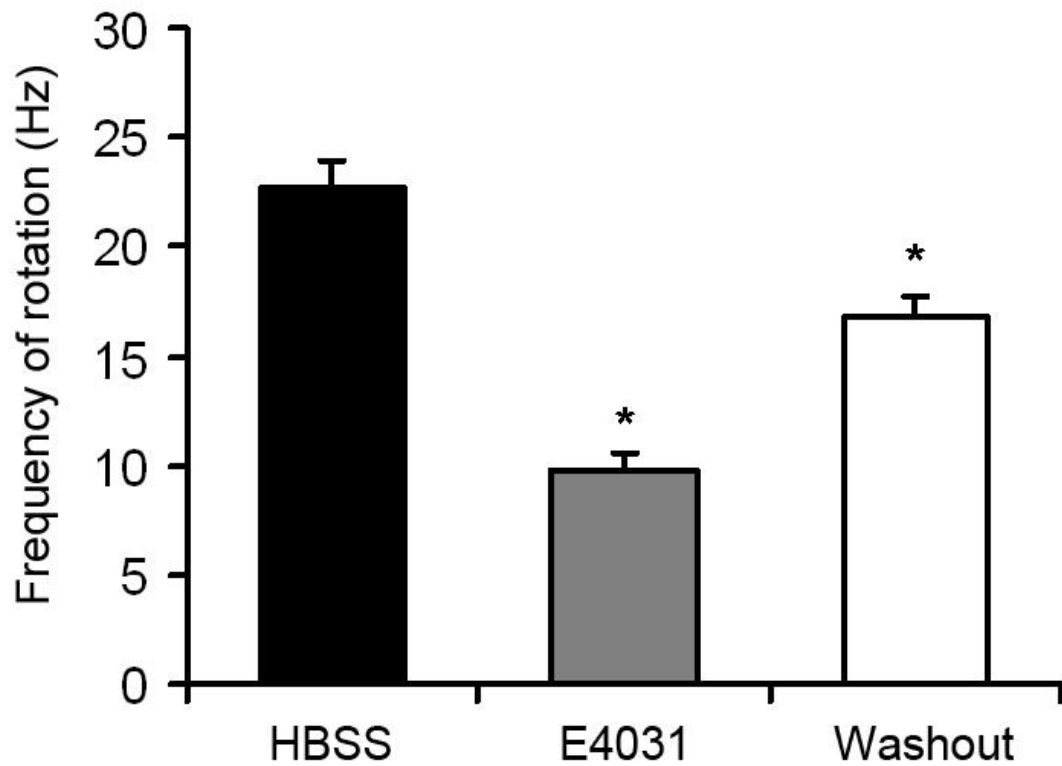
Figure 2.7. Effect of E4031 on reentry frequency in I$_{Kr}$ monolayers. Reentry frequencies of hERG overexpressing monolayers before (black) and after (grey) superfusion of E4031; and reentry frequency after 5 min washout (white). One-way ANOVA with Tukey's multiple comparison test.
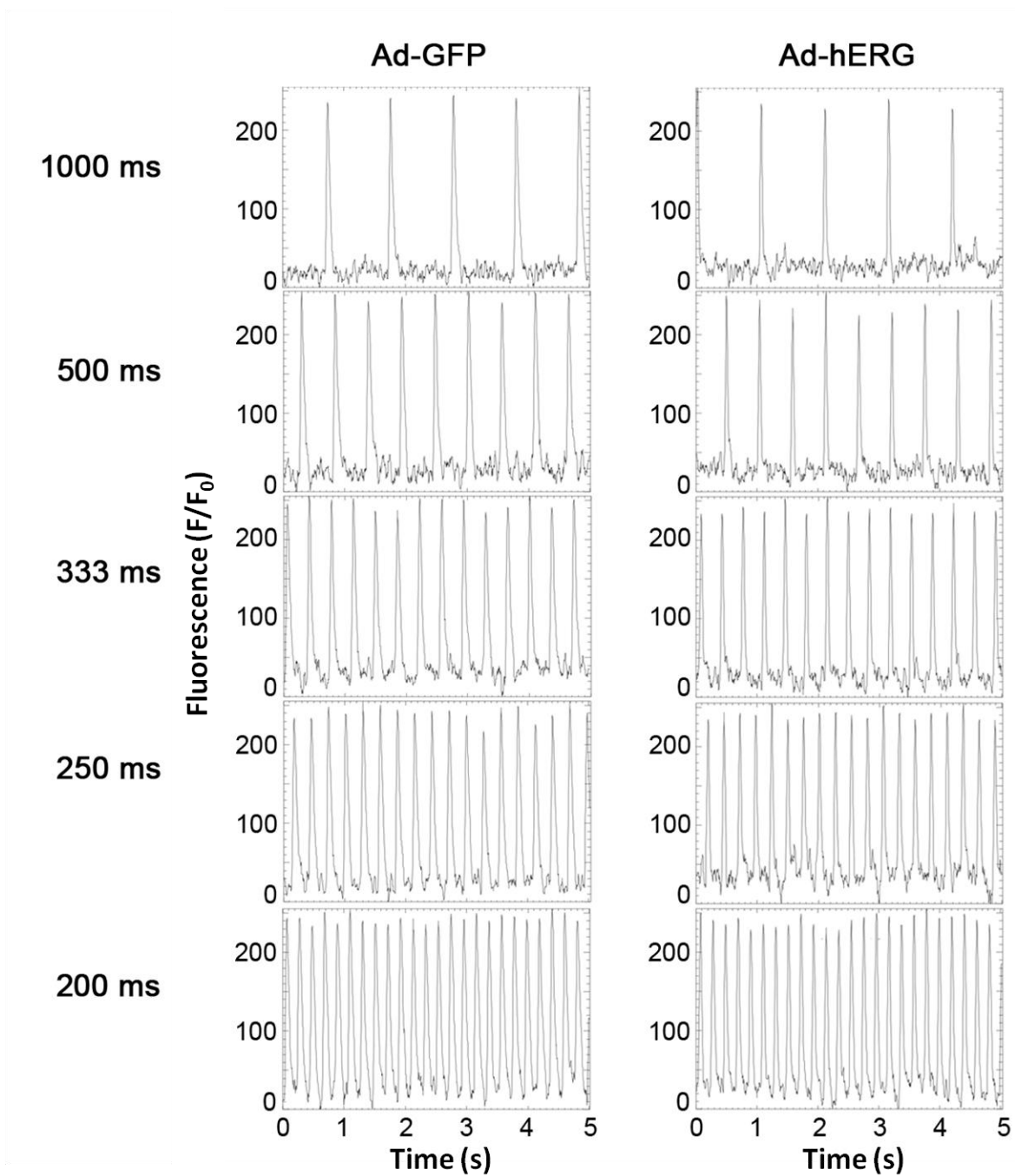
Figure 2.8. Single pixel recordings from Ad-GFP and Ad-hERG infected monolayers under pacing cycle length of 1000ms, 500ms, 333ms, 250ms, and 200ms.
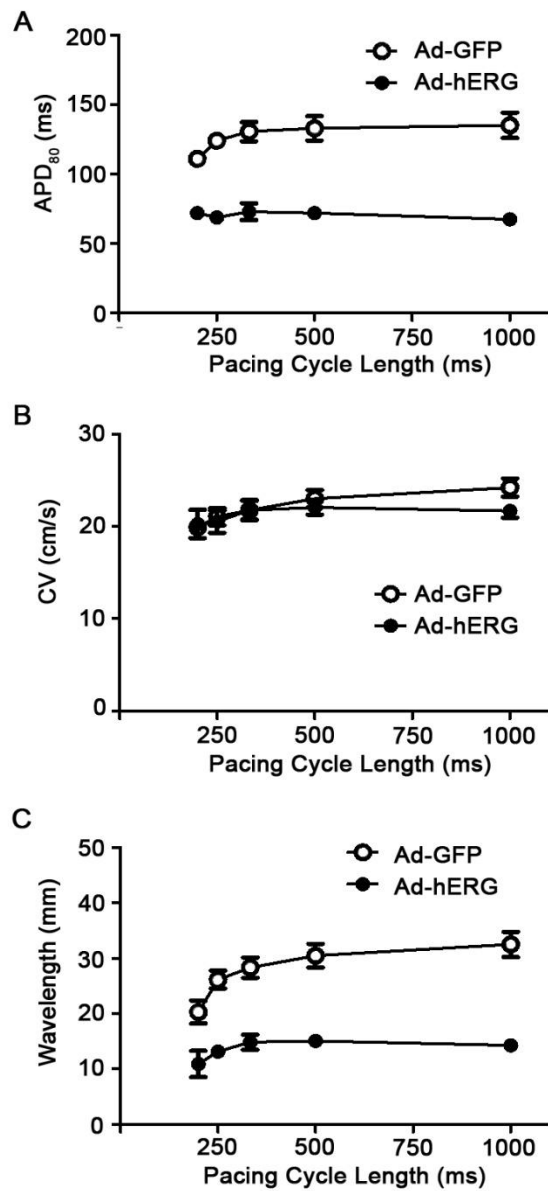
Figure 2.9. Effects of hERG overexpression on action potential duration (APD), conduction velocity (CV) and wavelength in monolayers paced at varying frequencies. A. Frequency dependence of APD_{80}. Mean values are statistically different ($p<0.05$). **B.** Frequency dependence of CV. Control values are not significantly different (NS) from Ad-hERG values at any pacing frequency; **C.** Frequency dependence of wavelength (WL=CV x APD). Mean values are significantly different at all pacing cycle lengths ($p<0.05$)

A. $y = -0.5174x + 40.114$
$R^2 = 0.9025$

$y = -0.0806x + 16.255$
$R^2 = 0.8991$
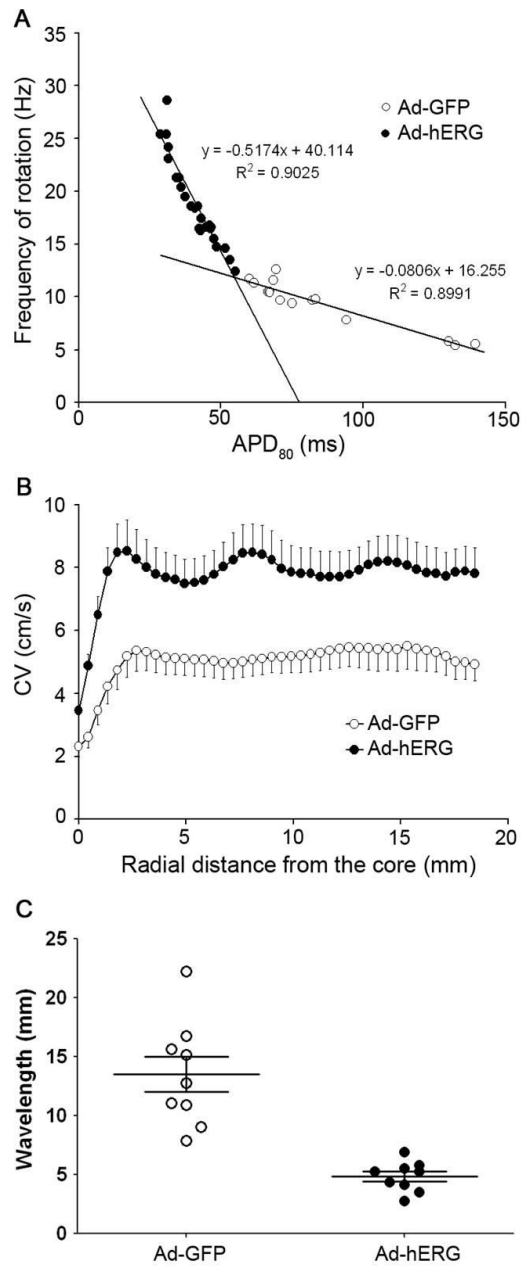
Figure 2.10. Effects of hERG overexpression on mean APD, CV and WL during sustained reentry in Ad-GFP (open symbols) and Ad-hERG monolayers (closed symbols). A. Rotation frequency as a function of APD_{80}. The regression lines relating frequency to APD is significantly steeper in Ad-hERG monolayers than control ($p<0.05$). Solid lines indicate linear regressions. **B.** CV as a function of distance from the center of rotation (core). CV is significantly higher in Ad-hERG than Ad-GFP infected monolayers at all distance from the core during reentry ($p<0.05$). **C.** Wavelength of reentry. The difference is statistically significant between Ad-GFP and Ad-hERG ($p<0.05$).

65
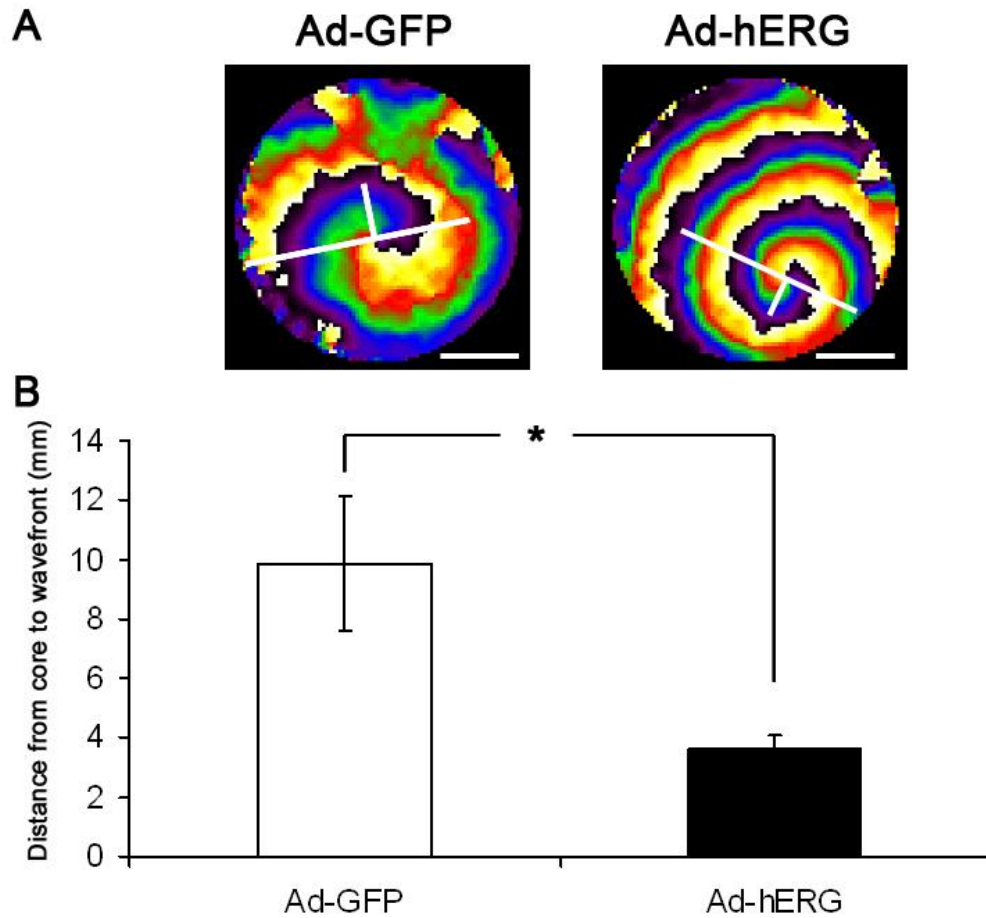
Figure 2.11. Rotor curvature in monolayers infected with Ad-GFP and Ad-hERG. A. Snapshots of the phase movies in Ad-GFP and Ad-hERG infected monolayers. White lines indicated the distance between the tip of rotating spiral wave (Singularity point at center of core) to the wavefront at ½ of the spiral wave full winding (the boundary between blue and purple bands – see text). Scale bar: 10 mm; **B.** quantification of the distance between the core and the wavefront. *: $p < 0.05$. Long white lines: The orientation of the wavefront at the tip. Short white lines: Orientaion perpendicular to the wavefront at the tip; used to measure the tip-to-½ winding distance.
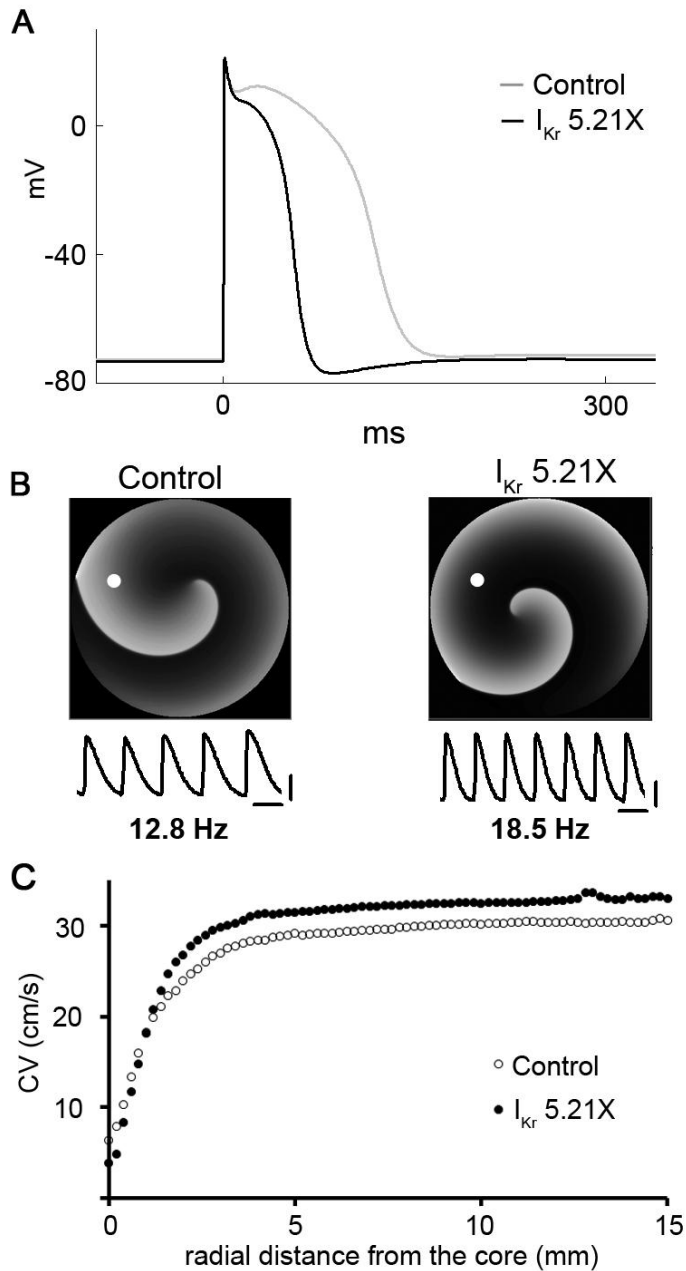
Figure 2.12. Numerical simulation using a neonatal rat ventricular myocyte (NRVM) model. A. Simulated action potentials in control and I_{Kr} 5.21X. Note progressive APD abbreviation and transient hyperpolarization after the action potential in I_{Kr} 5.21X. **B.** Top, snapshots of 2D simulations of reentry in control and I_{Kr} 5.21X in a NRVM model. Reentry frequency is 12.8 Hz in control (left) and 18.5 Hz in I_{Kr} 5.21X (right). Bottom, action potentials calculated at the position of the white dot on each reentry snapshot. Scale bars, horizontal = 50 ms; vertical = 20 mV. **C.** CV as a function of distance from the center of rotation (core).

67
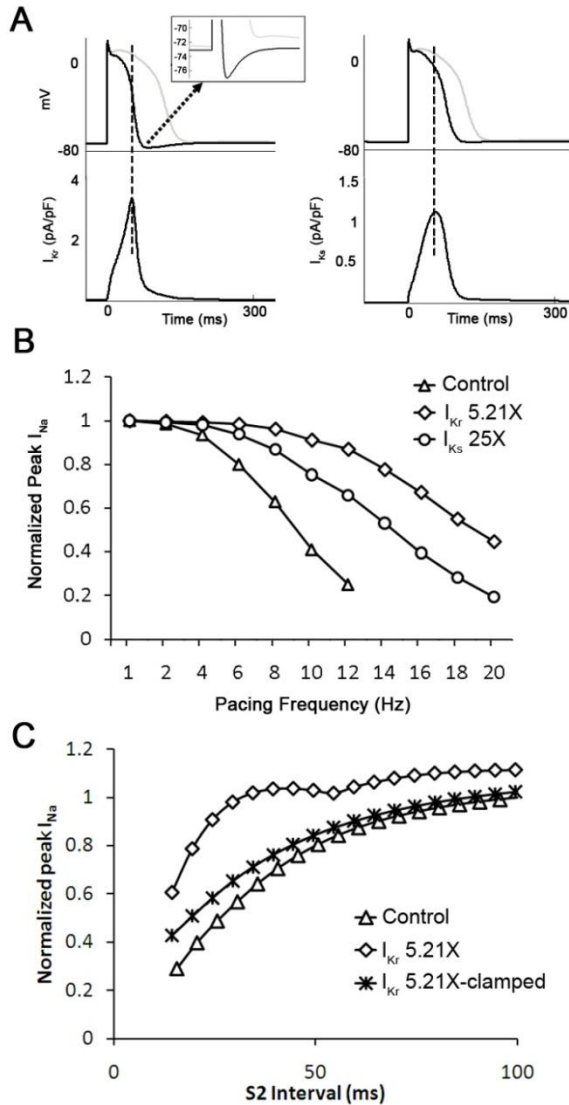
Figure 2.13. Simulations demonstrate different consequences of IKr vs IKs upregulation on membrane potential and INa availability. A. Superimposed single cell action potentials obtained in control (gray traces), I_{Kr} 5.21X (black traces, left) and I_{Ks} 25X (black traces, right). The APD shortening effect of increasing I_{Kr} was greater than I_{Ks}. In addition, transient hyperpolarization occurred only for I_{Kr} upregulation. Inset, expanded voltage versus time trace emphasizes I_{Kr}-induced transient hyperpolarization. **B.** I_{Na} peak density as a function of pacing frequency in control, I_{Kr} 5.21X and I_{Ks} 25X increase. For control and increased I_{Ks}, the magnitude of I_{Na} decreased monotonically with increasing pacing frequency. For I_{Kr} upregulation, I_{Na} increased at pacing frequencies between 10 and 20 Hz indicating increased cell excitability. **C.** A single cell I_{Kr} 5.21X model was paced at 2 Hz for 10 sec (S1) followed by a premature S2 stimulus. At shorter S2 intervals, significantly higher I_{Na} was observed as compared to control. This increased I_{Na} availability was suppressed when the maximal diastolic potential of the cell was clamped to -70 mV.
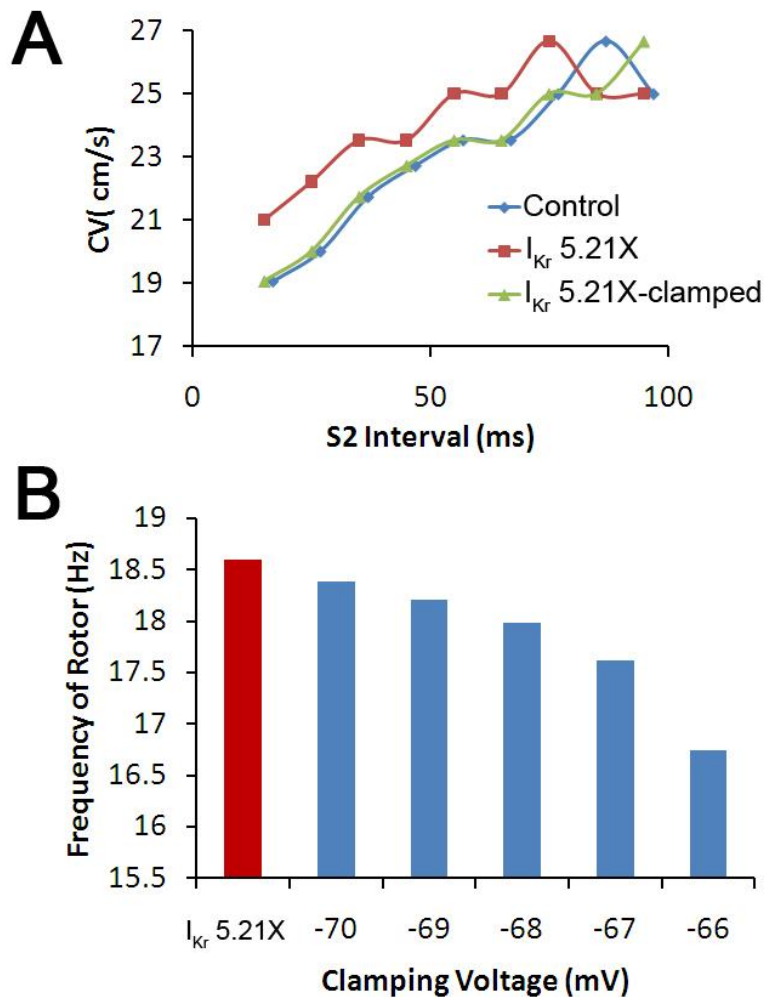
Figure 2.14. Effects of transient hyperpolarization in the IKr 5.21X model. A.
The same S1-S2 protocol as in Fig. 7C was used in a 1D cable of 10 mm length.
The increase in I_{Na} was translated into proportional increase in CV for all S2
intervals. Note that the increase in CV was not observed when the MDP was
clamped to -70 mV. **B.** The frequency of reentry in 2D I_{Kr} 5.21X monolayer model
decreased progressively when the MDP was clamped to more positive voltages,
thus indicating the role of transient hyperpolarization in accelerating reentry.
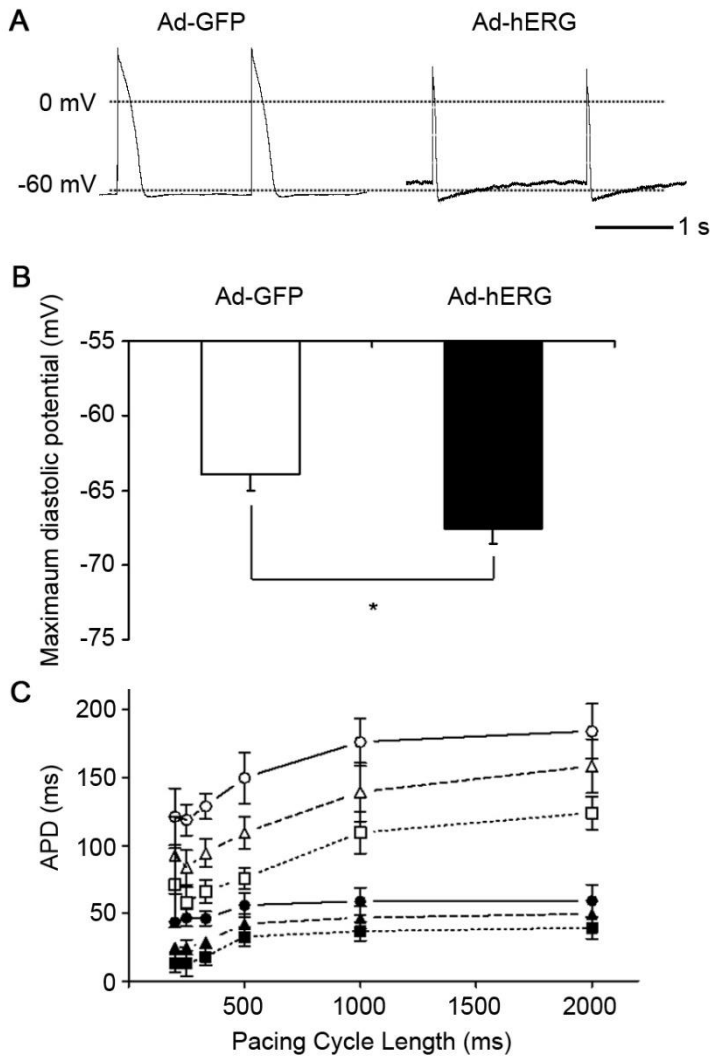
Figure 2.15. IKr overexpression produces transient hyperpolarization after each action potential in isolated NRVM. A. Representative current clamp recordings. Left: action potential in myocyte infected with Ad-GFP; Right: action potential in myocyte infected with Ad-hERG. **B.** Maximal diastolic potential in Ad-hERG and Ad-GFP cells. C. Frequency dependence of APD_{30} (squares), APD_{50} (triangles) and APD_{80} (circles) in myocytes infected with Ad-GFP (filled symbols) or Ad-hERG (open symbols. Student's paired t test.

CHAPTER 3

GENETICALLY ENGINEERED EXCITABLE CARDIAC FIBROBLASTS COUPLED TO CARDIOMYOCYTES RESCUE NORMAL PROPAGATION AND PREVENT ARRHYTHMIAS IN HETEROCELLULAR MONOLAYERS

3.1 Abstract

The use of genetic engineering of unexcitable cells to enable expression of gap junctions and inward rectifier potassium channels has suggested that cell therapies aimed at establishing electrical coupling of unexcitable donor cells to host cardiomyocytes may be arrhythmogenic. Whether similar considerations apply when the donor cells are electrically excitable has not been investigated. Here we tested the hypothesis that adenoviral transfer of genes coding Kir2.1 (I_{K1}), Nav1.5 (I_{Na}) and connexin-43 (Cx43) proteins into neonatal rat ventricular fibroblasts (NRVF) will convert them into excitable cells, rescue rapid conduction velocity (CV) and reduce the incidence of complex reentrant arrhythmias in an *in vitro* model. We used adenoviral (Ad-) constructs encoding Kir2.1, Nav1.5 and Cx43 in NRVF. In single NRVF, Ad-Kir2.1 or Ad-Nav1.5 infection enabled us to regulate the densities of I_{K1} and I_{Na}, respectively. At varying MOI ratios of 10/10,

5/10 and 5/20, NRVF co-infected with Ad-Kir2.1 + Nav1.5 were hyperpolarized and generated action potentials (APs) with upstroke velocities >100 V/s. However, when forming monolayers only the addition of Ad-Cx43 made the excitable NRVF capable of conducting electrical impulses (CV=20.71±0.79 cm/s). When genetically engineered excitable NRVF overexpressing Kir2.1, $Na_V1.5$ and Cx43 were used to replace normal NRVF in heterocellular monolayers that included NRVM, CV was significantly increased (27.59±0.76 vs. 21.18±0.65 cm/s, p<0.05), reaching values similar to those of pure myocytes monolayers (27.27±0.72 cm/s, NS). Moreover, during reentry, propagation was faster and more organized, with a significantly lower number of wavebreaks in heterocellular monolayers formed by excitable compared with unexcitable NRVF. We concluded that viral transfer of genes coding Kir2.1, Nav1.5 and Cx43 to cardiac fibroblasts endows them with the ability to generate and propagate APs. The results provide proof of concept that cell therapies with excitable donor cells increase safety and reduce arrhythmogenic potential.

3.2 Introduction

Cell therapy, which involves the introduction of new cells into host tissue, is emerging as a novel therapeutic approach in heart disease [159]. Numerous studies have shown that by using bioengineered tissue, including stem and somatic cells, there can be successful modification of the electrophysiological properties of host cardiomyocytes [160-162]. Further, antiarrhythmic effects of cell therapy have been observed both *in vitro* and *in vivo* [163]. However, recent

studies suggested that coupling of unexcitable cells, which are commonly used in cell therapy, to cardiomyocytes might yield different functional outcomes that can be arrhythmogenic [164]. Recently, Yankelson et al. showed that when fibroblasts transfected to express the voltage-sensitive potassium channel $K_V1.3$ were co-cultured with NRVM they reduced significantly (to 68%) the spontaneous beating frequency of the cultures [163]. Subsequently, McSpadden et al. demonstrated that coupling cardiomyocytes with human embryonic kidney (HEK293) cells overexpressing connexin-43 (Cx43) modulates pacemaker activity and slows impulse conduction by as much as 5 times [164]. Miragoli et al. found similar slowing in conduction velocity (CV) in cardiomyocytes monolayers covered with fibroblasts expressing Cx43. Accompanying the reduction of conduction was a significant depolarization in host cardiomyocytes' resting potential (RMP) from -78 mV to -50 mV [133]. Our previous studies using co-cultures of randomly distributed NRVM and neonatal rat ventricular fibroblasts (NRVF), which express low levels of Cx43 and repolarizing potassium currents, demonstrated correlations between the proportion of fibroblasts and the amount of conduction and rotor frequency slowing, the number of wavebreaks, and the degree of fibrillatory conduction [85]. The above studies brought attention to the potential arrhythmogenic consequences of using unexcitable cells in an attempt to regenerate normal cardiac function in compromised myocardium. To our knowledge, no one has studied the electrophysiological consequences when the donor cells are engineered to be fully excitable and capable of generating action potentials (APs).

A crucial condition for any approach used in cell therapy in cardiology is the absence of pro-arrhythmia. This can be achieved when the safety of electrical wave propagation between the donor cells and the host myocardium is preserved by both a high level of excitability and an appropriate degree of intercellular communication at the interface. Therefore, it seems reasonable to assume that, using excitable donor cells capable of generating APs as cell therapy would rescue rapid CV and reduce the incidence of complex reentry arrhythmias. To prove this concept we conducted experiments in a heterocellular *in-vitro* model of cardiac impulse propagation. Since NRVF are unexcitable cells lacking sufficient densities of the two essential currents for the generation of ventricular myocyte-like APs (i.e., the inward rectifier current, I_{K1} and the rapid inward sodium current, I_{Na} [132, 165]), we tested the following two hypotheses: 1. adenoviral transfer of genes coding Kir2.1 (I_{K1}) and Nav1.5 (I_{Na}) proteins converts NRVF into excitable cells; 2. adenoviral transfer of genes coding Kir2.1, Nav1.5 and Cx43 proteins into NRVF enables them to couple with host cardiomyocytes, rescue rapid CV and reduce the incidence of complex reentry arrhythmias in an *in vitro* model.

3.3 Materials and Methods

3.3.1 Isolation and Culture of NRVF and NRVM

This study followed guidelines for animal research of the University of Michigan. The protocol was approved by the University Committee on Use and Care of Animals (Approval Number: 09996-2). All surgery was performed after anesthesia by inhalational administration of isofluorane to minimize suffering.

Neonatal rats were euthanized by decapitation. Ventricular myofibroblasts and myocytes were isolated and cultured as described by Zlochiver et al. [85]. Briefly, hearts were removed from 1 to 2 day old Sprague-Dawley rats (Charles River Laboratories, MA) and collected in calcium and magnesium free Hanks' Balanced Salt Solution (HBSS). Ventricles were then isolated, well minced and digested in a solution that contained 0.06% trypsin (Roche Applied Science, IN) and 0.15% pancreatin (Sigma, MO). A two-hour pre-plating period was used to separate early attached NRVF and unattached myocytes. NRVF were cultured in M199 medium (Cambrex, NJ) with 10% fetal bovine serum (FBS) (Cellgro,VA), 20 U/mL penicillin, 20 μg/mL streptomycin; while myocytes were cultured in the same medium with additional 100 μmol/L bromodeoxyuridine (Sigma, MO). Cells were subsequently cultured at 37ºC, 5% CO2. At passage 3 NRVF were plated sparsely for patch clamp experiments, and at high density to form either pure NRVF monolayers (500,000 NRVF/35 mm dish) or heterocellular monolayers (800,000 NRVM or 80%/35 mm dish; 200,000 NRVF or 20% /35 mm dish) for optical mapping experiments. All NRVF used in this study were passage 3 cardiac myofibroblasts, as demonstrated by α-SMA immunostainning.

3.3.2 Adenoviral Constructs

We generated adenoviral constructs containing the human Cx43 cDNA sequence (Ad-Cx43) using the AdMax adenoviral vector creation system (Microbix Biosystems, Mississauga, Ontario, Canada). Human Cx43 cDNA was inserted into the pDC315 shuttle vector. The constructed shuttle vector and adeno-genomic plasmid pBHGloxΔE1,3Cre were co-transfected into Microbix

293 cells using the Ca^{2+}-phosphate transfection method. Viruses were then purified using ViraBind adenovirus purification kit (Cell Biolabs, San Diego, CA) and the titer was calculated by a plaque forming assay before multicellular preparations were infected with varying multiplicity of infection (MOI). Based on immunostaining 10 MOI was found to be optimal for uniform expression of Cx43 proteins. The adenovirus expressing mouse Kir2.1 (Ad-Kir2.1) was generously provided by Dr. Peter Backx (University Health Network Toronto, Ontario, Canada) for amplification at University of Michigan. The Ad-Nav1.5 construct was generously provided by Dr. Silvia Priori (University of Pavia, IRCCS Fondazione Maugeri, Pavia, Italy). 5 and 10 MOI were found optimal for Ad-Kir2.1 infection; 10 and 20 MOI were found optimal for Ad-Nav1.5 infection. Viral infections were performed in NRVF at passage 3. All experiments, including patch clamping, fluorescence recovery after photobleaching (FRAP) and optical mapping, were performed at least 48 hours after infection to allow sufficient protein expression.

3.3.3 Electrophysiology

Voltage clamp experiments were performed in single ventricular NRVF infected with Ad-Kir2.1 or Ad-Nav1.5 using a MultiClamp 700B amplifier (Axon Instruments, Forest City, CA). I_{K1} recordings were carried out as previously described [88]. The bath solution contained (mM): NaCl 148, NaH_2PO_4 0.4, $MgCl_2$ 1, KCl 5.4, $CaCl_2$ 1, HEPES 15, pH was adjusted to 7.4 with NaOH. Nifedipine (5 µM) was added to block calcium currents. The pipette solution contained (mM): KCl 148, $MgCl_2$ 1, EGTA 5, HEPES 5, creatine 2, ATP 5, phosphocreatine 5, pH was adjusted to 7.2 with KOH. The tip potential was

nulled, cell capacitance and series resistance were compensated (~80%) and average cell size was calculated on the basis of cell capacitance (see Figure 3.6). I_{K1} currents were elicited by 125 ms steps applied in 10 mV increments with a holding potential of 0 mV stepping from -100 mV to +50 mV. $BaCl_2$ (1 mM) was used to isolate I_{K1} from background currents. I_{Na} was recorded at room temperature with the pipette filling solution (mM): NaCl 5, CsF 135, EGTA 10, MgATP 5, and HEPES 5 (pH=7.2). The extracellular solution contained (mM): NaCl 5, $MgCl_2$ 1, $CaCl_2$ 1, $CdCl_2$ 0.1, glucose 11, CsCl 132.5, and HEPES 20 (pH=7.35). I_{Na} currents were recorded when membrane potential was depolarized from a holding potential of -160 mV to various potentials from -100 to 10 mV in 5 mV increments and 200 ms duration.

APs were recorded in the current clamp configuration using a MultiClamp 700B amplifier from individual NRVF infected with Ad-Kir2.1 + Ad-Nav1.5, and Ad-Kir2.1 + Ad-Nav1.5 + Ad-Cx43. World Precision Instruments DS8000 stimulator was used to generate square pulses (1 – 3 ms duration). Extracellular solution was HBSS with Ca^{2+} and Mg^{2+} (Sigma, MO). The pipette solution contained (mM): $MgCl_2$ 1, EGTA 5, KCl 150, HEPES 5, Phosphocreatine 5, K_2ATP 4.5, β-Hydroxybutyric acid 2. All AP recordings were conducted at 37°C.

3.3.4 Western Blotting

Uninfected and Ad-Cx34 infected NRVF were lysed with RAPA buffer (50 mM Tris-HCl, pH 7.4, 150 mM NaCl, 1% NP-40, 0.25% Na-deoxycholate, 0.1% SDS, 1 mM EDTA) with protease inhibitor cocktail (Sigma, MO). 20 µg proteins were electrophoresed in 4-20% sodium dodecyl sulfate-polyacrylamide gel under

reducing condition, and proteins were transferred to polyvinylidene difluoride membrane. The membrane was incubated with rabbit anti-hCx43 antibody (Millipore, MA) overnight at 4°C after being incubated in blocking buffer (5% fat-free milk in Tris-buffered saline/Tween 20). After washing three times in TBST (100 mM Tris-HCl, pH 7.4, NaCl 145 mM, 0.1% Tween 20), the membrane was then incubated with horseradish peroxidase-conjugated goat anti-rabbit IgG (Jackson ImmunoResearch, PA). Chemiluminescence was developed by the addition of SuperSignal West Pico Chemiluminescent Substrate (Pierce, IL). Signals were detected using radiographic film. For re-probing, the membrane was incubated in Western Blot Stripping Buffer (Pierce, IL) for 30 min at 37°C. Then the membrane was re-blotted with mouse anti-GAPDH antibody and horseradish peroxidase-conjugated goat anti-mouse IgG (Santa Cruz Biotech, CA).

3.3.5 FRAP experiments

Uninfected and Ad-Cx43 infected (10 MOI) NRVF were loaded with 5-(and-6)-carboxyfluorescein diacetate (5(6)-CFDA) (Invitrogen, NY) (7 μg/mL, 30 min) at 37°C. Regular M199 culture medium was used for the dye loading and during experiments. Dishes were placed in a heating chamber to keep the temperature at 37°C. Singe cells were photobleached selectively using a confocal microscope and laser (Nikon A1R). Snapshots of fluorescence images were taken every 15 seconds until 6 minutes after the photobleaching. Target cells that went through photobleaching were marked with red circles (Figure 3.5). The cells next to the target cell were marked with green circles and used as

positive controls. The blue circles were set in the corner areas where no cells

were present, in order to measure the background florescence. The recovery of

florescence in the target cells was measured and normalized to the florescence

right before the photobleaching. The time course of recovery of 5(6)-CFDA in

target cells was fit with an exponential function using GraphPad Prism 5. The

rate constant [166] and other parameters of the fitting were calculated and

presented in table II.

3.3.6 Optical mapping

Monolayers were placed on a heating stage (37°C) and superfused

constantly with non-carbonated HBSS (Sigma, MO) containing (mM): $CaCl_2$1.6,

KCl 5.4, $MgSO_4$ 0.8, KH_2PO_4 0.4, $NaHCO_3$ 4.2, NaCl136.9, $NaHPO_4$0.3, D-

Glucose5.5, and HEPES10; pH 7.4. A high-resolution CCD camera (80x80 pixels,

SciMeasure Analytical Systems Inc, GA) was used to record electrical wave

propagation after staining the dishes with 40 µM/L di-8-ANEPPS (Molecular

Probes, NY) for 15 minutes. Monolayers were paced at 2X threshold through a

bipolar electrode. Incremental pacing started at 1 Hz (5 ms duration), until loss of

1:1 capture or induction of sustained reentry. 5-s movies were obtained at 200

frames/s and subsequently analyzed offline.

3.3.7 Analyses of Optical Movies

All movies were subjected to background fluorescence subtraction and

filtered using spatial (3x3 pixels) and temporal (7 pixels) conical convolution

filters. Phase maps were generated during sustained reentry to measure rotation

frequency and phase singularities (PS) [76]. Dominant frequency (DF) maps and

phase maps were constructed as described previously [77]. DF and PS were calculated and averaged from each frame. For CV measurements, we conducted ensemble averaging for each pixel for over 5 or more propagating wave fronts following each stimulus. After generating an ensemble averaged movie the activation time distributions (50% of upstroke) for the spatial regions of 5x5 pixels were fitted with the plane, and gradients of activation times gx and gy were calculated for each plane along the x and y axes, respectively. Then we calculated the magnitude of the local CV for each pixel as $(g_x^2 + g_y^2)^{-1/2}$. We then plotted mean values and standard deviations for CV.

3.3.8 Statistical Analyses

Statistical analyses were performed using Origin 6.0 and Prism 5. Two-way ANOVA with Bonferroni post-tests was used for patch clamping and FRAP data. Analyses of rotation frequency and PS were performed using one-way ANOVA with Tukey's multiple comparison test. A Student's *t-test* with Welch-correction was used to analyze the average CV. Data are expressed as mean±SEM. $p < 0.05$ was considered to be significant.

3.4 Results

3.4.1 Kir2.1 and Na$_V$1.5 expression in NRVF

To our knowledge, constitutive expression of Kir2.1 has not been described for NRVF. At 5 MOI and 10 MOI of adenoviral Kir2.1 expression, we consistently observed uniform GFP expression in single NRVF, as illustrated in

Figure 3.1A. I_{K1} densities were determined by voltage-clamp experiments. Figure

3.1B shows the voltage clamp protocol on the top right (see Methods session

3.3.3) and representative Ba^{2+}-sensitive I_{K1} traces on the top left. Cells were

randomly selected for I_{K1} recordings. Both inward and outward I_{K1} increased

when MOI was increased from 5 to 10 MOI. I_{K1} density vs voltage (IV) plots are

shown on the bottom of Figure 3.1B. Both the peak inward and outward currents

were significantly increased in 10 MOI (n=4) Ad-Kir2.1 infected NRVF comparing

to 5 MOI (n=7) infected NRVF (-100 mV: -31.08±7.28 pA/pF vs. -13.83±6.12

pA/pF, p<0.01; -50 mV: 22.22V±5.92 pA/pF vs. 3.34±0.92 pA/pF, p<0.01).

Although the peak inward and outward currents in 5 MOI infected NRVF were still

twice the amount of what reported previously in NRVM [167], we chose this MOI

for the following monolayer experiments in order to keep a homogenous infection

through a dish containing more than 200, 000 NRVF.

Nav1.5 expression was achieved by infecting NRVF with Ad-Nav1.5 at 10

MOI and 20 MOI. Average I_{Na} IV plots are presented in Figure 3.2A, with

representative traces depicted on the top left and voltage-clamp protocol on the

top right. Peak I_{Na} increased significantly when the MOI was increased from 10 to

20 MOI (-21.64±6.64 pA/pF, n=8 vs. -81.27±25.41 pA/pF, n=4, p<0.001),

reaching similar values as I_{Na} in native NRVM [168]. However, as expected

normalized voltage dependence of activation and inactivation and recovery from

inactivation plots showed no difference between the two groups (Figure 3.2B and

C).

3.4.2 Kir2.1 and Na$_V$1.5 functional expression enabled AP generation in single NRVF

As shown in the previous section, NRVF infected with Ad-Kir2.1 plus Ad-Na$_V$1.5 demonstrated robust I$_{Na}$ and I$_{K1}$ currents, which suggested that genetically engineered fibroblasts may become excitable and capable of generating APs. Thus, we co-infected three groups of NRVF with Ad-Kir2.1 and Ad-Nav1.5 (K/Na) at different MOI ratios: 10/10 (n=7), 10/20 (n=8), and 5/20 MOI (n=7), in an effort to optimize the conditions for excitability. The resting membrane potential (RMP) was hyperpolarized in all three K/Na groups with respect to control, as illustrated in Figure 3.3A (p<0.05 vs. UI). In addition, as shown in Figure 3.3B, unlike control cells, current-clamp experiments enabled AP recordings from all three groups of co-infected NRVF. Quantification of the AP maximum upstroke velocity (dV/dtmax) in each of the three groups K/Na groups yielded values of 100 V/s on average. As summarized in Figure 3.3D-F, AP shapes were variable but in all cases repolarization phase showed a characteristic plateau-like morphology, owing to the strong inward rectification of I$_{K1}$ at voltages between -50 and 0 mV (see Figure 3.1B) [169]. However, APD measured at 30, 50 and 80% repolarization were relatively brief in all three groups, with no statistically significant difference among groups.

3.4.3 Cx43 overexpression increased coupling between neighboring NRVF

Previous studies suggested that Cx43 was expressed in cultured cardiac fibroblasts [85]. Thus we used immunohistochemistry in confluent NRVF

82

monolayers to examine the level of Cx43 expression and thus determine whether APs would propagate across the monolayer. As shown by the left panel of Figure 3.4A, Cx43 was nearly undetectable in uninfected NRVF monolayers. As expected, despite the fact that these monolayers expressed robust levels of both Kir2.1 and Nav1.5 they failed to propagate APs. Therefore, we constructed an adenovirus encoding human Cx43 sequence (Ad-Cx43) to overexpress Cx43 proteins. The right panel of Figure 3.4A illustrates the outcome of using the Ad-Cx43 construct. Cx43 was immunolocalized throughout on the cell membrane and also the nucleus area of myofibroblasts after 48 hours infection. Western blot results indicated that there is a more than 30-fold increase in total Cx43 expressions after infection (Figure 3.4B).

We used FRAP as a functional assay to determine whether overexpression of Cx43 increased cell-to-cell communication in the NRVF monolayer. Once loaded, the CFDA dye was retained in the cell because it was hydrolyzed by cytoplasmic esterases into carboxyfluorescein (CF). But it was able to permeate through gap junctions due to its low molecular weight (376 Da) [166]. Therefore, after photobleaching, unbleached dye molecules would redistribute to the target cell through gap junctions. Figure 3.5A shows representative recordings in a control NRVF monolayer v.s. an Ad-Cx43 infected NRVF monolayer, before and after the photobleaching. The target cells for photobleaching were outlined in red in both cases. After 6 minutes, fluorescence barely recovered in uninfected NRVF (n=4), suggesting weak intercellular coupling among normal NRVF. In contrast, Ad-Cx43 infected (n=3) NRVF showed a significant florescence recovery (>60%) after 6 minutes suggesting the

florescent dye was able to travel through the overexpressed Cx43 from the neighboring NRVF. Normalized florescence recovery plots were summarized in Figure 3.5B.

3.4.4 K/Na/Cx43 overexpression enables fast AP propagation in NRVF monolayers

Using 5 MOI Ad-Kir2.1 and 20 MOI Ad-Nav1.5, I_{K1} and I_{Na} current densities in NRVF reached similar levels as the corresponding values in NRVM (see Figures 3.1 and 3.2) [167, 168]. Also this triple infection significantly reduced input membrane resistance (106.85±51.07 MΩ, n=6 vs. 301.95±75.25 MΩ, n=4, p<0.05) without changing the size of these NRVF (70.54±16.37 pF, n=6, vs. 117.74±33.09 pF, n=4, NS) (Figure 3.6). Therefore we chose this ratio in triple infection experiments to determine whether monolayers formed by excitable NRVF overexpressing Cx43 can propagate action potentials at velocities equivalent to those of myocytes. In triple infected NRVF (K/Na/Cx43 at 5/20/10 MOI), we first confirmed that the cells were electrically excitable. Figure 3.7A illustrated representative AP recordings. A K/Na/Cx43 NRVF (Figure 3.7A left) generated large amplitude APs with rapid upstroke velocities, ~ 30 mV overshoot and ~ 40 ms duration similar to the morphology of the K/Na NRVF (Figure 3.3B). On the other hand, in the absence of $Na_V1.5$, K/Cx43 NRVF (Figure 3.7A right) were unable to generate APs despite having a RMP of ~72 mV (Figure 3.7B). Thus the endogenous sodium current [170] was insufficient to depolarize the NRVF even with the stimulus bring the membrane potential to threshold. Figure 3.7B shows that the RMP values for both K/Na/Cx43 (n=6) and K/Cx43 (n=5)

NRVF were similar to each other but significantly more negative than uninfected (n=3) NRVF. Figure 3.7C summarizes the values for APD_{30} APD_{50} and APD_{80} measured at pacing cycle lengths between 250 and 1000 ms. The average APD_{80} at 1 Hz pacing was 37.13±7.78 ms in K/Na/Cx43 NRVF (n=4).

To determine whether the overexpressed I_{K1} rather than the endogenous delayed rectifier potassium currents [170] was responsible for the AP shape during repolarization, we compared the effects of $BaCl_2$ (1 mM) versus 4-AP (1 mM) in single excitable NRVF. As shown in Figure 3.8A, while 4-AP (blue trace) did not affect either the AP shape or the RMP in any significant way, $BaCl_2$ (red trace) initially prolonged APD and subsequently depolarized the RMP of the K/Na cells to the same level as the UI NRVF (gray trace). The effect of $BaCl_2$ was fully reversed after a 5 min washout period (Figure 3.8B, n=4). Figure 3.8C and D summarizes the effect of 4-AP (1 mM, n=5) or $BaCl_2$ (1 mM, n=4) on APD_{30}, APD_{50} and APD_{80}. While 4-AP did not modify APDs on all levels, $BaCl_2$ significantly prolonged both APD_{50} and APD_{80} ($p<0.05$ vs. control).

In high resolution optical mapping experiments, K/Na/Cx43 NRVF plated as 2 dimensional (2D) monolayers, propagated action potentials at velocities (>20 cm/s) that were comparable to those of NRVM monolayers. Figure 3.9A is an activation map generated from an excitable NRVF monolayer paced at 1 Hz. Average CVs were quantified and plotted at varying pacing cycle lengths in Figure 3.9B. The average CV at 1 Hz was 20.71±0.79 cm/s (n=7). The optical APD_{75} and APD_{50} were also measured and summarized in Figure 5C.

85

3.4.5 Engineered excitable NRVF rescue CV in heterocellular monolayers

Previously, we investigated the effects of myocyte-myofibroblast interactions on wave propagation dynamics in monolayers of co-cultured NRVM and NRVF [85]. We demonstrated that CV is diminished with larger myofibroblast/myocyte area ratios. To determine whether NRVF made excitable by K/Na/Cx43 overexpression can serve to rescue propagation, we generated heterocellular monolayers consisting of randomly distributed mixtures of NRVM and excitable NRVF, and compared their properties with those of heterocellular monolayers containing unexcitable (i.e., uninfected) NRVF at the same myofibroblast/myocyte ratio (80% myocytes/20% fibroblasts). Figure 3.10A illustrates the random distribution of the two cell types at two different levels of magnification. In Figure 3.10B, we compare representative uninfected (control) and K/Na/Cx43 monolayers immunostained for α-actinin, Cx43 and DAPI. The expression of Cx43 at myocyte-to-fibroblast contacts was significantly increased in excitable NRVF monolayers comparing to control. Occasionally we were able to detect Cx43 and Cx40 between fibroblasts and myocytes, however, the overall expression of connexins is very limited (Figure 3.1C).

Optical mapping was then performed in three groups of monolayers: pure myocyte (M) monolayers acting as control, heterocellular monolayers containing uninfected fibroblasts and myocytes (UI Fb/M), and heterocellular monolayers containing excitable K/Na/Cx43 fibroblasts and myocytes (K/Na/Cx43 Fb/M) at the same ratio (80% myocytes; 20% fibroblast). Figure 3.11A shows representative activation maps for each of the three groups of monolayers

86

obtained during pacing at 1 Hz. Clearly, conduction in the UI Fb/M monolayer (middle) was very slow compared to control (left). However, when the UI NRVF were replaced by the same number of excitable fibroblasts, the activation time was restored to the control level (right). Composite results from 6-8 monolayers in each group are shown in Figure 3.11B. Quantification of CV at varying pacing cycle lengths demonstrated that the propagation velocities were significantly reduced in the UI Fb/M monolayers compared to control (21.18 ± 0.65, n=6 vs. 27.27 ± 0.72 cm/s, n=8, $p<0.05$); however, excitable NRVF (K/Na/Cx43 Fb/M) fully restored fast CV (27.59 ± 0.76 cm/s, n=8, NS vs M).

3.4.6 Engineered excitable NRVF rescued simple reentry patterns

As demonstrated previously, increasing the proportion of fibroblasts in the monolayer reduced both CV and the frequency of reentry but increased the complexity of propagation during reentry resulting in fractionation, wavebreaks and increased number of wavelets [85]. Here we investigated whether the presence of excitable K/Na/Cx43 fibroblasts prevents such effects and restores the well-organized reentry patterns that are normally observed in monolayers containing >95% myocytes [77, 85]. Thus, we compared the dynamics of reentry in K/Na/Cx43 NRVF/M monolayers with those of UI NRVF/M and pure M monolayers. Sustained functional reentry could be observed in all three groups whether spontaneously or pacing induced. The top of Figure 3.12A shows phase maps obtained during reentry each of the three groups. In these maps, each color indicates one phase of the AP, and the convergence of all colors at the center of rotation is defined as a phase singularity (PS) [151]. Under each phase

map is a corresponding time-space plot (TSP) constructed along the horizontal dashed line [171], to quantify the temporal evolution of the electrical activity in each monolayer. Consistent with our previous findings [85], the spatio-temporal characteristics of reentry were significantly more complex in the UI Fb/M monolayers (center) than in the M monolayer (left) or the K/Na/Cx43 NRVF/M monolayer. Clearly, the number of PS and the complexity of wave propagation were appreciably greater, but the frequency of reentry was significantly lower in the UI NRVF/M monolayer than in the other two. These data are consistent with the CV measurements plotted in Figure 3.12B. Figure 3.12B summarized the rotation frequencies from the three groups of monolayers. Clearly the UI NRVF/M monolayers had slower reentry frequency than control myocyte monolayers (6.81 ± 0.32 Hz, n=10, vs 10.71 ± 0.65 Hz, n=6, $p < 0.05$). However, by increasing both excitability and intercellular conductivity, K/Na/Cx43 overexpression in the Fb/M monolayer restored the rotation frequency (10.35 ± 0.28 Hz, n=11, NS vs M) to control levels. In Figure 8C the maximal number of PS was counted in each frame of a 5-s movie and the average was calculated and then plotted for each group [85]. As expected, the UI NRVF/M monolayers had a larger number of wavebreaks and PSs (6.54 ± 1.16, n=10, vs 1.47 ± 0.23, n=6, $p < 0.05$) underlying increased complexity of AP propagation. Conversely, the number of phase singularities per frame in excitable K/Na/Cx43 Fb/M monolayers was similar to the control monolayer (1.54 ± 0.23, n=11 vs 1.47 ± 0.23, NS).

3.5 Summary

We have used a genetic engineering approach to convert unexcitable cardiac fibroblasts from neonatal rat hearts into excitable cells with the objective of restoring rapid impulse propagation in a heterocellular monolayer model. The most important results in Chapter 3 are as follows: **1.** We generated excitable fibroblasts by adenoviral overexpression of three ion channels: Kir2.1, $Na_V1.5$, and Cx43. **2.** In patch clamp experiments, excitable NRVF demonstrated strong inward rectifier K^+ currents that resulted in well polarized RMP near the predicted K^+ equilibrium potential of -85 mV. These cells were readily excited by electrical stimuli similar to those used in NRVM in patch clamp experiments. When plated as 2D monolayers, these engineered excitable NRVF can propagate APs at velocities similar to those of NRVM. **3.** In heterocellular (NRVM/NRVF) monolayers, engineered excitable NRVF rescued CV to a level similar to pure myocyte monolayers. **4.** During reentry, both the complexity of wave propagation and the number of wavebreaks were significantly less in heterocellular monolayers containing excitable than non-excitable NRVF. Altogether, the data presented strongly suggest that, in the setting of cell therapy, safety of wave propagation and prevention of pro-arrhythmia can only be guaranteed by the ability of both donor cells and host myocardium to generate rapid upstroke action potentials and propagate them at high velocities.

3.6 Study Limitations

The engineered excitable NRVF were generated and examined in an in-vitro neonatal rat model. While this allowed us to overexpress multiple ion channels in a highly controlled environment, the amount of virus required to make excitable NRVF could be different in large animals or humans because of the different expression of ion channels. Also we used uninfected NRVF instead of GFP infected NRVF in the co-culture system. In addition, adult myofibroblasts could be a better resource to further confirm our findings. Moreover, the adenoviral constructs of Kir2.1 used to increase IK1 was from mouse while the other two constructs were from human. While this would be problematic for in vivo testing, our goal was to demonstrate feasibility in an in vitro system. Nevertheless, our data suggested that the excitable NRVF can rescue impulse propagation and reduce the incidence of complex arrhythmias in heterocellular monolayers formed by myocytes and myofibroblasts.

3.7 Conclusion

Genetically modified NRVF are capable of generating and propagating APs similar to those generated by NRVM. Moreover, excitable myofibroblasts can couple with host cardiac myocytes and reduce arrhythmia by restoring rapid conduction and reducing fibrillatory conduction. Altogether, the data presented in this study strongly suggest that, in the setting of cell therapy, safety of wave propagation and prevention of pro-arrhythmia can only be guaranteed by the

ability of both donor cells and host myocardium to generate rapid upstroke action potentials and propagate them at high velocities.

3.8 Acknowledgements

Table I - Cell size of NRVF and NRVM

	Range (pF)	Mean±SEM (pF)
Myofibroblasts	27.83 to 240.6	82.31±8.85 (n=33)
Myocytes	5.85 to 31.12	12.08±0.98 (n=30)

Table II - Exponential fit of FRAP experiment

One-phase association	Control	Ad-Cx43
Best-fit values		
Y0	-52.65	-19.86
Plateau	5.952	54.95
K	4.145	0.9122
Tau	0.2412	1.096
Half-time	0.1672	0.7599
Span	58.60	74.81
Std. Error		
Y0	37.23	2.888
Plateau	0.2479	0.4700
K	1.046	0.04464
Span	37.18	2.702
95% Confidence Intervals		
Y0	-128.9 to 23.61	-25.85 to -13.87
Plateau	5.444 to 6.460	53.98 to 55.93
K	2.003 to 6.288	0.8196 to 1.005
Tau	0.1590 to 0.4993	0.9952 to 1.220
Half-time	0.1102 to 0.3461	0.6898 to 0.8457
Span	-17.55 to 134.7	69.21 to 80.42
Goodness of Fit		
Degrees of Freedom	28	22
R^2	0.7359	0.9901
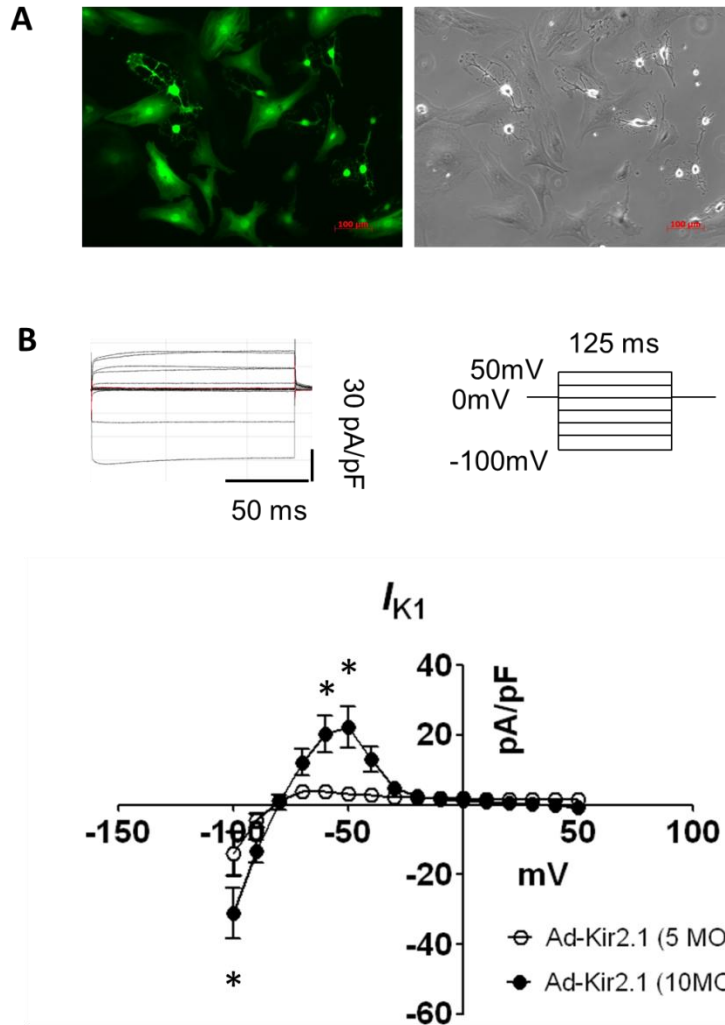
Figure 3.1. Adenoviral expressions of Kir2.1 and NaV1.5 proteins in NRVF after 48 hours of infection. A. GFP-tagged Kir2.1 channel expression. Left: fluorescent micrograph of a passage 3 NRVF 48 h after Ad-Kir2.1 infection. Right: corresponding phase contrast micrograph. Scale bar = 100 µm. **B**. Voltage clamp protocol (top right) and representative example of currents (top left) from Ad-Kir2.1 infected NRVF; and I-V relationship (bottom) of the $BaCl_2$ sensitive currents normalized to cell capacitance in NRVF infected with Ad-Kir2.1 at 5 MOI (open circles) and 10 MOI (filled circles). *: $p < 0.05$
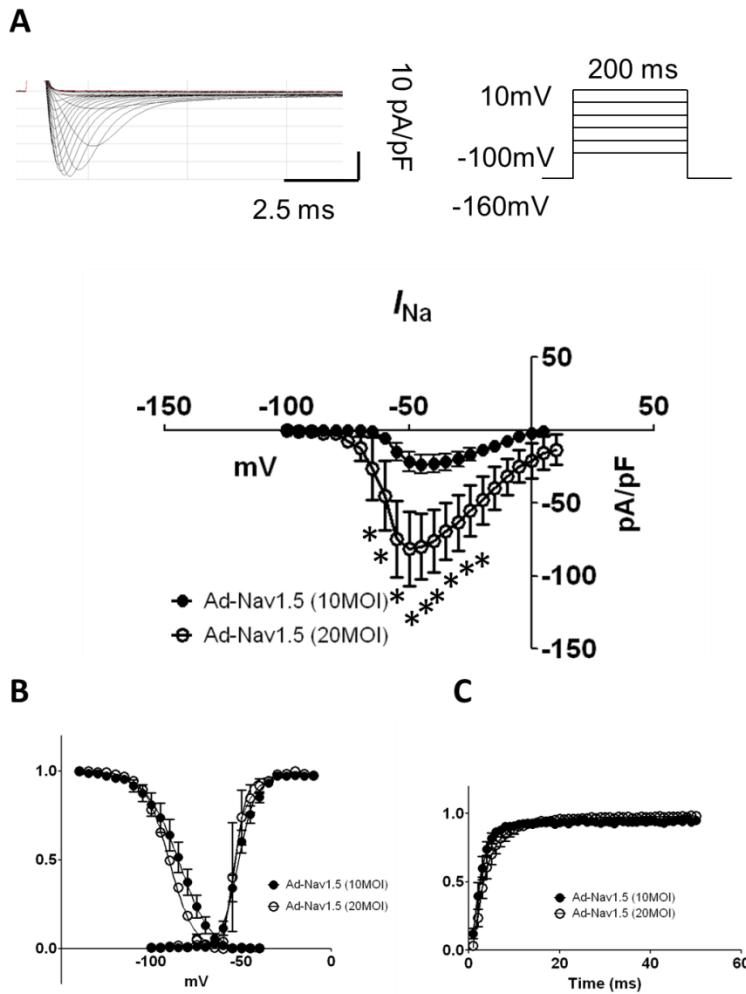
Figure 3.2. Adenoviral expressions of Nav1.5 proteins in NRVF after 48 hours of infection. A. Voltage clamp protocol (top right) and representative examples of currents from Ad-Nav1.5 (top left) infected NRVF; and I-V relationship (bottom) of I_{Na} normalized to cell capacitance in NRVF infected with Ad-Nav1.5 at 10 MOI (filled circles) and 20 MOI (open circles). **B.** Normalized activation and inactivation curves of I_{Na}. **C.** Normalized recovery from inactivation curves of I_{Na}. The curves in B and C are not different statistically. *: $p < 0.05$

95
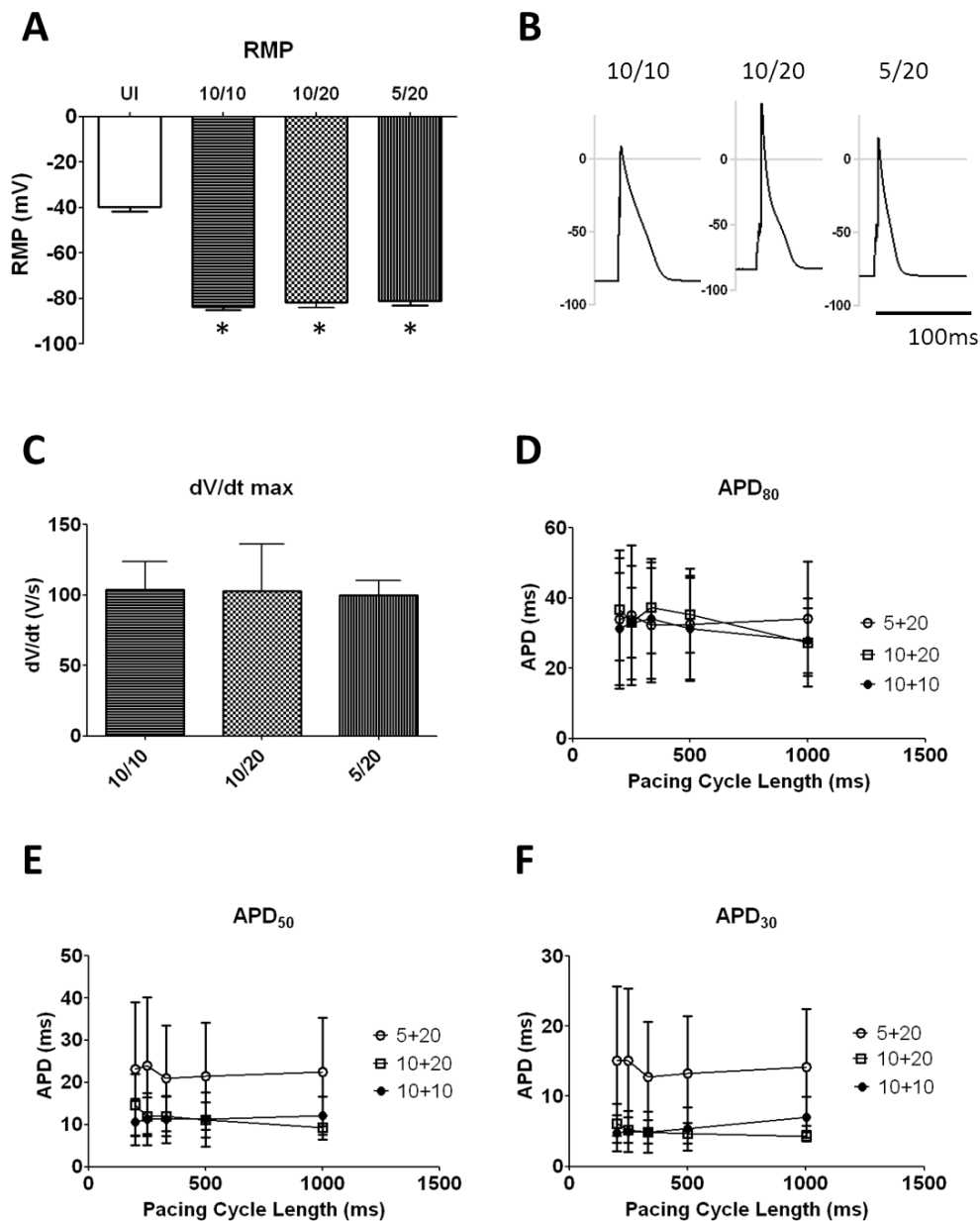
Figure 3.3. Characterizations of action potentials in NRVF co-infected with Ad-Kir2.1 and Ad-Nav1.5 (K/Na). A. Resting membrane potentials from uninfected and co-infected NRVF (K/Na: 10/10, 10/20 and 5/20 MOI). **B.** Representative action potential recordings from NRVF infected with K/Na at 10/10, 10/20 and 5/20 MOI. **C.** Maximal upstroke velocity measured from co-infected NRVF (10/10, 10/20 and 5/20 MOI, NS). **D- F.** Action potential durations (APD)$_{80}$, APD$_{50}$ and APD$_{30}$ in co-infected NRVF (10/10, filled circles; 10/20, open square; and 5/20, open circles; NS).

A

Control Fb   Ad-Cx43 Fb

B

UI   Ad-CX43

Cx43

GAPDH
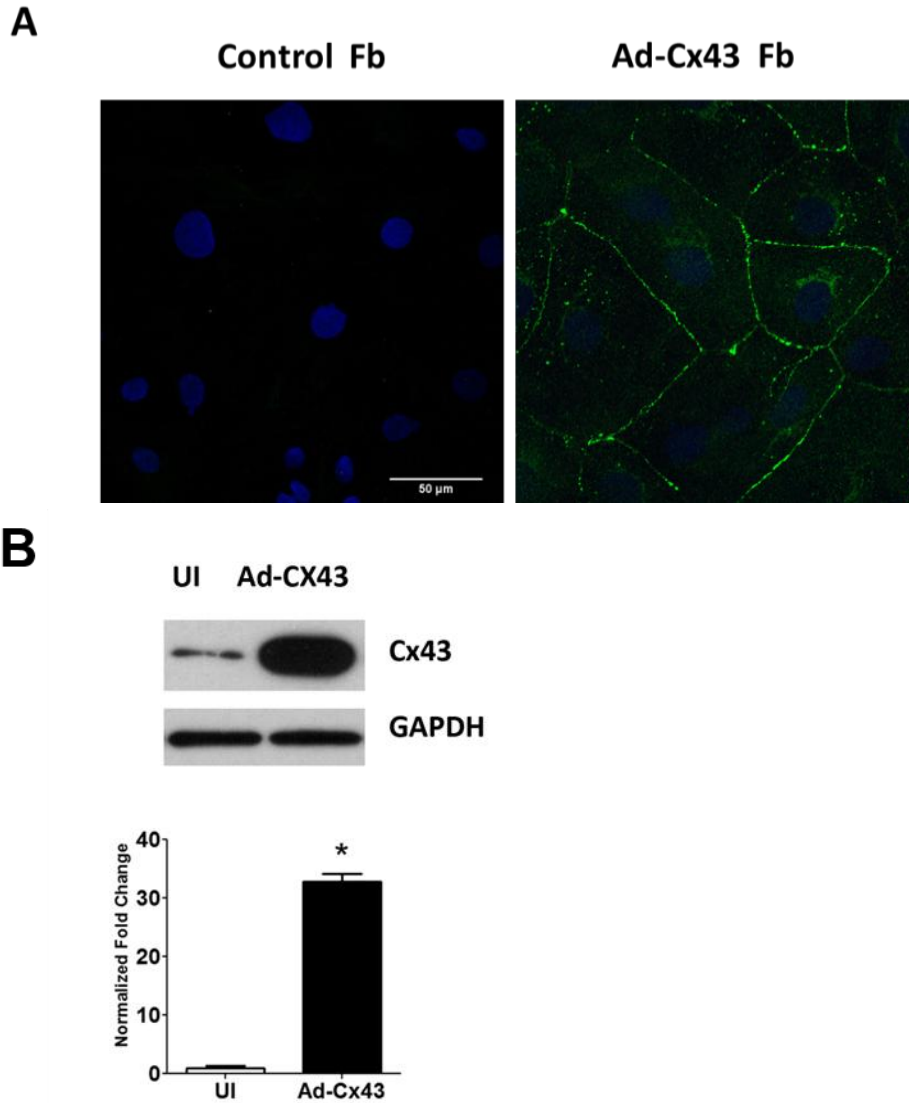
Figure 3.4. Adenoviral expressions of Cx43 in NRVF after 48 hours of infection. A. Immunostainning of control and Ad-Cx43 infected NRVF using an antibody for Cx43 (green) shows increased expression of Cx43 on cell membrane. Scale bar = 50 μm. **B.** Western blot showing Cx43 expression was significantly increased after infection (>30 fold).
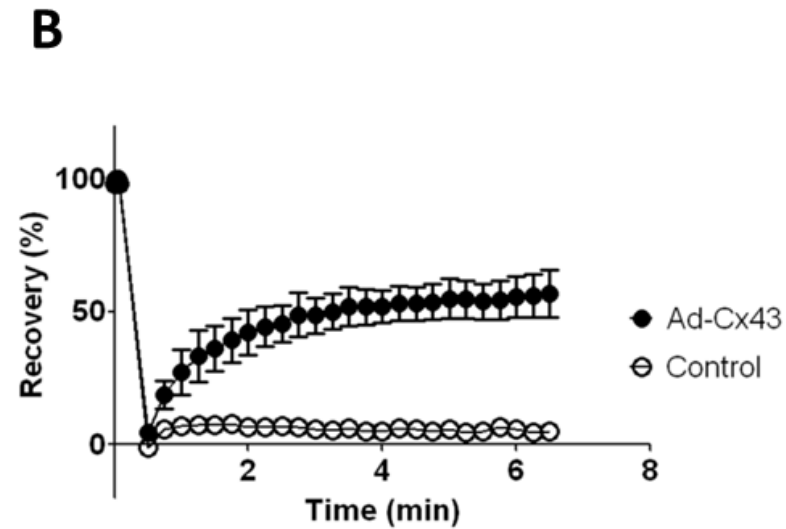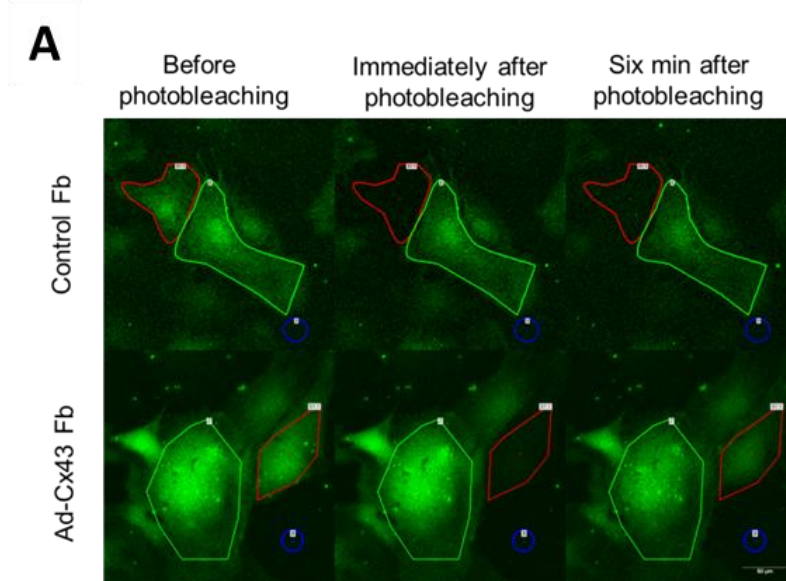
Figure 3.5. Functional coupling in uninfected and Ad-Cx43 infected NRVF.
A. FRAP experiments shows strong functional coupling between Ad-Cx43 infected NRVF. Red box indicated the target cell that was photobleached. Green box shows the possible donor cell next to target cell. Blue and yellow box were used to evaluate the background fluorescence. **B.** Quantification of the florescence recovery six minutes after photobleaching in control (open circles) and Ad-Cx43 infected (filled circles) NRVF.
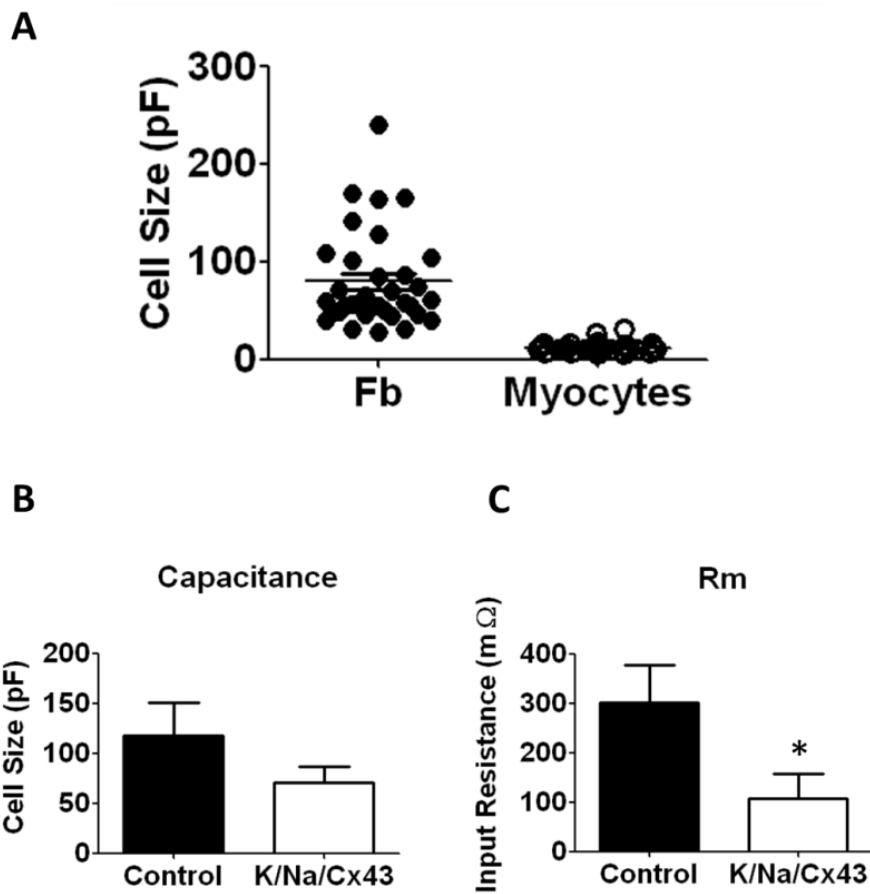
Figure 3.6. Characterizations of cell membrane properties. A. Comparison of cell capacitances between cardiac fibroblasts and NRVM. **B.** The viral infection did not change the capacitances of NRVF. **C.** The viral infection significantly reduced input resistances of NRVF. *: $p < 0.05$.
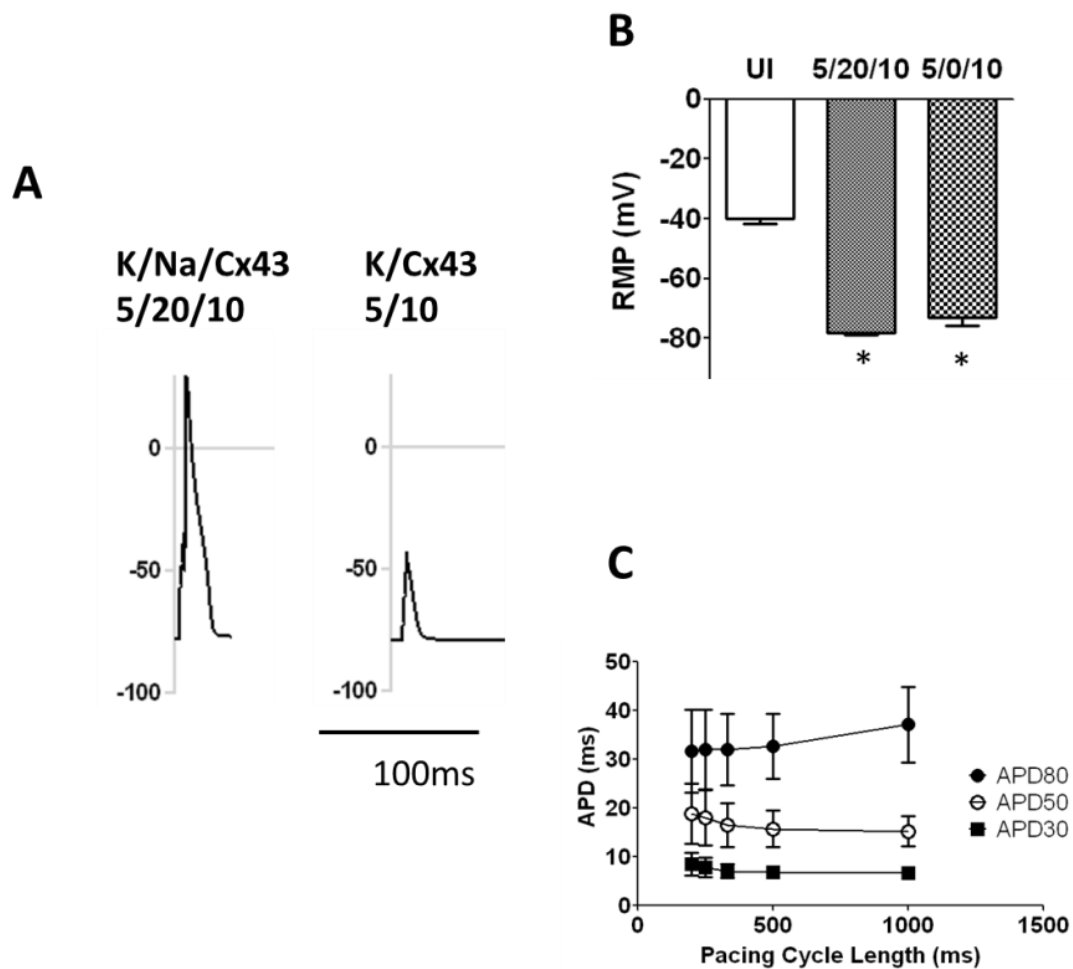
Figure 3.7. Characterizations of action potentials in NRVF infected with Ad-Kir2.1, Ad-Nav1.5 and Ad-Cx43. A. Action potentials were recorded from triple infected (K/Na/Cx43, 5/20/10 MOI) NRVF (left) but not in K/Cx43 (5/10 MOI) infected NRVF (right). **B.** Resting membrane potentials in uninfected, K/Na/Cx43 infected and K/Cx43 infected NRVF. **C.** APD_{80}, APD_{50} and APD_{30} measured at different pacing cycle length.
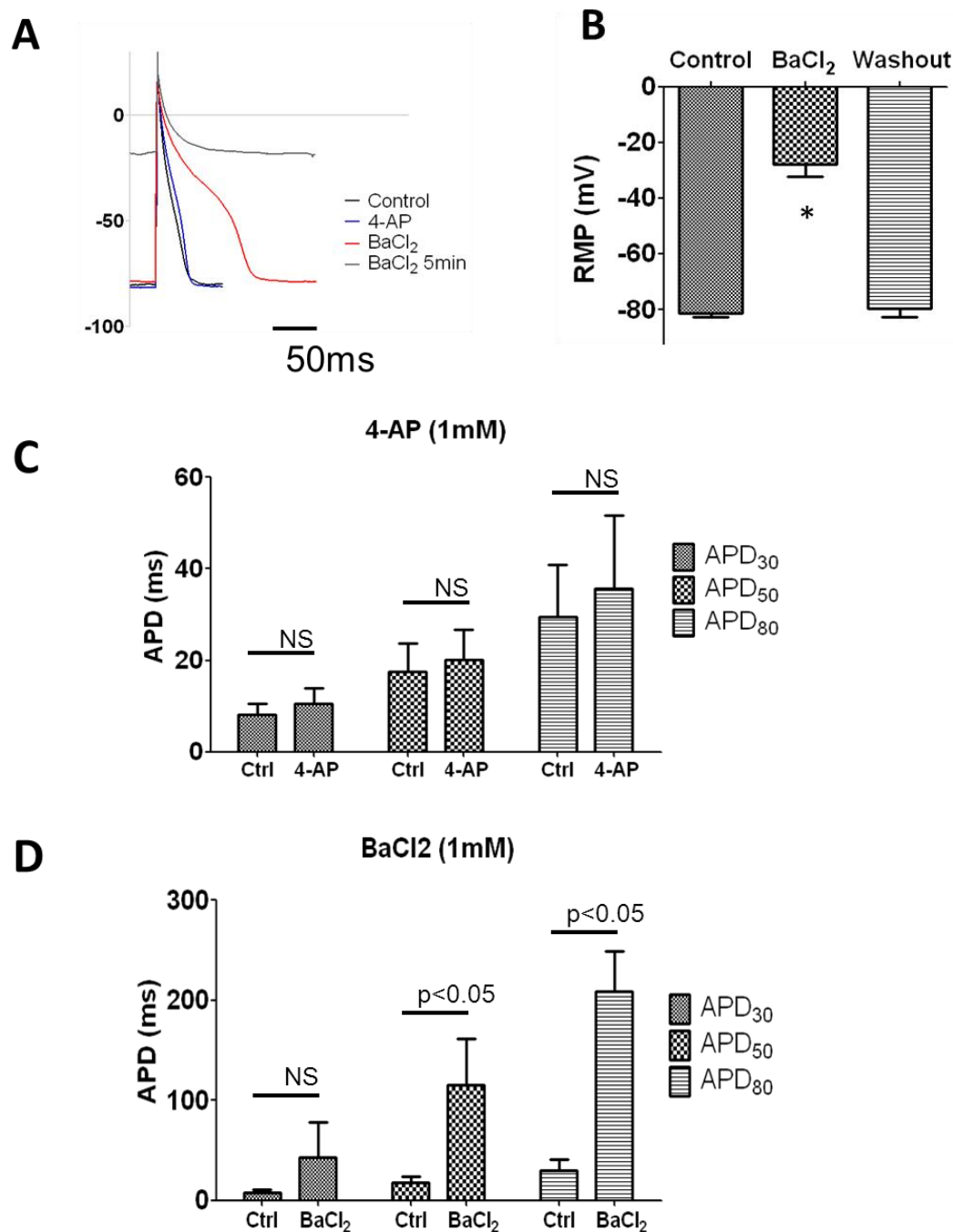
Figure 3.8. Effect of BaCl$_2$ and 4-AP on action potentials in NRVF infected with Ad-Kir2.1, Ad-Nav1.5 and Ad-Cx43. A. Representative AP traces shows that resting membrane potential and APD are sensitive to BaCl$_2$ (1mM) but not 4-AP (1mM). **B.** RMP measured before and after BaCl$_2$ (1mM) perfusion and after washout in K/Na/Cx43 NRVF. *: $p<0.05$. **C.** Quantification of APD$_{30}$, APD$_{50}$ and APD$_{80}$ before and after 4-AP or BaCl$_2$ perfusion. **D**. Quantification APD$_{30}$, APD$_{50}$ and APD$_{80}$ before and after BaCl$_2$ perfusion.
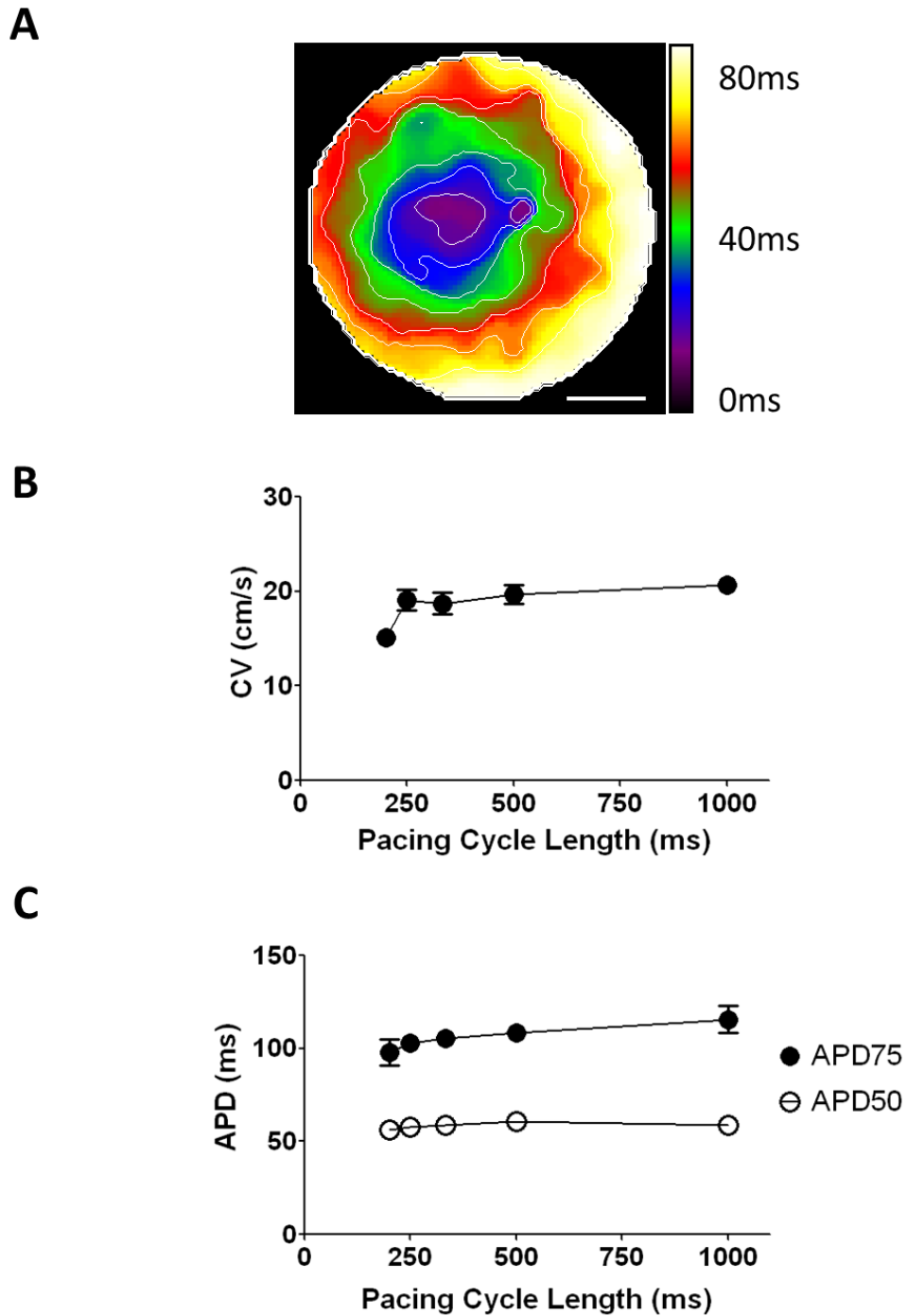
Figure 3.9. Action potential propagation in 2D monolayer of K/Na/Cx43 NRVF. A. Representative activation map of electrical paced (1Hz) AP propagation in K/Na/Cx43 NRVF monolayer. Scale bar =10 mm. B. CV of paced propagation at different pacing cycle lengths from 1000 ms to 200 ms (n=7). **C**. APD_{75} and APD_{50} measured at different pacing cycle lengths from 1000 ms to 200 ms (n=7).
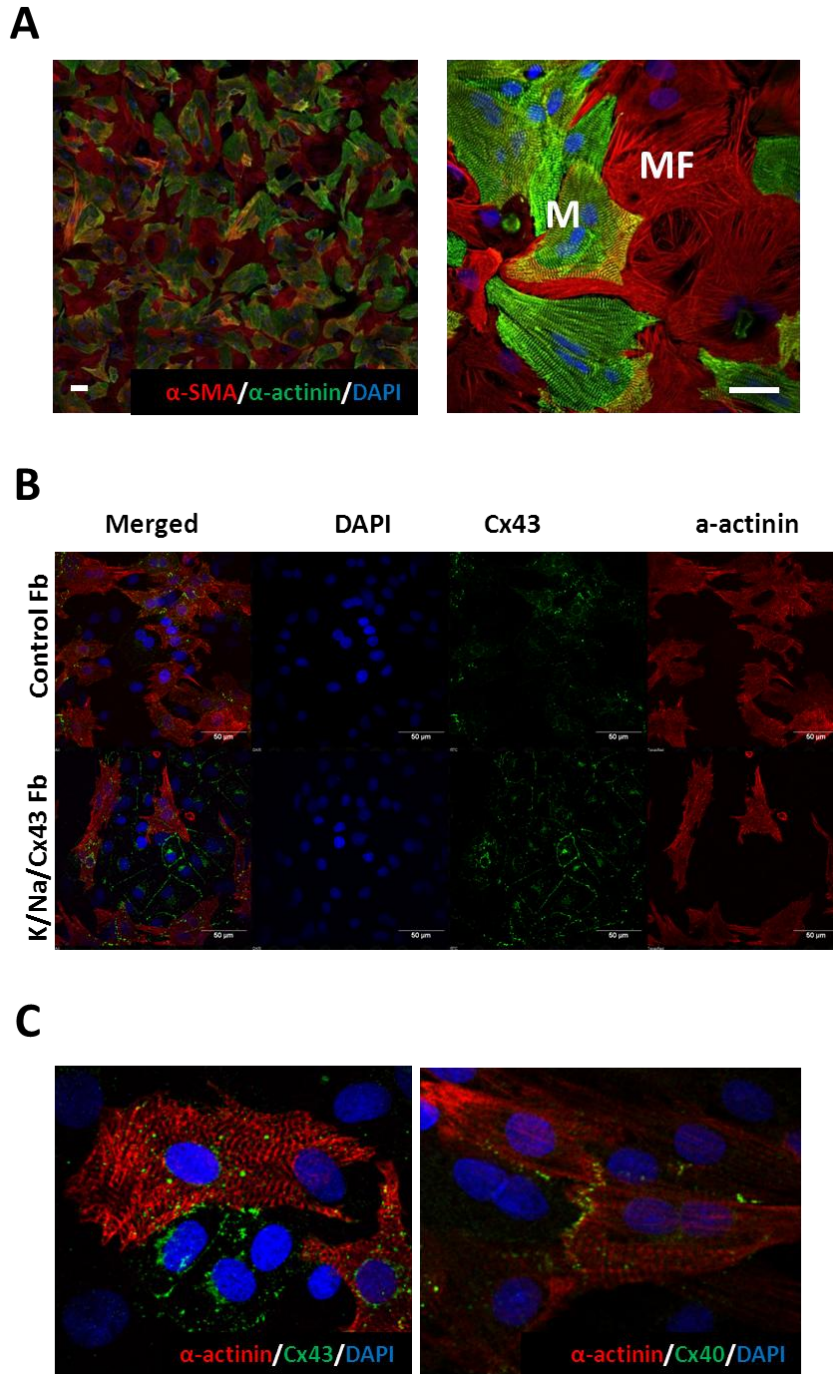
Figure 3.10. Interaction of NRVF and NRVM in an in vitro heterocellular monolayer model. A. Coimmunostainning of NRVM/NRVF co-culture using an antibody for a-SMA (red) and an antibody for a-actinin (green). Scale bar = 10 µm. **B.** Characterization of Cx43 expression between NRVF and NRVM in heterocellular monolayers (uninfected NRVF vs. K/Na/Cx43 NRVF). Scale bar = 50 µm. **C.** Cx43 and Cx40 expression in UI Fb/M heterocellular monolayer. Limited Cx43 and Cx40 were detected between NRVF and NRVM.

A

M   UI Mf/M   KNaCx43 Mf/M

B
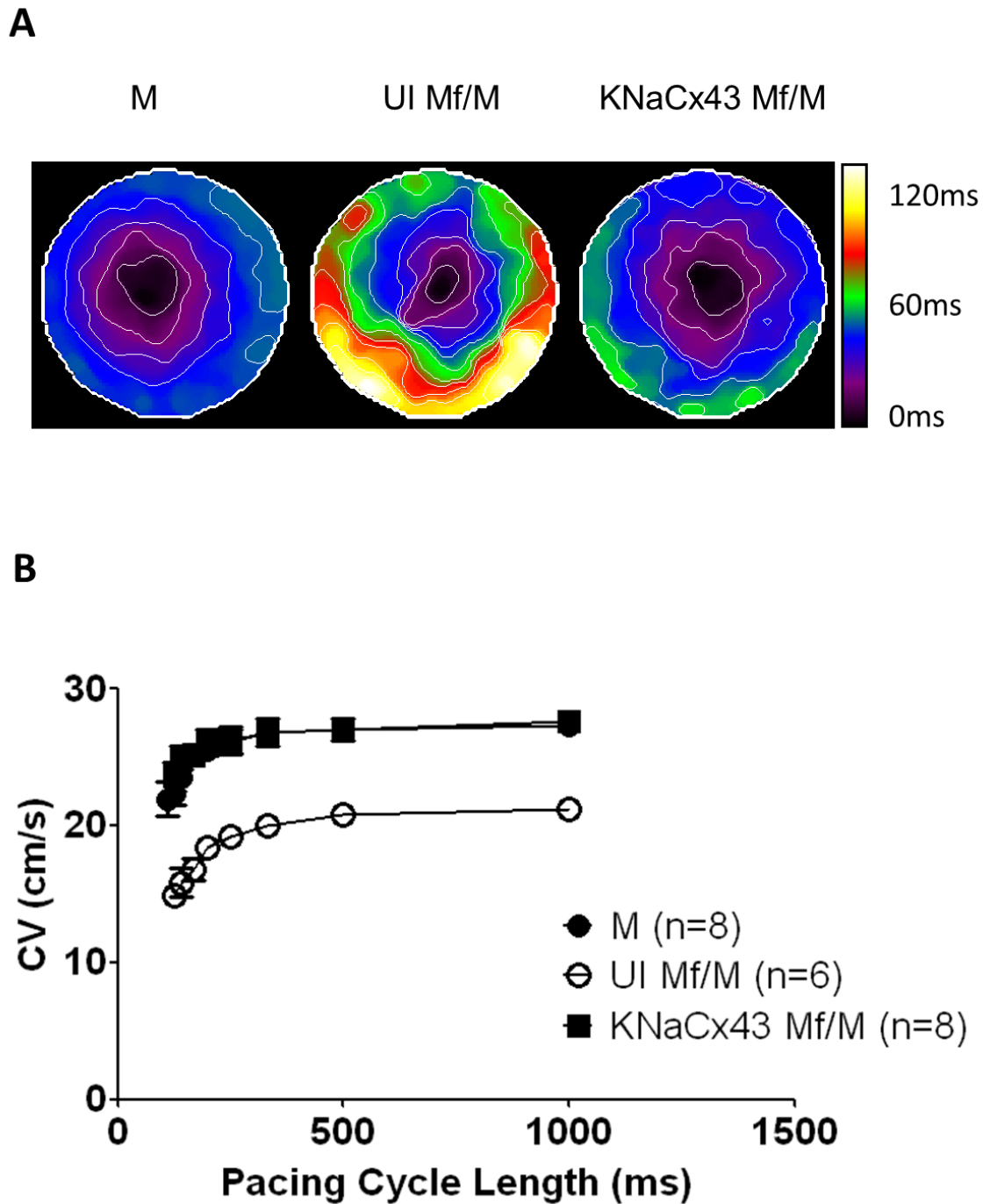
Figure 3.11. K/Na/Cx43 NRVF rescued normal conduction velocity. A. Activation maps from monolayers of myocytes only (M, left), 20% uninfected NRVF/NRVM co-culture (UI Mf/M, middle), and 20% K/Na/Cx43 NRVF/NRVM co-culture (KNaCx43 Mf/M, right). **B.** Quantification of CV at varies pacing cycle lengths in monolayers of myocytes (filled circles), 20% UI co-culture (open circle), and 20% engineered co-culture (filled square).
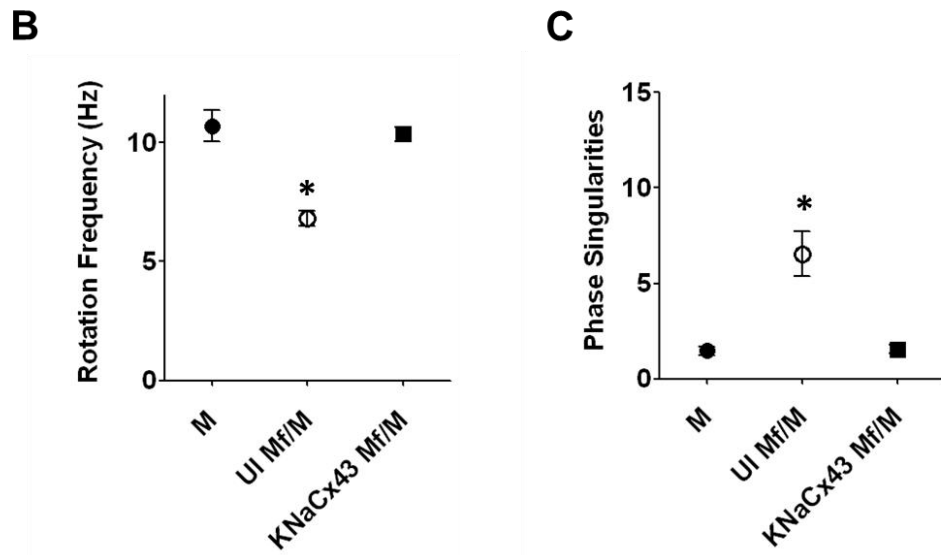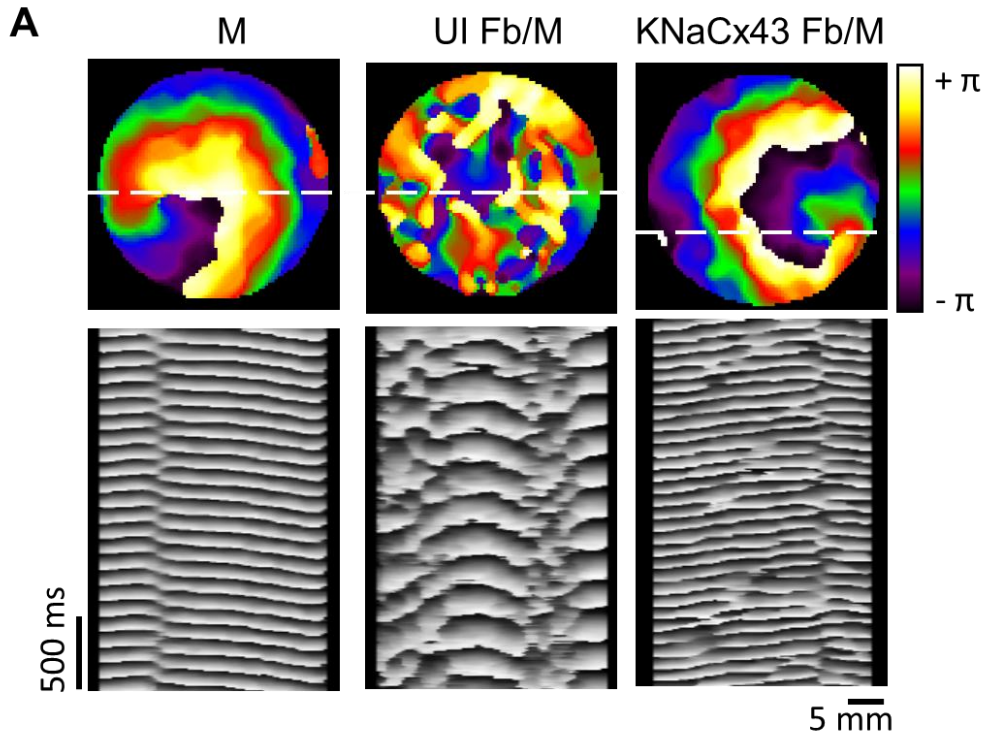
Figure 3.12. K/Na/Cx43 NRVF increased reentry frequency and reduced wavebreaks. A. Snapshots (top) and Time-Space Plot (bottom) from representative optical mapping movies in monolayers of myocytes (left), 20% UI co-culture (middle), and 20% engineered co-culture (right). **B.** Quantification of rotation frequency in monolayers of myocytes (filled circle), UI co-culture (open circle), and engineered co-culture (filled square). **C.** Quantification of phase singularities in monolayers of myocytes (filled circle), UI co-culture (open circle), and engineered co-culture (filled square).

CHAPTER 4

GENERAL DISCUSSION

In general, the work presented in this dissertation can be divided into two similar, and yet, very different projects. One common feature between them is that both projects utilized a 2-dimensional (2D) biological tissue model, each tailored for the specific goals of the given study. First, using NRVM monolayers, I investigated the effects of overexpressing hERG (I_{Kr}) on electrical impulse propagation and reentry dynamics in this cardiac cellular model. Second, I created a new model by engineering cardiac fibroblasts so that they could serve as excitable donor cells. I then studied the efficacy and consequences of using these cells to restore rapid impulse propagation and to reduce the initiation of reentry arrhythmia in monolayers.

The most important results of my first project (hERG/I_{Kr} upregulation) are described in detail in Chapter 2 of this dissertation. In brief, the key electrophysiological findings, with respect to the NRVM monolayer model, are as follows: 1) I_{Kr} overexpression significantly increased the frequency of reentry; 2)

Under conditions of low frequency pacing (1-5Hz), I_{Kr} overexpression shortened the APD by more than 50%, but it did not affect CV; 3) During sustained reentry, APD shortening (induced by I_{Kr} upregulation) resulted in a reduced WL with increased CV values at all distances from the rotor's core. The shorter WL and higher CV provided the appropriate environment for fast and stable rotors; 4) Computer simulations showed that the mechanism underlying I_{Kr}-induced rotor acceleration is a transient hyperpolarization following the repolarization phase of each AP, and this increased sodium channel availability, and thus excitability ahead of the wave front. 5) The transient hyperpolarization was confirmed experimentally in current-clamp studies with single NRVM infected with Ad-HERG. Overall, the results presented in this study (Chapter 2) provide strong evidence that hERG overexpression dramatically accelerates reentry frequency by shortening the APD and transiently hyperpolarizing the cell membrane potential. Therefore, it is plausible to suggest that an increase in I_{Kr} could be an important factor in the maintainance of cardiac arrhythmias.

The most important results of my second project are presented in detail in Chapter 3 of this dissertation. In summary, the key results are as follows: 1) Excitable cardiac fibroblasts were successfully generated by adenoviral overexpression of three ion channel proteins: Kir2.1, $Na_V1.5$, and Cx43. 2) In patch clamp experiments, excitable NRVF demonstrated strong inward rectifier K^+ currents that resulted in a well-polarized RMP near the predicted K^+ equilibrium potential of -85 mV. These cells were readily excited by electrical stimuli similar to those used for NRVM in patch-clamp experiments. When plated

as 2D monolayers, the engineered, excitable NRVF propagated APs at velocities similar to those recorded for NRVM. 3) Compared to monolayers containing unexcitable fibroblasts alone or with NRVM, heterocellular (NRVM/NRVF) monolayers that contained the engineered excitable NRVF were able to rescue the CV to a level similar to that observed with pure myocyte monolayers. 4) During reentry, both the complexity of wave propagation and the number of wavebreaks were significantly less in heterocellular monolayers containing excitable NRVF as compared to those with non-excitable NRVF. Altogether, the results presented in Chapter 3 support the concept that cell therapy would benefit from using electrically excitable donor cells as a way to increase the safety of wave propagation and thereby reduce the arrhythmogenic potential associated with fibrosis and other pathological conditions.

4.1 The Role of hERG in Arrhythmias

To date, more than 300 mutations have been identified that are associated with a loss-of-function phenotype in I_{Kr} and LQTS2 [150]. These mutations result in suppression of hERG channel function, either due to impaired trafficking of the channel subunits or a result of dominant negative effect of the channels on the cell membrane. However, gain-of-function mutations in I_{Kr} can be arrhythmic as well. For example, a hERG-linked short-QT syndrome (SQTS) has been described, in which an inactivation-attenuating mutation, N558K, resulted in a gain-of-function in hERG channels [98, 157]. It is now generally accepted that loss-of-function in hERG channels results in prolongation of the APD, which

increases the incidence of EADs and enhances the spatial heterogeneity of AP

repolarization (a substrate for wavebreaks and reentrant arrhythmia) [172].

However, the mechanism of how a gain-of-function mutation in hERG can lead to

arrhythmias is unclear.

4.1.1 A dual mechanism for I_{Kr}-overexpression-induced rotor acceleration

While the clinical phenotypes associated with alterations in potassium

channels have been characterized for years, it was unknown how those

alterations affected reentry frequency and dynamics. The results presented in

Chapter 2 suggest that the consequences of I_{Kr} overexpression are somewhat

similar to those recently demonstrated for the ventricles of transgenic mice

overexpressing the inward rectifier potassium channel (I_{K1}), which resulted in a

shorter WL, sustained membrane hyperpolarization and exceedingly fast and

stable reentry/VF [76]. In the same study, computer simulations established that

during sustained reentry the diastolic membrane potential was 4 mV more

negative (~−94 mV) in the transgenic when compared to the WT case (~−90 mV).

Such hyperpolarization was enough to increase the Na^+ channel availability by

~30%, which contributed to reducing the core size and stabilizing the reentry.

Similar to the I_{K1} overexpressing mouse, our I_{Kr} overexpressing monolayers also

resulted in APD and WL shortening. However, unlike the transgenic I_{K1}

overexpressing mouse, the hyperpolarization associated with I_{Kr} overexpression

was transient and the membrane potential returned to the resting level within 100

msec or less. Therefore, a relative increase in CV was manifested during high

frequency reentry, but was undetectable at the lower pacing frequencies.

Nevertheless, as demonstrated by additional computer simulations presented in Figure 2.13, increase in Na^+ channel availability at the time of maximal hyperpolarization would certainly contribute to increase the CV (Figure 2.14), and therefore the frequency and stability of the rotors, and to reduce the incidence of wavebreak and fibrillatory conduction. Initially, this result was unexpected because up-regulation of the other component of the delayed rectifier K^+ current, I_{Ks}, has been shown to contribute to post-repolarization refractoriness, and to increase the incidence of wavebreaks and fibrillatory conduction with only a modest increase in rotor frequency [77]. Yet, as demonstrated in the computer simulation (Figure 2.13), while I_{Kr} upregulation produced a transient hyperpolarization after the abbreviated action potential, I_{Ks} upregulation did not result in membrane hyperpolarization and therefore its effects on I_{Na} availability were substantially blunted at any given activation frequency. The difference is most significant at the highest frequencies which are relevant to those usually observed during reentry in the monolayers. Our additional computer simulations presented in Figure 2.14 with MDPs clamped to less negative potentials in single cell, 1D cable and 2D monolayer models further confirm that the transient hyperpolarization contributes to the acceleration of reentry in I_{Kr} upregulation. Note that the effects of increased I_{Na} availability and CV disappeared when the transient hyperpolarization was artificially suppressed.

4.1.2 Different I_{Kr} vs I_{Ks} kinetics, different consequences during reentry

Although initially counterintuitive, the results presented in Chapter 2 add up when one considers the different kinetics of I_{Kr} and I_{Ks}, as well as their

different contributions to repolarization during the cardiac AP. I_{Kr} activates rapidly

and displays marked inward rectification due to the fact that, at positive

membrane potentials, the rate of I_{Kr} inactivation is faster than the rate of I_{Kr}

activation. Consequently, I_{Kr} has a relatively low conductance during the AP

plateau (phase 2) but continues to increase throughout a substantial portion of

the repolarization phase (Figure 2.13A), which explains the marked APD

shortening and transient hyperpolarizing effects of I_{Kr} overexpression in our

NRVM. In contrast, although I_{Ks} increases somewhat more rapidly during the

plateau, it begins to decline before phase-3 repolarization takes place (Figure

2.13B). As such, I_{Ks} contributes relatively less than I_{Kr} to the repolarization phase

of the ventricular AP; and thus, its APD shortening effect is relatively less than I_{Kr}

at any given level of up-regulation. Taken together with the fact that I_{Ks} up-

regulation does not lead to transient hyperpolarization after each AP, this helps

to explain the substantially lesser effect of I_{Ks} up-regulation on rotor frequency in

the monolayers as compared with I_{Kr} up-regulation. As demonstrated previously,

because of its slow deactivation kinetics, I_{Ks} tends to accumulate at high

frequencies, and it therefore plays an important role in post-repolarization

refractoriness and fibrillatory conduction [77, 173, 174]. In contrast, during reentry,

the shorter APD produced by I_{Kr}-overexpression gives Na^+ channels enough time

to recover, without impinging on the excitability during the diastolic interval before

the next wavefront invades the tissue. As a result, this prevents wave front-wave

tail interactions that could destabilize the rotor. In addition, the transient

hyperpolarization induced by I_{Kr} up-regulation further increases Na^+ channel

availability and excitability, both of which are very sensitive to the membrane potential. Finally, I_{Kr} is not known to accumulate like I_{Ks} does, which suggests that I_{Kr} is unlikely to play any important role in postrepolarization refractoriness. This would also explain why, in the I_{Kr}-overexpressing monolayers, rotors are able to spin at very high frequencies without breaking apart.

While this mechanistic understanding of how potassium currents influence arrhythmogenesis is important, more often ventricular arrhythmias occur after a gross anatomical insult [175]. The result of these insults is the infiltration of the damaged myocardium by fibroblasts and the replacement of viable myocardium with fibrosis. However, gene therapy may allow a pathogenic response to an insult to be a viable therapy one day.

4.2 Genetic modification of cardiac fibroblasts

To date, the only published genetic modifications aimed at converting unexcitable cells into fully excitable cells have been conducted using HEK293 cells. In 2005, Cho et al. attempted to generate pacemaker cells from HEK293 cells by expressing three ion channels: Kir2.1, NaChBac (a Na^+ channel from bacteria), and the human ether-a-go-go (hERG)-related channel. APs were generated in a small number of these cells (5/31) with a low maximum rate of rise of 21.6±8.6 V/s [176]. More recently, in 2011, Kirkton et al. generated a stable line of excitable HEK293 cells by modifying the combination of overexpressed proteins, delivering Kir2.1, Nav1.5, and Cx43 proteins into the cells [86]. In a subsequent study, the same group showed that these excitable HEK293 cells

112

improved both the electrical and mechanical function of a "zig-zag" network of cardiac tissues *in vitro* [177]. However, to our knowledge there is no previously published evidence of similar genetic modifications in unexcitable cells of cardiac origin prior to this dissertation.

4.2.1 Why Kir2.1, Na$_V$1.5 and Cx43 overexpression in NRVF?

Excitable NRVF generated APs whose morphology was reminiscent of APs in mammalian ventricular myocytes. However, in all cases, the APD measured at 80% repolarization was relatively brief. Only early during Ba^{2+} superfusion was the APD$_{80}$ prolonged to about 200 msec, and this immediately preceeded complete Ba^{2+}-induced depolarization (Figure 3.8A). During the first few minutes of Ba^{2+} superfusion, the excitable NRVF were slightly depolarized and demonstrated a prominent plateau, which likely represented the time course of I$_{Na}$ inactivation in the presence of strong inward rectification of I$_{K1}$ [169]. Nevertheless, the question still arises as to whether the endogenous sarcolemma ion channels in the NRVF contributed to the AP morphology that was observed under our experimental conditions. What is known is that three endogenous voltage-gated potassium currents have been identified and characterized in NRVF: I$_{to}$, I$_{Kf}$ and I$_{Ks}$ [170]. The distribution of these potassium channels is very heterogeneous, but the transient outward K$^+$ current (I$_{to}$) is expressed in majority of cells; two different delayed rectifier K$^+$ currents (I$_{Kf}$ and I$_{Ks}$) are expressed in a small percentage of cells. In addition, 4-Aminopyridine (4-AP) was found to strongly block I$_{Kf}$ and I$_{Ks}$ while it had no effect on I$_{to}$. As demonstrated in this dissertation (Chapter 3), 4-AP blockade had negligible effects on the APD of

excitable NRVF, which suggests that neither I_{Kf} nor I_{Ks} was involved in repolarization. It is possible that I_{to} may have at least a minor contribution during the early phase of repolarization, but it is unlikely that this current has any significant role in maintaining the highly polarized resting membrane potential.

Walsh et al. also identified a small tetrodotoxin-sensitive Na^+ current in some cells (NRVF) [170]. However, we observed that in the absence of $Na_V1.5$ overexpression, this small endogenous Na^+ current was unable to depolarize cells beyond threshold for AP initiation despite Kir2.1 overexpression, and a cell RMP that was close to -80 mV (Figure 3.7A). In a separate study, Na^+-Ca^{2+} exchanger mRNA and proteins (NCXI) were identified, which may play a role in restoring the Na^+ gradient in our engineered NRVF [178].

With respect to intercellular communication, studies have suggested that NRVF express gap junction proteins (Cx43, Cx45 and Cx40) across a number of species [133, 140, 179]. However, our immunostainning results indicated that expression of either Cx43 or Cx40 was very limited in control NRVF (Figure 3.4 and 3.10C). Therefore, although Ad-Kir2.1 + Ad-Na_V1.5 infection made NRVF excitable, we were unable to demonstrate AP propagation in monolayers consisting of excitable NRVF that only expressed native connexion proteins at endogenous (low) levels. However, excitable NRVF monolayers which also overexpressed Cx43 exhibited wave propagation at velocities comparable to those of NRVM. Therefore, our results suggest that, in the setting of cell therapy, a sufficient density of gap junctional current would be necessary to enable AP propagation between excitable donor cells and the host myocardium.

Our results significantly extend those of McSpadden et al. [164], who

conducted a study on cell pairs, in which each pair consisted of a NRVM coupled

to an engineered unexcitable HEK293 cell of varying size expressing

Kir2.1+Cx43. They demonstrated that pairing a large unexcitable HEK293 cell

(e.g., ~30 pF) to a NRVM reduced the myocyte RMP and distinctly impaired its

ability to generate action potentials. On the other hand, a smaller HEK293 cell

size and the presence of I_{K1} contributed to the preservation of the NRVM RMP,

as well as the excitability of the myocyte and the normal shape of its action

potential. The myofibroblasts used in the present study (~82 pF at passage 3)

were larger than the HEK cells (~31 pF) used by McSpadden et al.. Additionally,

our myofibroblasts were also significantly larger than the NRVM (~12 pF). Yet,

the presence of $Na_V1.5$ in the myofibroblasts not only helped preserve the ability

of the myocytes to generate action potentials but it did so with a high degree of

safety. This was demonstrated by the significantly larger conduction velocity of

heterocellular monolayers containing excitable myofibroblasts as compared to

monolayers containing unexcitable myofibroblasts. We can thus infer that, in the

setting of cell therapy, the safety of wave propagation and prevention of pro-

arrhythmia can only be guaranteed by the ability of both donor cells and host

myocardium to generate and propagate rapid upstroke APs.

4.2.2 NRVF as a target to treat post MI arrhythmia

Several laboratories have developed a number of *in vitro* models to study

the interaction(s) between NRVF and myocytes as well as their role in modifying

impulse conduction and arrhythmia [133, 134]. Rohr's group significantly

advanced our understanding of the consequences of heterocellular coupling using patterned strands [134]. Gaudesius et al. provided strong evidence that NRVF inserted between strands of NRVM could lead to significant conduction delay, and even conduction block, when the length of the NRVF exceeded 300 μm [134]. Subsequently, using a different heterocellular arrangement in their co-cultures, Miragoli et al proved that the incidence of ectopic activity was in direct relationship with the density of NRVF cultured on top of the myocyte strands [133]. Experimental and computer simulation results from our laboratory demonstrated that in heterocellular monolayers containing fibroblasts distributed at random, the conduction velocity exhibits a complex nonlinear dependence on the degree of electrical coupling [85]. Taken together, all of the above evidence emphasizes the importance of the fibroblast as a potential target to regulate normal and abnormal impulse propagation and arrhythmogenesis in the fibrotic myocardium *in vitro*.

Recently, Rosker et al. tested the ability of three individual drugs to revert the phenotype of myofibroblasts to fibroblasts in cultured conditions [145]. They reported that 24 hour-treatment with an actin-targeting drug abolished the NRVF's arrhythmogenic interaction with cardiomyocytes by increasing the CV in a dose-dependent manner [145]. More recently, Jayawardena et al. demonstrated that fibroblasts can be reprogramed to cardiomyocytes using a combination of only four micro-RNAs *in vitro* and *in vivo* [180]. This finding alone further emphasizes the importance, and feasibility of using NRVF as a therapeutic target to regulate cardiac electrical activity post MI. In this

dissertation, I tested another approach, and genetically modified NRVF using a combination genes coding for three distinct membrane proteins that are essential in the initiation and propagation of cardiac electrical impulses. This gene therapy enabled us to successfully improve conduction and prevent the arrhythmogenic effects of fibrosis in an *in vitro* model.

4.3 Cell Therapy to Treat Arrhythmias

Despite varying success of conventional therapies (pharmacology, ablation, and electronic devices) in the treatment of cardiac arrhythmias, cell therapy has recently become a strong focus of many laboratories. Multiple cell types have been tested and introduced into host tissue with the hope of repairing damaged or compromised cardiac tissues by aiming to improve impulse conduction and contractility of the host myocardium [176].

4.3.1 Gene/Cell therapy for cardiac arrhythmias

Recent studies have shown that human mesenchymal stem cells (hMSCs) overexpressing HCN2 channels can serve as biological pacemakers when they form gap junction-mediated electrotonic coupling with host cardiomyocytes [181]. Injection of these hMSCs into the left ventricular wall successfully induced spontaneous rhythms in a chronic canine model of atrioventricular block [161]. Another recently developed technique utilized polyethylene glycol to induce cell fusion and create heterokaryons of donor and host cells. By using cell fusion, the authors avoided uncontrolled migration of donor cells and the need for high

degree gap junction coupling in order to obtain functional effects. Heterokaryons of host myocytes and HCN1-overexpressing fibroblasts have been shown to generate spontaneous AP oscillations in guinea pig hearts [160]. These *in vivo* heterokaryons were shown to remain stable in the host heart for several months [182, 183]. Human embryonic stem cells (hESCs) have also been efficacious at modulating heart rate. hESCs derived cardiomyocytes can differentiate into embryoid bodies (EBs) that can couple with NRVM and serve as biological pacemakers [184]. However, the *in vivo* effects of these pacemakers are still controversial. Importantly, while most cellular therapies have thus far aimed to modulate pacemaking, very few have been developed toward rescuing impulse propagation across diseased or scar tissue.

4.3.2 Choice of NRVF as a candidate for cell therapy

Being the most abundant cell type in the heart, cardiac fibroblasts, and their differentiation into myofibroblasts, have been a huge topic of post MI arrhythmia research [123]. Myofibroblasts have been identified in mature human infarct scars 17 years post-infarction [185, 186]. These cells contribute to the development of cardiac fibrosis. They accomplish this by consolidating the infarcted tissue and depositing excess ECM components [187]. Although cardiac MF maintain the myocardium structure in the diseased heart [188], they also promote arrhythmias through multiple mechanisms. Fibroblasts release various cytokines that alter the expression of various ion channel proteins in cardiomyocytes [189]. Also, they might modify the electrophysiology of the myocardium by coupling to the surviving myocytes.

A recent study has provided evidence that engrafted fibroblasts can integrate with host cardiomyocytes after transplantation in both small and big mammalian models (rats and pigs) [163]. This has paved the path for the development of a combination gene cell therapy aimed at improving conduction in myocardium with fibroblast infiltration. Therefore, the genetic modification approach developed in Chapter 3 may serve as a foundation for novel therapeutic avenues targeting gene regulation of cardiac fibroblasts. Further, excitable MF may play a key role in future cell therapy where they can be used to replace damaged cardiac cells in infarcted tissues.

4.3.3 Engineered MF vs. stem cell derived cardiac myocytes

Human induced pluripotent stem cell (iPS) derived cardiac myocytes have recently become another main focus of cell therapy, with the long-term hope that they may be introduced into host tissue and restore lost myocytes function following MI. Our laboratory has successfully constructed *in vitro* monolayers of human iPS-derived cardiac myocytes (iPSC-CMs) to study impulse propagation and reentry arrhythmias [82]. Simultaneous voltage and calcium mapping showed that iPSC-CM monolayers propagate APs at CVs that are comparable to those recorded in NRVM monolayers [190]. As a potential therapeutic avenue, these cells hold great promise for two main reasons: (1) the ability of researchers to obtain patient-specific iPSC-CMs; (2) the inherent nature of iPSC-CMs to undergo unlimited cell reproduction. To my knowledge, iPSC-CMs have not yet been successfully used for cardiac regeneration, althrough significant advances have been made toward understanding and characterizing these cells so as to

better facilitate their continued and future role in basic research and medicine. Human iPS-CMs were first reported to have a slow upstroke velocity (8~10 V/s), likely due to their less negative RMP (-63.5 and -57.1 mV) [191, 192]. Injection of stem cells, however, has thus far yielded mixed results in *in vivo* animal studies. Although slight improvements have been observed, only a very small percentage of injected iPSC-CM cells have been shown to survive after implantation [193, 194]. Therefore, though promising, the field of cardiac regeneration is in an infant stage and still requires a great deal of fundamental basic research before it could be translated into clinical practice. One area of needed research includes experiments in which excitable MF, similar to those generated in our own study, are allographicaly implanted in the infarcted hearts of animals. The short and long-term results from such a study would likely provide vital insights into the potential benefits/challenges associated with this type of cell therapy. In theory, the idea is novel and of great potential clinical significance: replace scar tissue with (new) cells, cells that are capable of generating APs and possibly forming connections with surviving border zone myocytes. However, the feasibility, efficacy, and long-term benefits/consequences of this idea still need to be thoroughly tested in practice.

MF also offer benefits that may be unique to those predicted from the use of stem cells. In addition to providing a potential conductive pathway, excitable MF may also aid in the formation of 3D collagenous structures that support cardiomyocyte attachment and alignment. As research in the field of regenerative medicine progresses, it may be found that there is a need, or benefit, to introduce

both excitable MF and iPSC-CMs. In such a way, combined therapy might be of experimental (and ultimately of clinical) interest. By using excitable MF in combination with stem cell derived cardiomyocytes, it may be possible to facilitate the formation of cell patches or sheets, which could be implanted into the fibrotic myocardium in order to help improve propagation and contractility.

4.4 Future Directions

As discussed above and throughout this disseration, my doctoral studies have demonstrated that wild type hERG overexpression results in fast reentry that contributes to the maintenance of high frequency arrhythmia. However, the mechanism(s) to explain how gain-of-function mutations (i.e. N588K) of the hERG channel can modify impulse propagation and the dynamics of reentrant arrhythmia is still not completely understood. In contrast to what is observed with protein (channel) overexpression, the number of hERG channels on the cell membrane does not increase on account of the N588K mutation. Instead, this gain-of-function mutation appears to change the gating properties of hERG, specifically the inactivation process of the channel. It is tempting to speculate that wild type hERG overexpression and hERG gain-of-function mutations may have some similar effects on the morphology of the cardiac AP (e.g. short APD); yet, how N588K hERG channel expression alters impulse propagation and reentry remains unclear, and can only be addressed with further study. The N588K mutation has been reported to have mixed gain- and loss-of function consequences for I_{Kr} [195]. In voltage clamp experiments, Grunnet et al.

observed both an increase in peak current and a reduction in tail current [195].

AP clamp experiments revealed that, unlike wild type hERG channels,

expression of N588K hERG channels generates a bell-shaped current whose

peak conductance occurs early in the plateau phase of the AP. The shift

observed in hERG kinetics on account of the N588K mutation may result in a

profound shortening of the APD. However, an important question arises that is

central to both understanding hERG channel function and my doctoral studies:

does expression of mutant channels that result in hERG/I_{Kr} gain-of-function leads

to a transient hyperpolarization, similar to that observed with overexpression of

wild type hERG channels (Chapter 2)? If so, how does this transient

hyperpolarization contribute to normal and abnormal impulse propagation?

Investigating the aforementioned gain-of-function mutation of hERG channels will

provide valuable information on the specific mechanisms underlying short QT

syndrome (SQTS) related mutations and their role in controlling the dynamics of

arrhythmia. For continued study of N588K hERG channels, an *in vitro* model

such as NRVM monolayers would serve as a beneficial tool, as used and

described in Chapter 2. Human iPSC-CMs monolayers (>15 mm in diameter),

such as those recently developed in our laboratory, would also aid in these

studies and additionally close the gap to clinical application (considering the

human origin of the cells) [190]. Overall, the hiPSC-CM model could serve as a

powerful tool to study a variety of known cardiac mutations in a human *in vitro*

system. With respect to SQTS, one could study the molecular and

electrophysiological effects of mutations in different channel proteins using the

same biological model. For example, the same cell and experimental design could be used to investigate the effects/properties of N588K in KCNH2, as well as of mutations specific for KCNQ1 and KCNJ2 (two other common SQTS-related genes). Finally, *in vivo* animal models of SQTS mutations should be developed in order to better evaluate how these potassium channel mutations influence impulse propagation under physiological and pathophysiological conditions at the 3-dimensional level.

Another important outcome of this thesis work is that the included studies provided a "proof of concept" that inclusion of excitable cells, such as those derived from a fibroblast lineage, may be a promising therapy in the prevention of arrhythmia in post-MI myocardium. The results further suggest that inclusion of these excitable cells is likely to be a more appropriate option than using unexcitable cells as a means of preventing pro-arrhythmia. Although I demonstrated that engineered excitable MF were able to improve conduction and reduce arrhythmia complexity, one should of course use caution before extrapolating these data to human clinical practice. It should be noted that introducing MF, let alone additional MF, into the atria or ventricles may be risky for a number of reasons, including: (1) inherent immunogenic response of injection/inclusion of foreign cells; (2) MF are known to increase extracellular matrix generation; and (3) MF secrete various cytokines that may up- or down-regulate ion channel expression in the host myocardium, all of which may have unique and potentially damaging effects. Therefore, genetic modification of endogenous cardiac MF, without introduction of additional myofibroblasts, would

be a more appropriate therapeutic approach. One way this could be achieved is to inject the specific viral constructs directly into the myocardium that has the MF infiltration. However, before any viral vectors are injected into myocardium (injured or not), a full characterization needs to be conducted so as to assess the safety and effects of expressing these ion channels in NRVF *in vivo.* One can speculate the consequences of transduction of viral vectors into damaged myocardium. These would all be valid concerns that need to be considered; however, I also see and believe in the significant benefits that this technique may offer for future basic and clinical studies. In theory, overexpressing appropriate levels of Kir2.1, $Na_V1.5$, and Cx43 enables once unexcitable cells to functionally express the three genes that are most important in the control of ventricular excitability and cell-to-cell propagation. It would be expected that the newly transfected genes should increase the excitability and conduction properties of the damaged myocytes themselves; and should myofibroblast-myocyte coupling exist *in vivo*, then the transfer of these genes into myofibroblasts might also improve excitability in the injured zone, which would thereby help prevent arrhythmias. As suggested above, viral constructs that specifically target myofibroblasts can be generated as an additional gene therapy approach. It has been suggested that, in combination with the development of novel delivery methods, gene therapy may prove to be an effective strategy to eliminate arrhythmias. Lastly, based on theory and the data presented in this thesis, it is my long-term hope and expectation that the use of transformed fibroblasts, such as fully mature induced-pluripotent stem cell derived cardiomyocytes, will be able

to restore the function lost by injured cardiac myocytes, rescue the impaired

excitability of fibrotic myocardium, and ultimately rescue the rhythmic contraction

of the injured heart.

BIBLIOGRAPHY

1. Keating, M.T. and M.C. Sanguinetti, *Molecular and cellular mechanisms of cardiac arrhythmias.* Cell, 2001. **104**(4): p. 569-80.

2. Widmaier, E.P., et al., *Vander's human physiology : the mechanisms of body function.* 12th ed. 2011, New York: McGraw-Hill.

3. Alpert, M.A., *Sudden cardiac arrest and sudden cardiac death on dialysis: Epidemiology, evaluation, treatment, and prevention.* Hemodial Int, 2011. **15 Suppl 1**: p. S22-9.

4. Cole, C.R., et al., *Heart-rate recovery immediately after exercise as a predictor of mortality.* N Engl J Med, 1999. **341**(18): p. 1351-7.

5. Rienstra, M., et al., *Symptoms and functional status of patients with atrial fibrillation: state of the art and future research opportunities.* Circulation, 2012. **125**(23): p. 2933-43.

6. Brodsky, M., et al., *Arrhythmias documented by 24 hour continuous electrocardiographic monitoring in 50 male medical students without apparent heart disease.* Am J Cardiol, 1977. **39**(3): p. 390-5.

7. Jouven, X., et al., *Long-term outcome in asymptomatic men with exercise-induced premature ventricular depolarizations.* N Engl J Med, 2000. **343**(12): p. 826-33.

8. Gertsch, M., *The ECG Manual.* Atrial Premature Beats. 2009: Springer London.

9. Grace, A.A. and D.M. Roden, *Systems biology and cardiac arrhythmias.* Lancet, 2012. **380**(9852): p. 1498-508.

10. Dreifus, L.S., E.L. Michelson, and E. Kaplinsky, *Bradyarrhythmias: clinical significance and management.* J Am Coll Cardiol, 1983. **1**(1): p. 327-38.

11. Barold, S.S., *Indications for permanent cardiac pacing in first-degree AV block: class I, II, or III?* Pacing Clin Electrophysiol, 1996. **19**(5): p. 747-51.

12. MacKenzie, R., *Second-degree AV block.* J Insur Med, 2004. **36**(4): p. 327-32.

13. Barold, S.S. and D.L. Hayes, *Second-degree atrioventricular block: a reappraisal.* Mayo Clin Proc, 2001. **76**(1): p. 44-57.

14. Dhingra, R.C., et al., *The significance of second degree atrioventricular block and bundle branch block. Observations regarding site and type of block.* Circulation, 1974. **49**(4): p. 638-46.

15. Vos, M.A., et al., *Enhanced susceptibility for acquired torsade de pointes arrhythmias in the dog with chronic, complete AV block is related to cardiac hypertrophy and electrical remodeling.* Circulation, 1998. **98**(11): p. 1125-35.

16. Tans, A.C., K.I. Lie, and D. Durrer, *Clinical setting and prognostic significance of high degree atrioventricular block in acute inferior myocardial infarction: a study of 144 patients.* Am Heart J, 1980. **99**(1): p. 4-8.

17.   Wells, J.L., Jr., et al., *Characterization of atrial flutter. Studies in man after open heart surgery using fixed atrial electrodes.* Circulation, 1979. **60**(3): p. 665-73.

18.   Cosio, F.G., et al., *Radiofrequency catheter ablation for the treatment of human type 1 atrial flutter.* Circulation, 1993. **88**(2): p. 804-5.

19.   Feinberg, W.M., et al., *Prevalence, age distribution, and gender of patients with atrial fibrillation. Analysis and implications.* Arch Intern Med, 1995. **155**(5): p. 469-73.

20.   Benjamin, E.J., et al., *Impact of atrial fibrillation on the risk of death: the Framingham Heart Study.* Circulation, 1998. **98**(10): p. 946-52.

21.   Vikman, S., et al., *Altered complexity and correlation properties of R-R interval dynamics before the spontaneous onset of paroxysmal atrial fibrillation.* Circulation, 1999. **100**(20): p. 2079-84.

22.   Ouyang, F., et al., *Repetitive monomorphic ventricular tachycardia originating from the aortic sinus cusp: electrocardiographic characterization for guiding catheter ablation.* J Am Coll Cardiol, 2002. **39**(3): p. 500-8.

23.   Gray, R.A., et al., *Nonstationary vortexlike reentrant activity as a mechanism of polymorphic ventricular tachycardia in the isolated rabbit heart.* Circulation, 1995. **91**(9): p. 2454-69.

24.   Monahan, B.P., et al., *Torsades de pointes occurring in association with terfenadine use.* JAMA, 1990. **264**(21): p. 2788-90.

25. de Bakker, J.M., et al., *Reentry as a cause of ventricular tachycardia in patients with chronic ischemic heart disease: electrophysiologic and anatomic correlation.* Circulation, 1988. **77**(3): p. 589-606.

26. Klein, L.S., et al., *Radiofrequency catheter ablation of ventricular tachycardia in patients without structural heart disease.* Circulation, 1992. **85**(5): p. 1666-74.

27. Kusumoto, F.M., *Cardiovascular Pathophysiology*. Vol. 27601-1300. 1999, Raleigh, North Carolina: Hayes Barton Press.

28. Zipes, D.P. and H.J. Wellens, *Sudden cardiac death.* Circulation, 1998. **98**(21): p. 2334-51.

29. Arnsdorf, M.F., *Cardiac excitability, the electrophysiologic matrix and electrically induced ventricular arrhythmias: order and reproducibility in seeming electrophysiologic chaos.* J Am Coll Cardiol, 1991. **17**(1): p. 139-42.

30. Jalife J, D.M., Anumonwo J, Berenfeld O, Kalifa J., ed. *Basic Cardiac Electrophysiology for the Clinician*. 2009, A John Wiley & Sons, Ltd., Publication.

31. Barnett, M.W. and P.M. Larkman, *The action potential.* Pract Neurol, 2007. **7**(3): p. 192-7.

32. Sanguinetti, M.C. and N.K. Jurkiewicz, *Two components of cardiac delayed rectifier K+ current. Differential sensitivity to block by class III antiarrhythmic agents.* J Gen Physiol, 1990. **96**(1): p. 195-215.

33. Lopatin, A.N. and C.G. Nichols, *Inward rectifiers in the heart: an update on I(K1).* J Mol Cell Cardiol, 2001. **33**(4): p. 625-38.

34. Lloyd-Jones, D., et al., *Heart disease and stroke statistics--2009 update: a report from the American Heart Association Statistics Committee and Stroke Statistics Subcommittee.* Circulation, 2009. **119**(3): p. 480-6.

35. Jalife, J., *Ventricular fibrillation: mechanisms of initiation and maintenance.* Annu Rev Physiol, 2000. **62**: p. 25-50.

36. Jalife, J., ed. *Cardiac Electrophysiology.* 4th ed. 2004, Saunders: Philadelphia, Pa.

37. Noujaim, S.F., et al., *Universal scaling law of electrical turbulence in the mammalian heart.* Proc Natl Acad Sci U S A, 2007. **104**(52): p. 20985-9.

38. Jalife, J. and S.V. Pandit, *Ionic mechanisms of wavebreak in fibrillation.* Heart Rhythm, 2005. **2**(6): p. 660-3.

39. Qu, Z., J.N. Weiss, and A. Garfinkel, *Cardiac electrical restitution properties and stability of reentrant spiral waves: a simulation study.* Am J Physiol, 1999. **276**(1 Pt 2): p. H269-83.

40. Berenfeld, O. and J. Jalife, *Purkinje-muscle reentry as a mechanism of polymorphic ventricular arrhythmias in a 3-dimensional model of the ventricles.* Circ Res, 1998. **82**(10): p. 1063-77.

41. McWilliam, J.A., *Fibrillar Contraction of the Heart.* J Physiol, 1887. **8**(5): p. 296-310.

42. Mayor, A.G., *Rhythmical pulsation in Scyphomedusae.* 1906, Washington,. 62 p.

43.   Mines, G.R., *On circulating excitations in heart muscles and their possible relation to tachycardia and fibrillation.* Transactions of the Royal Society, 1914. **IV**: p. 43-52.

44.   Lewis, T., Feil, H, Stroud, W, *Observations upon flutter and firbillation ii. Nature of auricular flutter.* Heart, 1920. **7**: p. 191-244.

45.   Lewis, T., Drury, A.N., Iliescu, C.C., *A demonstration of circus movement in clinical flutter of the auricles.* Heart, 1921. **8**: p. 341-55.

46.   Lewis, T., Drury, A.N., Iliescu, C.C., *A demonstration of circus movement in clinical fibrillation of the auricles.* Heart, 1921. **8**: p. 361-9.

47.   Allessie, M.A., F.I. Bonke, and F.J. Schopman, *Circus movement in rabbit atrial muscle as a mechanism of trachycardia.* Circ Res, 1973. **33**(1): p. 54-62.

48.   Allessie, M.A., F.I. Bonke, and F.J. Schopman, *Circus movement in rabbit atrial muscle as a mechanism of tachycardia. II. The role of nonuniform recovery of excitability in the occurrence of unidirectional block, as studied with multiple microelectrodes.* Circ Res, 1976. **39**(2): p. 168-77.

49.   Allessie, M.A., F.I. Bonke, and F.J. Schopman, *Circus movement in rabbit atrial muscle as a mechanism of tachycardia. III. The "leading circle" concept: a new model of circus movement in cardiac tissue without the involvement of an anatomical obstacle.* Circ Res, 1977. **41**(1): p. 9-18.

50.   Moe, G.K. and J. Jalife, *Reentry and ectopic mechanisms in the genesis of arrhythmias.* Arch Inst Cardiol Mex, 1977. **47**(2): p. 206-11.

51.   Madore, B.F. and W.L. Freedman, *Computer simulations of the belousov-zhabotinsky reaction.* Science, 1983. **222**(4624): p. 615-6.

52.   Zhabotinsky, A.M. and A.N. Zaikin, *Autowave processes in a distributed chemical system.* J Theor Biol, 1973. **40**(1): p. 45-61.

53.   Winfree, A.T., *Varieties of spiral wave behavior: An experimentalist's approach to the theory of excitable media.* Chaos, 1991. **1**(3): p. 303-334.

54.   Allison, J.S., et al., *The transmural activation sequence in porcine and canine left ventricle is markedly different during long-duration ventricular fibrillation.* J Cardiovasc Electrophysiol, 2007. **18**(12): p. 1306-12.

55.   Henry, H. and V. Hakim, *Linear stability of scroll waves.* Phys Rev Lett, 2000. **85**(25): p. 5328-31.

56.   Setayeshgar, S. and A.J. Bernoff, *Scroll waves in the presence of slowly varying anisotropy with application to the heart.* Phys Rev Lett, 2002. **88**(2): p. 028101.

57.   Vaidya, D., et al., *Reentry and fibrillation in the mouse heart. A challenge to the critical mass hypothesis.* Circ Res, 1999. **85**(2): p. 174-81.

58.   Samie, F.H., et al., *Rectification of the background potassium current: a determinant of rotor dynamics in ventricular fibrillation.* Circ Res, 2001. **89**(12): p. 1216-23.

59.   Mironov, S., J. Jalife, and E.G. Tolkacheva, *Role of conduction velocity restitution and short-term memory in the development of action potential duration alternans in isolated rabbit hearts.* Circulation, 2008. **118**(1): p. 17-25.

60. Pandit, S.V., et al., *Targeting atrioventricular differences in ion channel properties for terminating acute atrial fibrillation in pigs.* Cardiovasc Res, 2011. **89**(4): p. 843-51.

61. Yamazaki, M., et al., *Mechanisms of stretch-induced atrial fibrillation in the presence and the absence of adrenocholinergic stimulation: interplay between rotors and focal discharges.* Heart Rhythm, 2009. **6**(7): p. 1009-17.

62. Nanthakumar, K., et al., *Optical mapping of Langendorff-perfused human hearts: establishing a model for the study of ventricular fibrillation in humans.* Am J Physiol Heart Circ Physiol, 2007. **293**(1): p. H875-80.

63. Herron, T.J., P. Lee, and J. Jalife, *Optical imaging of voltage and calcium in cardiac cells & tissues.* Circ Res, 2012. **110**(4): p. 609-23.

64. Ideker, R.E. and J.M. Rogers, *Human ventricular fibrillation: wandering wavelets, mother rotors, or both?* Circulation, 2006. **114**(6): p. 530-2.

65. Chattipakorn, N., et al., *Three-dimensional mapping of earliest activation after near-threshold ventricular defibrillation shocks.* J Cardiovasc Electrophysiol, 2003. **14**(1): p. 65-9.

66. Yamazaki, M., et al., *Heterogeneous atrial wall thickness and stretch promote scroll waves anchoring during atrial fibrillation.* Cardiovasc Res, 2012. **94**(1): p. 48-57.

67. Berenfeld, O., et al., *Spatially distributed dominant excitation frequencies reveal hidden organization in atrial fibrillation in the Langendorff-perfused sheep heart.* J Cardiovasc Electrophysiol, 2000. **11**(8): p. 869-79.

68. Adrian, R.H., W.K. Chandler, and A.L. Hodgkin, *Voltage clamp experiments in striated muscle fibres.* J Physiol, 1970. **208**(3): p. 607-44.

69. Joyner, R.W., F. Ramon, and J.W. Morre, *Simulation of action potential propagation in an inhomogeneous sheet of coupled excitable cells.* Circ Res, 1975. **36**(5): p. 654-61.

70. Luo, C.H. and Y. Rudy, *A model of the ventricular cardiac action potential. Depolarization, repolarization, and their interaction.* Circ Res, 1991. **68**(6): p. 1501-26.

71. Starmer, C.F., et al., *Proarrhythmic response to potassium channel blockade. Numerical studies of polymorphic tachyarrhythmias.* Circulation, 1995. **92**(3): p. 595-605.

72. Warren, M., et al., *Blockade of the inward rectifying potassium current terminates ventricular fibrillation in the guinea pig heart.* J Cardiovasc Electrophysiol, 2003. **14**(6): p. 621-31.

73. Mansour, M., et al., *Left-to-right gradient of atrial frequencies during acute atrial fibrillation in the isolated sheep heart.* Circulation, 2001. **103**(21): p. 2631-6.

74. Sarmast, F., et al., *Cholinergic atrial fibrillation: I(K,ACh) gradients determine unequal left/right atrial frequencies and rotor dynamics.* Cardiovasc Res, 2003. **59**(4): p. 863-73.

75. Li, J., M. McLerie, and A.N. Lopatin, *Transgenic upregulation of IK1 in the mouse heart leads to multiple abnormalities of cardiac excitability.* Am J Physiol Heart Circ Physiol, 2004. **287**(6): p. H2790-802.

76. Noujaim, S.F., et al., *Up-regulation of the inward rectifier K+ current (I K1) in the mouse heart accelerates and stabilizes rotors.* J Physiol, 2007. **578**(Pt 1): p. 315-26.

77. Munoz, V., et al., *Adenoviral expression of IKs contributes to wavebreak and fibrillatory conduction in neonatal rat ventricular cardiomyocyte monolayers.* Circ Res, 2007. **101**(5): p. 475-83.

78. Kneller, J., et al., *Mechanisms of atrial fibrillation termination by pure sodium channel blockade in an ionically-realistic mathematical model.* Circ Res, 2005. **96**(5): p. e35-47.

79. Mandapati, R., et al., *Quantification of effects of global ischemia on dynamics of ventricular fibrillation in isolated rabbit heart.* Circulation, 1998. **98**(16): p. 1688-96.

80. *The cardiac arrhythmia suppression trial.* N Engl J Med, 1989. **321**(25): p. 1754-6.

81. Akar, F.G. and G.F. Tomaselli, *Ion channels as novel therapeutic targets in heart failure.* Ann Med, 2005. **37**(1): p. 44-54.

82. Zhang, J., et al., *Extracellular matrix promotes highly efficient cardiac differentiation of human pluripotent stem cells: the matrix sandwich method.* Circ Res, 2012. **111**(9): p. 1125-36.

83. Priebe, L. and D.J. Beuckelmann, *Simulation study of cellular electric properties in heart failure.* Circ Res, 1998. **82**(11): p. 1206-23.

84. Sekar, R.B., et al., *IK1 heterogeneity affects genesis and stability of spiral waves in cardiac myocyte monolayers.* Circ Res, 2009. **104**(3): p. 355-64.

85. Zlochiver, S., et al., *Electrotonic myofibroblast-to-myocyte coupling increases propensity to reentrant arrhythmias in two-dimensional cardiac monolayers.* Biophys J, 2008. **95**(9): p. 4469-80.

86. Kirkton, R.D. and N. Bursac, *Engineering biosynthetic excitable tissues from unexcitable cells for electrophysiological and cell therapy studies.* Nat Commun, 2011. **2**: p. 300.

87. Thompson, S.A., et al., *Engraftment of human embryonic stem cell derived cardiomyocytes improves conduction in an arrhythmogenic in vitro model.* J Mol Cell Cardiol, 2012. **53**(1): p. 15-23.

88. Milstein, M.L., et al., *Dynamic reciprocity of sodium and potassium channel expression in a macromolecular complex controls cardiac excitability and arrhythmia.* Proc Natl Acad Sci U S A, 2012.

89. Curran, M.E., et al., *A molecular basis for cardiac arrhythmia: HERG mutations cause long QT syndrome.* Cell, 1995. **80**(5): p. 795-803.

90. Warmke, J.W. and B. Ganetzky, *A family of potassium channel genes related to eag in Drosophila and mammals.* Proc Natl Acad Sci U S A, 1994. **91**(8): p. 3438-42.

91. Itoh, T., et al., *Genomic organization and mutational analysis of HERG, a gene responsible for familial long QT syndrome.* Hum Genet, 1998. **102**(4): p. 435-9.

92. Sanguinetti, M.C. and M. Tristani-Firouzi, *hERG potassium channels and cardiac arrhythmia.* Nature, 2006. **440**(7083): p. 463-9.

93. Sanguinetti, M.C., et al., *A mechanistic link between an inherited and an acquired cardiac arrhythmia: HERG encodes the IKr potassium channel.* Cell, 1995. **81**(2): p. 299-307.

94. Viskin, S., *Long QT syndromes and torsade de pointes.* Lancet, 1999. **354**(9190): p. 1625-33.

95. Haverkamp, W., et al., *The potential for QT prolongation and proarrhythmia by non-antiarrhythmic drugs: clinical and regulatory implications. Report on a policy conference of the European Society of Cardiology.* Eur Heart J, 2000. **21**(15): p. 1216-31.

96. Vitola, J., J. Vukanovic, and D.M. Roden, *Cisapride-induced torsades de pointes.* J Cardiovasc Electrophysiol, 1998. **9**(10): p. 1109-13.

97. Sanguinetti, M.C. and J.S. Mitcheson, *Predicting drug-hERG channel interactions that cause acquired long QT syndrome.* Trends Pharmacol Sci, 2005. **26**(3): p. 119-24.

98. Brugada, R., et al., *Sudden death associated with short-QT syndrome linked to mutations in HERG.* Circulation, 2004. **109**(1): p. 30-5.

99. Nuss, H.B., E. Marban, and D.C. Johns, *Overexpression of a human potassium channel suppresses cardiac hyperexcitability in rabbit ventricular myocytes.* J Clin Invest, 1999. **103**(6): p. 889-96.

100. Morais Cabral, J.H., et al., *Crystal structure and functional analysis of the HERG potassium channel N terminus: a eukaryotic PAS domain.* Cell, 1998. **95**(5): p. 649-55.

101.   Akhavan, A., R. Atanasiu, and A. Shrier, *Identification of a COOH-terminal segment involved in maturation and stability of human ether-a-go-go-related gene potassium channels.* J Biol Chem, 2003. **278**(41): p. 40105-12.

102.   Cui, J., et al., *Analysis of the cyclic nucleotide binding domain of the HERG potassium channel and interactions with KCNE2.* J Biol Chem, 2001. **276**(20): p. 17244-51.

103.   Trudeau, M.C., et al., *HERG, a human inward rectifier in the voltage-gated potassium channel family.* Science, 1995. **269**(5220): p. 92-5.

104.   Smith, P.L., T. Baukrowitz, and G. Yellen, *The inward rectification mechanism of the HERG cardiac potassium channel.* Nature, 1996. **379**(6568): p. 833-6.

105.   Armstrong, C.M. and B. Hille, *Voltage-gated ion channels and electrical excitability.* Neuron, 1998. **20**(3): p. 371-80.

106.   Schonherr, R. and S.H. Heinemann, *Molecular determinants for activation and inactivation of HERG, a human inward rectifier potassium channel.* J Physiol, 1996. **493 (Pt 3)**: p. 635-42.

107.   Spector, P.S., et al., *Fast inactivation causes rectification of the IKr channel.* J Gen Physiol, 1996. **107**(5): p. 611-9.

108.   Choi, S.B., S. Frontoni, and L. Rossetti, *Mechanism by which calcitonin gene-related peptide antagonizes insulin action in vivo.* Am J Physiol, 1991. **260**(2 Pt 1): p. E321-5.

109. Hoshi, T., W.N. Zagotta, and R.W. Aldrich, *Two types of inactivation in Shaker K+ channels: effects of alterations in the carboxy-terminal region.* Neuron, 1991. **7**(4): p. 547-56.

110. Tempel, B.L., et al., *Sequence of a probable potassium channel component encoded at Shaker locus of Drosophila.* Science, 1987. **237**(4816): p. 770-5.

111. Lopez-Barneo, J., et al., *Effects of external cations and mutations in the pore region on C-type inactivation of Shaker potassium channels.* Receptors Channels, 1993. **1**(1): p. 61-71.

112. Yellen, G., et al., *An engineered cysteine in the external mouth of a K+ channel allows inactivation to be modulated by metal binding.* Biophys J, 1994. **66**(4): p. 1068-75.

113. Wang, S., et al., *A quantitative analysis of the activation and inactivation kinetics of HERG expressed in Xenopus oocytes.* J Physiol, 1997. **502 (Pt 1)**: p. 45-60.

114. Lees-Miller, J.P., et al., *Electrophysiological characterization of an alternatively processed ERG K+ channel in mouse and human hearts.* Circ Res, 1997. **81**(5): p. 719-26.

115. London, B., et al., *Two isoforms of the mouse ether-a-go-go-related gene coassemble to form channels with properties similar to the rapidly activating component of the cardiac delayed rectifier K+ current.* Circ Res, 1997. **81**(5): p. 870-8.

116. Sale, H., et al., *Physiological properties of hERG 1a/1b heteromeric currents and a hERG 1b-specific mutation associated with Long-QT syndrome.* Circ Res, 2008. **103**(7): p. e81-95.

117. Mitcheson, J.S. and J.C. Hancox, *An investigation of the role played by the E-4031-sensitive (rapid delayed rectifier) potassium current in isolated rabbit atrioventricular nodal and ventricular myocytes.* Pflugers Arch, 1999. **438**(6): p. 843-50.

118. Weerapura, M., et al., *A comparison of currents carried by HERG, with and without coexpression of MiRP1, and the native rapid delayed rectifier current. Is MiRP1 the missing link?* J Physiol, 2002. **540**(Pt 1): p. 15-27.

119. Weber, K.T., et al., *Myofibroblast-mediated mechanisms of pathological remodelling of the heart.* Nat Rev Cardiol, 2012.

120. Kapoun, A.M., et al., *B-type natriuretic peptide exerts broad functional opposition to transforming growth factor-beta in primary human cardiac fibroblasts: fibrosis, myofibroblast conversion, proliferation, and inflammation.* Circ Res, 2004. **94**(4): p. 453-61.

121. Rohr, S., *Myofibroblasts in diseased hearts: new players in cardiac arrhythmias?* Heart Rhythm, 2009. **6**(6): p. 848-56.

122. Banerjee, I., et al., *Determination of cell types and numbers during cardiac development in the neonatal and adult rat and mouse.* Am J Physiol Heart Circ Physiol, 2007. **293**(3): p. H1883-91.

123. Baudino, T.A., et al., *Cardiac fibroblasts: friend or foe?* Am J Physiol Heart Circ Physiol, 2006. **291**(3): p. H1015-26.

124. Maisch, B., *Extracellular matrix and cardiac interstitium: restriction is not a restricted phenomenon.* Herz, 1995. **20**(2): p. 75-80.

125. McAnulty, R.J. and G.J. Laurent, *Collagen synthesis and degradation in vivo. Evidence for rapid rates of collagen turnover with extensive degradation of newly synthesized collagen in tissues of the adult rat.* Coll Relat Res, 1987. **7**(2): p. 93-104.

126. Weber, K.T., *The Dead Sea lives! Someone's rockin' my dreamboat.* Cardiovasc Res, 1995. **29**(5): p. 604-10.

127. Swynghedauw, B., *Molecular mechanisms of myocardial remodeling.* Physiol Rev, 1999. **79**(1): p. 215-62.

128. Kohl, P., et al., *Electrical coupling of fibroblasts and myocytes: relevance for cardiac propagation.* Journal of electrocardiology, 2005. **38**(4 Suppl): p. 45-50.

129. Peters, N.S., et al., *Disturbed connexin43 gap junction distribution correlates with the location of reentrant circuits in the epicardial border zone of healing canine infarcts that cause ventricular tachycardia.* Circulation, 1997. **95**(4): p. 988-96.

130. Rook, M.B., et al., *Differences in gap junction channels between cardiac myocytes, fibroblasts, and heterologous pairs.* Am J Physiol, 1992. **263**(5 Pt 1): p. C959-77.

131. Kamkin, A., et al., *Mechanically induced potentials in fibroblasts from human right atrium.* Exp Physiol, 1999. **84**(2): p. 347-56.

132. Kohl, P., et al., *Mechanosensitive fibroblasts in the sino-atrial node region of rat heart: interaction with cardiomyocytes and possible role.* Exp Physiol, 1994. **79**(6): p. 943-56.

133. Miragoli, M., G. Gaudesius, and S. Rohr, *Electrotonic modulation of cardiac impulse conduction by myofibroblasts.* Circ Res, 2006. **98**(6): p. 801-10.

134. Gaudesius, G., et al., *Coupling of cardiac electrical activity over extended distances by fibroblasts of cardiac origin.* Circ Res, 2003. **93**(5): p. 421-8.

135. de Bakker, J.M., et al., *Slow conduction in the infarcted human heart. 'Zigzag' course of activation.* Circulation, 1993. **88**(3): p. 915-26.

136. Bian, W. and L. Tung, *Structure-related initiation of reentry by rapid pacing in monolayers of cardiac cells.* Circ Res, 2006. **98**(4): p. e29-38.

137. Eyden, B., *The myofibroblast: an assessment of controversial issues and a definition useful in diagnosis and research.* Ultrastruct Pathol, 2001. **25**(1): p. 39-50.

138. Gabbiani, G., C. Chaponnier, and I. Huttner, *Cytoplasmic filaments and gap junctions in epithelial cells and myofibroblasts during wound healing.* J Cell Biol, 1978. **76**(3): p. 561-8.

139. Goldsmith, E.C., et al., *Organization of fibroblasts in the heart.* Dev Dyn, 2004. **230**(4): p. 787-94.

140. Camelliti, P., et al., *Spatially and temporally distinct expression of fibroblast connexins after sheep ventricular infarction.* Cardiovasc Res, 2004. **62**(2): p. 415-25.

141. Rohr, S., R. Fluckiger-Labrada, and J.P. Kucera, *Photolithographically defined deposition of attachment factors as a versatile method for patterning the growth of different cell types in culture.* Pflugers Arch, 2003. **446**(1): p. 125-32.

142. MacCannell, K.A., et al., *A mathematical model of electrotonic interactions between ventricular myocytes and fibroblasts.* Biophys J, 2007. **92**(11): p. 4121-32.

143. Banerjee, I., et al., *Dynamic interactions between myocytes, fibroblasts, and extracellular matrix.* Ann N Y Acad Sci, 2006. **1080**: p. 76-84.

144. LaFramboise, W.A., et al., *Cardiac fibroblasts influence cardiomyocyte phenotype in vitro.* Am J Physiol Cell Physiol, 2007. **292**(5): p. C1799-808.

145. Rosker, C., et al., *Abolishing myofibroblast arrhythmogeneicity by pharmacological ablation of alpha-smooth muscle actin containing stress fibers.* Circ Res, 2011. **109**(10): p. 1120-31.

146. Rohr, S., *Arrhythmogenic implications of fibroblast-myocyte interactions.* Circ Arrhythm Electrophysiol, 2012. **5**(2): p. 442-52.

147. Chen, L.X., et al., *Fluorofenidone inhibits transforming growth factor-beta1-induced cardiac myofibroblast differentiation.* Pharmazie, 2012. **67**(5): p. 452-6.

148. Vaquero, M., D. Calvo, and J. Jalife, *Cardiac fibrillation: from ion channels to rotors in the human heart.* Heart Rhythm, 2008. **5**(6): p. 872-9.

149. Hancox, J.C., et al., *The hERG potassium channel and hERG screening for drug-induced torsades de pointes.* Pharmacol Ther, 2008. **119**(2): p. 118-32.

150. Perrin, M.J., et al., *Human ether-a-go-go related gene (hERG) K+ channels: function and dysfunction.* Prog Biophys Mol Biol, 2008. **98**(2-3): p. 137-48.

151. Gray, R.A., A.M. Pertsov, and J. Jalife, *Spatial and temporal organization during cardiac fibrillation.* Nature, 1998. **392**(6671): p. 75-8.

152. Berenfeld, O., et al., *Frequency-dependent breakdown of wave propagation into fibrillatory conduction across the pectinate muscle network in the isolated sheep right atrium.* Circ Res, 2002. **90**(11): p. 1173-80.

153. Korhonen, T., S.L. Hanninen, and P. Tavi, *Model of excitation-contraction coupling of rat neonatal ventricular myocytes.* Biophys J, 2009. **96**(3): p. 1189-209.

154. Delcarpio, J.B., W.C. Claycomb, and R.L. Moses, *Ultrastructural morphometric analysis of cultured neonatal and adult rat ventricular cardiac muscle cells.* Am J Anat, 1989. **186**(4): p. 335-45.

155. Tamaddon, H.S., et al., *High-resolution optical mapping of the right bundle branch in connexin40 knockout mice reveals slow conduction in the specialized conduction system.* Circ Res, 2000. **87**(10): p. 929-36.

156. Couderc, J.P., et al., *T-wave morphology abnormalities in benign, potent, and arrhythmogenic I(kr) inhibition.* Heart Rhythm, 2011. **8**(7): p. 1036-43.

157. Gaita, F., et al., *Short QT Syndrome: a familial cause of sudden death.* Circulation, 2003. **108**(8): p. 965-70.

158. Anantharam, A. and G.W. Abbott, *Does hERG coassemble with a beta subunit? Evidence for roles of MinK and MiRP1.* Novartis Found Symp, 2005. **266**: p. 100-12; discussion 112-7, 155-8.

159. Choudry, F.A. and A. Mathur, *Stem cell therapy in cardiology.* Regen Med, 2011. **6**(6 Suppl): p. 17-23.

160. Cho, H.C., Y. Kashiwakura, and E. Marban, *Creation of a biological pacemaker by cell fusion.* Circ Res, 2007. **100**(8): p. 1112-5.

161. Plotnikov, A.N., et al., *Xenografted adult human mesenchymal stem cells provide a platform for sustained biological pacemaker function in canine heart.* Circulation, 2007. **116**(7): p. 706-13.

162. Feld, Y., et al., *Electrophysiological modulation of cardiomyocytic tissue by transfected fibroblasts expressing potassium channels: a novel strategy to manipulate excitability.* Circulation, 2002. **105**(4): p. 522-9.

163. Yankelson, L., et al., *Cell therapy for modification of the myocardial electrophysiological substrate.* Circulation, 2008. **117**(6): p. 720-31.

164. McSpadden, L.C., H. Nguyen, and N. Bursac, *Size and Ionic Currents of Unexcitable Cells Coupled to Cardiomyocytes Distinctly Modulate Cardiac Action Potential Shape and Pacemaking Activity in Micropatterned Cell Pairs.* Circ Arrhythm Electrophysiol, 2012.

165. Fozzard, H.A. and D.A. Hanck, *Structure and function of voltage-dependent sodium channels: comparison of brain II and cardiac isoforms.* Physiol Rev, 1996. **76**(3): p. 887-926.

166. Abbaci, M., et al., *Gap junctional intercellular communication capacity by gap-FRAP technique: a comparative study.* Biotechnol J, 2007. **2**(1): p. 50-61.

167. He, Y., et al., *Kir2.3 knock-down decreases IK1 current in neonatal rat cardiomyocytes.* FEBS Lett, 2008. **582**(15): p. 2338-42.

168. Auerbach, D.S., et al., *Structural heterogeneity promotes triggered activity, reflection and arrhythmogenesis in cardiomyocyte monolayers.* J Physiol, 2011. **589**(Pt 9): p. 2363-81.

169. Delmar, M., et al., *Ionic basis and analytical solution of the wenckebach phenomenon in guinea pig ventricular myocytes.* Circ Res, 1989. **65**(3): p. 775-88.

170. Walsh, K.B. and J. Zhang, *Neonatal rat cardiac fibroblasts express three types of voltage-gated K+ channels: regulation of a transient outward current by protein kinase C.* Am J Physiol Heart Circ Physiol, 2008. **294**(2): p. H1010-7.

171. Pertsov, A.M., et al., *Spiral waves of excitation underlie reentrant activity in isolated cardiac muscle.* Circ Res, 1993. **72**(3): p. 631-50.

172. Brunner, M., et al., *Mechanisms of cardiac arrhythmias and sudden death in transgenic rabbits with long QT syndrome.* J Clin Invest, 2008. **118**(6): p. 2246-59.

173. Kurokawa, J., H. Abriel, and R.S. Kass, *Molecular basis of the delayed rectifier current I(ks)in heart.* J Mol Cell Cardiol, 2001. **33**(5): p. 873-82.

174. Gintant, G.A., *Two components of delayed rectifier current in canine atrium and ventricle. Does IKs play a role in the reverse rate dependence of class III agents?* Circ Res, 1996. **78**(1): p. 26-37.

175. Weber, K.T., C.G. Brilla, and J.S. Janicki, *Myocardial fibrosis: functional significance and regulatory factors.* Cardiovasc Res, 1993. **27**(3): p. 341-8.

176. Cho, H.C. and E. Marban, *Biological therapies for cardiac arrhythmias: can genes and cells replace drugs and devices?* Circ Res, 2010. **106**(4): p. 674-85.

177. Kirkton, R.D. and N. Bursac, *Genetic engineering of somatic cells to study and improve cardiac function.* Europace, 2012. **14 Suppl 5**: p. v40-v49.

178. Raizman, J.E., et al., *The participation of the Na+-Ca2+ exchanger in primary cardiac myofibroblast migration, contraction, and proliferation.* J Cell Physiol, 2007. **213**(2): p. 540-51.

179. De Maziere, A.M., et al., *Spatial and functional relationship between myocytes and fibroblasts in the rabbit sinoatrial node.* J Mol Cell Cardiol, 1992. **24**(6): p. 567-78.

180. Jayawardena, T.M., et al., *MicroRNA-Mediated In Vitro and In Vivo Direct Reprogramming of Cardiac Fibroblasts to Cardiomyocytes.* Circ Res, 2012. **110**(11): p. 1465-73.

181. Potapova, I., et al., *Human mesenchymal stem cells as a gene delivery system to create cardiac pacemakers.* Circ Res, 2004. **94**(7): p. 952-9.

182. Alvarez-Dolado, M., et al., *Fusion of bone-marrow-derived cells with Purkinje neurons, cardiomyocytes and hepatocytes.* Nature, 2003. **425**(6961): p. 968-73.

183. Weimann, J.M., et al., *Stable reprogrammed heterokaryons form spontaneously in Purkinje neurons after bone marrow transplant.* Nat Cell Biol, 2003. **5**(11): p. 959-66.

184. Xue, T., et al., *Functional integration of electrically active cardiac derivatives from genetically engineered human embryonic stem cells with quiescent recipient ventricular cardiomyocytes: insights into the development of cell-based pacemakers.* Circulation, 2005. **111**(1): p. 11-20.

185. Sun, Y. and K.T. Weber, *Infarct scar: a dynamic tissue.* Cardiovasc Res, 2000. **46**(2): p. 250-6.

186. Willems, I.E., et al., *The alpha-smooth muscle actin-positive cells in healing human myocardial scars.* Am J Pathol, 1994. **145**(4): p. 868-75.

187. Fessing, M.Y., et al., *BMP signaling induces cell-type-specific changes in gene expression programs of human keratinocytes and fibroblasts.* J Invest Dermatol, 2010. **130**(2): p. 398-404.

188. Souders, C.A., S.L. Bowers, and T.A. Baudino, *Cardiac fibroblast: the renaissance cell.* Circ Res, 2009. **105**(12): p. 1164-76.

189. Pedrotty, D.M., et al., *Cardiac fibroblast paracrine factors alter impulse conduction and ion channel expression of neonatal rat cardiomyocytes.* Cardiovasc Res, 2009. **83**(4): p. 688-97.

190. Lee, P., et al., *Simultaneous voltage and calcium mapping of genetically purified human induced pluripotent stem cell-derived cardiac myocyte monolayers.* Circ Res, 2012. **110**(12): p. 1556-63.

191. Moretti, A., et al., *Patient-specific induced pluripotent stem-cell models for long-QT syndrome.* N Engl J Med, 2010. **363**(15): p. 1397-409.

192. Itzhaki, I., et al., *Modelling the long QT syndrome with induced pluripotent stem cells.* Nature, 2011. **471**(7337): p. 225-9.

193. Arbab, A.S., et al., *In vivo trafficking and targeted delivery of magnetically labeled stem cells.* Hum Gene Ther, 2004. **15**(4): p. 351-60.

194. Assis, A.C., et al., *Time-dependent migration of systemically delivered bone marrow mesenchymal stem cells to the infarcted heart.* Cell Transplant, 2010. **19**(2): p. 219-30.

195. Grunnet, M., et al., *Biophysical characterization of the short QT mutation hERG-N588K reveals a mixed gain-and loss-of-function.* Cell Physiol Biochem, 2008. **22**(5-6): p. 611-24.